# Optical diagnostics of laser plasmas

Alice Pedregosa Delserieys

# Optical diagnostics of laser plasmas

A thesis presented on application for the degree of Doctor of Philosophy in the Faculty of Science by

**Alice Delserieys**

**BSc 2001**


School of Mathematics and Physics

The Queen's University of Belfast

Northern Ireland

February 18, 2008

*“ ‘I can’t believe that!’ said Alice.*
*‘Can’t you?’ the Queen said in a pitying tone. ‘Try again: draw a long breath, and shut your eyes.’*
*Alice laughed. ‘There’s no use trying,’ she said; ‘one cannot believe impossible things.’*
*‘I daresay you haven’t had much practice,’ said the Queen. ‘When I was your age, I always did it for half-an-hour a day. Why, sometimes I’ve believed as many as six impossible things before breakfast.’* [1] ”

**Pour mon mari en souvenir de notre aventure irlandaise.**

[1] *Alice’s Adventures in Wonderland*, Lewis Carroll

# Acknowledgements

I would like to use this opportunity to thank everybody who has helped me to carry on this research work.

I would like to thank first my supervisors Dave Riley and Ciaran Lewis for sharing with me their experience when needed while giving me the opportunity to gain my own experience. We had valuable exchanges about science, often prolongated in the friendly atmosphere of a Northern Irish pub. The scattering group, Fida Khattak, Elena Garcia, Shabbir Naz, Julio Angulo, Sahoo were of great support in our weekly Monday meetings and beyond. Colm McKenna, my first lab partner, showed me there was no need for stress in a lab.

This work would not have been possible without the help of the technical support staff. I am thinking in particular in Sidney and Kieran from the electronic workshop who rescued me in many laser's breakdowns. Philip Orr in the mechanical workshop managed after all to get all the parts of my experiments in place despite the delays I was leaving, always too short for the workshop schedules.

The strength of the physics department at Queen's certainly lies in the availability everyone is showing when it comes to getting something sorted. Dan Marlow showed great patience and care to support me with the laser maintenance, Victor Lindsay allowed me to borrow Level 3 lab equipment so I could progress faster. Mat Zepf, Tom Field, Bill Graham, Bob Mc Cullough, Marco Borghesi, Martin Lamb, Gleb Gribakin, Brendon Dromey, Satya Kar,

Adam Hunniford, Gagik Nersisyan, Chriss Calvert, Carlo Cecchetti were great costumers of the coffee club, it was nice and useful to work with them.

I was lucky as well to be given the opportunity to explore labs beyond Queen's walls and enjoy passionate and intensive times in large facilities. I would like to mention first John Costello for the many long and enthusiastic conversations we had in Dublin and in the FEL in Hamburg. The Luli team was my first contact in a French lab, which allowed me to enrich my French vocabulary (a flange is "UN flasque" in French). Frank Rosmej, in Prague, taught me rigorous analyses of atomic spectra that proved useful in my own research work.

Finally, I would like to thank all my friends who made this Belfast experience even more enjoyable, Fatima, Debbie, Heather, Jarlath, Fernando, Elena, Karola, Michaela, Charlie, Elm, Doro and others. My thoughts go to my family as well, Emma, Simon and my parents who had to eat British Christmas cakes and toffees for three years. I am not forgetting my adopted family Pedregosa Gutierrez for whom I went to Spanish classes.

Of course, my last thanks goes to my husband Jofre who taught me to count in 8 bits when it comes to salsa and 32 bits to use Matlab. Although I mastered better in 8 bits, with Jofre at my side, I still managed to change title twice in two years, from miss to misses and from misses to doctor.

**Abstract**

An optical Thomson scattering diagnostic has been implemented on low temperature laser-produced plasmas. This is a novel diagnostic for these types of plasmas which provides a reliable non-intrusive means of determining absolute values for electron number density and temperature, with a minimal number of assumptions required compared to most diagnostics used so far. A frequency doubled Nd:YAG laser was used as a source of scattered light, then detected with a gated ICCD detector after being spectrally resolved by a 1 meter grating spectrometer. The density and temperature of an expanding KrF laser-ablated magnesium plume have been obtained. The electron temperature was found to decay with the expected $T_e \propto t^{-1}$ dependence. However, it was found that the electron density has a time dependence $n_e \propto t^{-4.95}$ which can be explained by strong recombination processes. Atomic Raman satellites were also observed; they were identified as originating from transitions between the different angular momentum levels of the metastable $^3P^0$ term in $MgI$. Comparison with preliminary calculations of Rayleigh and Raman cross-sections of $MgI$ ground state and first excited state showed variations in the population of metastables relative to atoms and ions. The study was then extended further by adapting the system to an optical emission spectroscopy diagnostic. Up to $\sim$ 40% discrepancy in temperature was found between the results given by each diagnostics, questioning the assumption of local thermodynamic equilibrium in the plasma, assumed to analyse the emission spectra.

# Contents

# Chapter 1

# Introduction

About the electron:

*Could anything at first sight seem more impractical than a body which is so small that its mass is an insignificant fraction of the mass of an atom of hydrogen.*

*J. J. Thomson*

This thesis describes how a new technique was applied to investigate low temperature laser produced plasmas formed by the ablation of metallic targets in vacuum. The diagnostic developed to study these plumes, Thomson scattering, involved the interaction of plasma with well chosen laser beams, so as not to perturb the plasma. The purpose of this introductory chapter is to explain the context and the goal of this research work. Some basic concepts of plasma physics, necessary for the understanding of the rest of the work, are reviewed. The technique of laser ablation and the uses of the plasmas resulting from it are reviewed to underline the interest of the research carried out in this thesis.

## 1.1 Plasmas

### 1.1.1 What is a plasma?

Plasma is matter in a state of partial or complete ionisation. Ionisation occurs when electrons are removed from neutral atoms during the absorption of energy from an external source. The term plasma was first used by Langmuir in 1928 to describe the inner region of a glowing ionised gas found in an arc discharge. However for an ionised gas to be called a plasma, it has to meet three basic criteria:

1. quasineutrality
2. collective behavior
3. low collision frequency

Essentially, a plasma is an assembly of free electrons and positive ions. While locally, there may be a charge imbalance, in the assembly as a whole, there are, to a good approximation, equal numbers of positive and negative charges (quasineutrality). Charge separation between ions and electrons gives rise to electric fields, and charged particle flows give rise to currents and magnetic fields. These fields affect the motion of other charged particles far away (collective behavior) and result in a range of phenomena of great complexity.

Plasmas are not often observed naturally on earth with the exception of lightning or the aurora borealis, but are said to represent 99% of the matter in the universe [1]. It occurs naturally in stellar interiors and atmospheres, solar winds, gaseous nebulae and much of the interstellar hydrogen. In the laboratory, a plasma can be produced by raising the temperature of a substance until a reasonably high fractional ionisation is obtained. There are many different methods of creating a plasma and depending on the method, the plasma may have a high or low density, a high or low temperature,

it may be steady or transient, stable or unstable, and so on. The plasmas most commonly encountered in nature or in the laboratories are presented in figure 1.1 with a wide variety of applications given to them. The plasma regime of interest in the present work is situated in a region of temperatures around $1eV$ and densities from $10^{13}$ to $10^{17}cm^{-3}$. We called this region low temperature laser plasma on figure 1.1 adapted from Sheffield [2].

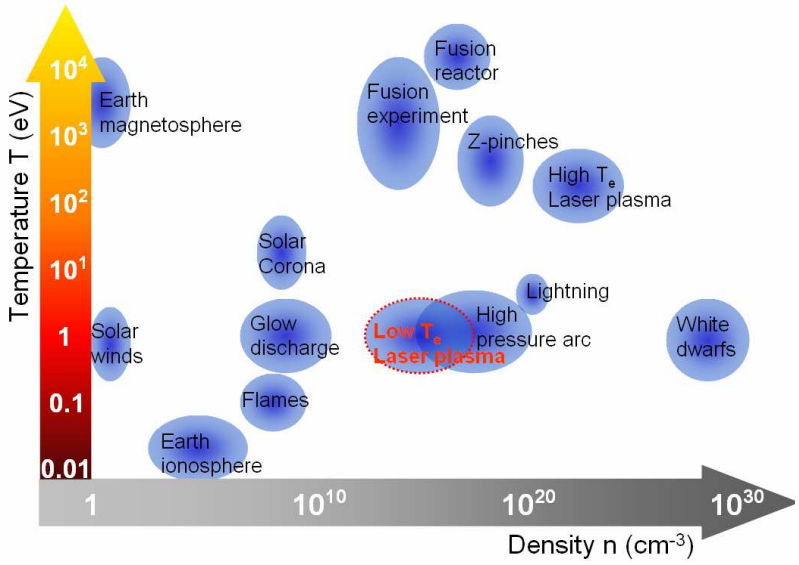


Figure 1.1: Density and temperature range of low temperature laser plasma compare to typical plasmas in nature and in the laboratory.

### 1.1.2 Characteristic lengths and times in a plasma

The charged particles in a plasma, both electrons and ions adjust their positions so they are screened from the electric fields of other charges. This characteristic distance over which the potential distance of a charge is shielded by neighboring charges defines the Debye length.

$$\lambda_D = \left( \frac{k_B T_e \varepsilon_0}{n_e e^2} \right)^{\frac{1}{2}} \tag{1.1}$$

Where $k_B$ is the Boltzman's constant, $\varepsilon_0$ is the permittivity of free space, e is the charge of an electron, $n_e$ the number density and $T_e$ the electron temperature. The electrons have individual behavior only on a scale shorter than the Debye length, so it makes it an important parameter in characterizing plasma-laser interactions. The number of electrons in the Debye sphere, $N_D$, is then given by

$$N_D = \frac{4}{3}\pi\lambda_D^3 n_e \tag{1.2}$$

Another parameter to consider in plasma-laser interaction is the plasma frequency. It is the lowest frequency at which an electromagnetic wave can propagate through the plasma without disturbing the plasma. If the electrons in a plasma are displaced from a uniform background of ions, electric fields will build up in such a direction as to restore the neutrality of the plasma by pulling the electron back to their original position. The electrons will oscillate around their equilibrium positions and it is this characteristic frequency that defines the plasma frequency,$\omega_p$

$$\omega_p = \left(\frac{n_e e^2}{m_e \varepsilon_0}\right)^{\frac{1}{2}} \tag{1.3}$$

where $m_e$ is the mass of an electron.

### 1.1.3 Temperature in a plasma

Temperatures in plasma physics are usually expressed in units of energy, electron-volts (eV). Using a Maxwellian distribution as the most probable distribution of particle velocities in a plasma, the average kinetic energy $E_{av}$ is [1]

$$E_{av} = \frac{3}{2}k_B T \tag{1.4}$$

where $k_B = 1.38 \times 10^{-23} J/K$ is the Boltzmann's constant and T is the temperature in K. Thus it is the energy corresponding to $k_B T$ that

is usually used to denote the temperature in a plasma, and for $k_BT = 1eV = 1.6 \times 10^{-19}J$, we have $T = 11,600K$. Unless stated otherwise, the temperature will be expressed in eV throughout this work.

## 1.2 Review of laser ablation and main applications

This research work is concentrating on plasmas produced by focusing laser beams onto solid targets. Since lasers were first developed in 1962, it was recognised that high-powered pulsed lasers could be used as a flexible and powerful tool for studying the interaction of intense electromagnetic fields with materials [3]. Nowadays, lasers have a broad range of applications in material processing. Their use in industry is extensive: laser cutting, welding, surface treatment, cleaning [4]. Laser ablation to create a plasma is widely used, with its range of applications going from medicine [5] to technology. One of the most important applications, and the one originally driving this work, is pulsed laser deposition (PLD) of thin film materials [6].

Conceptually and experimentally, PLD is extremely simple, probably the simplest among all thin film growth techniques. It consists of a target holder and a subtract holder in a vacuum chamber. A laser is used to vaporise solid or liquid materials and to deposit thin films. A set of optical components is used to focus and raster the laser beam over the target surface. This technique is flexible and easily adaptable to different operational modes. It also has the ability to preserve the stoichiometry of compound materials under optimum conditions. Film growth can be carried out in a reactive environment containing any kind of gas, and a wide variety of ablating material can be used. The technique is so versatile that with the choice of an appropriate laser it can be used to grow films of any kind of material. However, such versatility might have slowed down the progress of PLD as research efforts were spread among many different materials. It presents as well the disadvantages

of presence of micro-sized particulates, and narrow forward angular distribution that makes large-area scale-up a very difficult task. PLD progress has been governed by laser progress. Mainly in the late 60s, the apparition of ns lasers with the development of the Q-switch, the high-efficiency 2nd harmonic generator to deliver shorter wavelength radiation, and better long term stability, increased the level of research. Interest rose again in the late 1980s with the success in the growth of commercial superconductors [7, 8].

The dominant mechanisms involved in such processes and in the resulting formation of a hot plasma from the irradiated surface will be described in a subsequent chapter as a better understanding is required for the interpretation of the data obtained in this work. To summarise, the mechanisms were found to depend sensitively on laser parameters such as the energy density (fluence), pulse duration, wavelength, polarisation, laser repetition rate, as well as the material being irradiated. In general, the useful range of laser wavelengths to ablate material for thin film growth lies between 200 and 400 nm, as most material used for deposition work exhibit strong absorption in this spectral region. Excimer lasers are usually the lasers of choice for PLD, as they emit directly in the ultraviolet range and can achieve pulse repetition rates up to several hundred hertz with energies near 500 mJ/pulse. In this present research project, a KrF excimer laser was used to ablate material (see chapter 4), situating the work in typical PLD conditions.

In contrast to the simplicity of the set up, the laser-target interaction and the plasma expansion are very complex physical phenomena. A number of mechanisms are involved: laser absorption, heating, melting, evaporation, expansion, ionisation, radiation, recombination and condensation. Theoretical descriptions are multidisciplinary and combine both equilibrium and non equilibrium processes. As a result, the fundamental processes occuring

within the plume during expansion away from the target are still not fully understood. They have been the subject of study at Queen's University for several years [9, 10, 11, 12, 13], and further development of novel diagnostics is essential to fully explore laser ablated plasma plumes.

## 1.3 Review of laser-plasmas diagnostics

As the number of applications for laser-produced plasma grew, so did the battery of diagnostic techniques to characterise them [14]. However, complete characterisation is extremely difficult due to the number of processes involved and by the numbers of parameters that can alter the plume properties, especially in the initiating laser pulse. Laser wavelength, intensity, pulse duration, spot size or beam profile can have dramatic effects [15]. The key parameters to measure in laser produced plasmas are the density and temperature.

The discussion in the present work will be limited to the case of low temperature plasmas, as most diagnostic techniques are only applicable over a specific range of values, where theoretical assumptions are valid, and can be applied to the experimentally recorded data, thereby allowing the inference of the desired parameter. Complete characterisation of the plasma plume requires an understanding of the advantages and limitations of several diagnostic techniques as well as their results.

**Electrostatic ion probes** (or Langmuir probes) are among the oldest and most basic diagnostics. They were primarily developed to measure the electron density and temperature in non flowing plasmas [16]. They are now applied as well to laser produced plasmas [17, 18]. They consist of a wire tip or small electrode immersed directly into the plasma to provide

local information on plasma conditions by examining the current collected by the probe. They have the advantage of being cheap and relatively easy to implement, but are restricted to investigate regions where the plasma has expanded enough to introduce a probe (far away from the target, $> 1cm$ and late in time, $> 1\mu s$). Moreover, it is an intrusive technique; the introduction of the probe might perturb the plasma initial conditions.

**Optical emission spectroscopy** (OES) is another broadly used technique, mainly because it is easy to implement and non intrusive. It is a less accurate method, as it relies on the validity of a few assumptions to obtain useful information. It also relies on the study of the shape and width of spectral lines that can be altered by numerous mechanisms. Details of the quantum mechanical theories to extract information from optical emission line profiles can be found in Griem's textbook [19]. Assuming Local Thermodynamic Equilibrium (LTE) of the plasma, the temperature can be estimated if relative intensities are measured for different transition frequency in the same atom or ion. The electron density can be deduced from measured Stark profiles if the plasma is dense enough ($N_e \geq 10^{15} cm^{-3}$) and emitting neutral or singly ionised lines. However Doppler broadening usually tends to override the Stark broadening of lines emitted by multiply ionised atoms.

**Laser Induced Fluorescence** (LIF) and **Optical Absorption Spectroscopy** (OAS) benefit advantages over OES such as the ability to probe non-emitting levels of energy and as a result to infer the density of selected species. LIF and OAS are usually measured simultaneously due to their coexistent nature. The technique is based on passing light of known wavelength through the plasma. If the laser is tuned to an appropriate transition, atoms are excited from the ground state to excited electronic levels by absorption of energy from the incident laser. Once excited, they can decay back to a

lower level of energy by spontaneous emission of a photon. This last process is referred to as fluorescence. In principle, the intensity of fluorescence is proportional to the density of the excited state species. Such measurements were performed at Queen's University on magnesium plasma plumes by Doyle and Martin [9, 10]. However, their measurements were compromised by strong reabsorption in the denser part of the plasma, which was optically thick.

A reliable and absolute diagnostic to measure electron densities and temperature in denser part of the plasma is **interferometry** [20]. Among the various possibilities, the Mach Zehnder Interferometer [21, 22] is advantageous as it is a single pass system, as opposed to the Michelson Interferometer. The technique uses the interferometer to measure the refractive index of the plume by measuring the change in the optical path difference that the plasma introduces. The phase of the traversing beam is altered by variation in refractive index which is caused by electron density gradient. The optical path is recorded as a fringe pattern and the electron density and temperature can be determined from this interference pattern. Using an ICCD detector (Intensified Charge Coupled Device), Doyle et al [22] measured electron densities of the order of $10^{18} cm^{-3}$ for a magnesium plume ablated by a KrF excimer laser close to the target and early in time with temporal and spatial resolution. However, a minimum measurable fringe shift limited experimental measurements to $< 100ns$ times and $< 700\mu m$ from the target surface.

The main diagnostic developed in the present research work is **Thomson Scattering**. It is a well established diagnostic for other types of plasmas, and presents many advantages detailed in chapter 3. However, The main area of application for Thomson scattering so far has been to high-temperature and

high-density plasmas (above $10^{18}cm^{-3}$). In recent years, efforts have been made to reduce the detection limit to below $10^{17}cm^{-3}$, which is the regime common for plasmas used in industrial applications. Thomson scattering diagnostics have been applied to RF discharges [23], and in particular at Queen's University [24, 25, 26], where electron densities down to $10^{11} - 10^{12}cm^{-3}$ were measured, opening the road to applying the diagnostic to low temperature laser-plasmas.

## 1.4 Aims and objectives

The work presented in this study is part of a broader research project to investigate laser ablated plumes of interest for PLD work. This research is first driven by applied requirement of materials processing technology mentioned in section 1.2. Single expanding plasmas of mainly Mg and Ti [9, 10], as well as modified plasmas [12, 13] have been studied so far at Queen's University. These include plasmas going through a charged mesh, or pinholes to make plasma jets, or two colliding plumes. The diagnostics used to investigate these plasmas have been reviewed in the previous section 1.3 and include Langmuire Probe, OAS, LIF and interferometry. All diagnostics have their limitations, and are applicable in a range of plasma conditions, illustrated in figure 1.2.

To extend the spatial and temporal mapping of the laser produced plasmas at Queen's University, a Thomson scattering diagnostic was implemented. This is a new type of diagnostic for these types of plasmas and presents the advantage of being relatively simple to interpret. The objective is then to be able to use it as a benchmark for other diagnostics, easier to implement.

It should not be forgotten that the aim of this project is also to extend

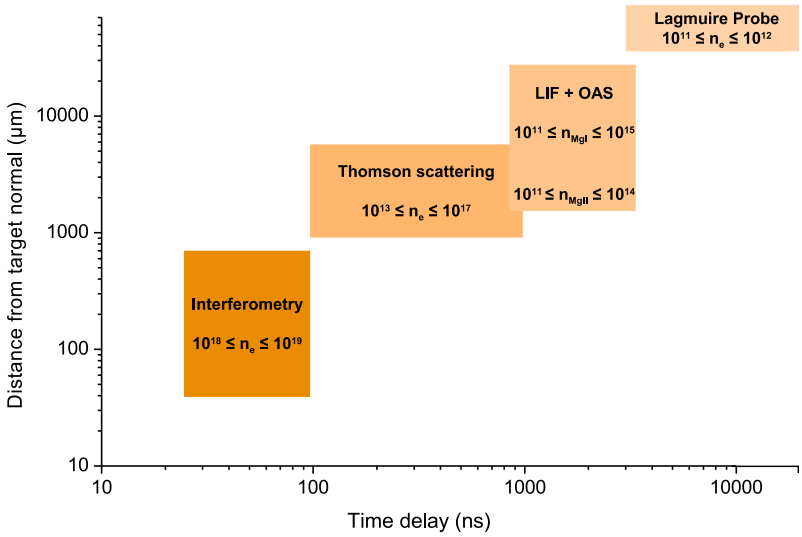


Figure 1.2: Range of diagnostics used in the laboratory of QUB on Mg laser produced plasmas. Details of each plasma study can be found in [18, 22, 27, 28]. The densities are in units of $cm^{-3}$

the fundamental knowledge about laser ablated plume dynamics. This thesis will then guide the reader from the development of a new diagnostic for low temperature laser plasmas to a discussion on the plasma dynamics arising from the measurements made.

## 1.5 Overview of the thesis

This thesis has been divided into 7 chapters. A short description of the content of each chapter is presented below.

**Chapter One:** gives a brief overview of the motivations for implementing a Thomson scattering diagnostic on low temperature laser-produced plasmas, with a brief description of other diagnostics available.

**Chapter Two:** discusses the relevant theoretical background to understand the plasma plume dynamics. Basic atomic processes in plasmas and

thermodynamic equilibrium models are outlined.

**Chapter Three:** outlines the specific theory relating to light scattering observed in this work. Methods for extracting plasma parameters from the scattered spectra have been presented.

**Chapter Four:** provides a detailed description of the experimental system used during the work. The experimental issues in setting up a Thomson scattering experiment are discussed.

**Chapter Five:** presents result and analyses of the plasma scattering spectra and emission spectra. This is followed by a discussion on the time and space evolution of the laser-produced Mg plumes.

**Chapter Six:** presents time resolved emission spectroscopy results of the expanding Mg plasma plume. This results can then be compared to the ones obtained by Thomson scattering.

**Chapter Seven:** concludes this thesis by providing a summary of the results presented in this research work. Suggestions for possible further work are discussed.

# Chapter 2

# Laser plasmas

*"In science one tries to tell people, in such a way as to be understood by everyone, something that no one ever knew before. But in poetry, it's the exact opposite. "*

Paul Dirac

When high intensity laser light interacts with a target, it produces a plume, expanding rapidly away from the target surface, of material containing neutrals and ions in both ground and excited states, electrons, photons, clusters and particulates. In this study, we concentrate on the irradiation of metallic surfaces in vacuum with ultraviolet (UV) nanosecond laser pulses at moderate fluence ($5 - 10 Jcm^{-2}$), that are widely used for the deposition of thin solid films. The luminous plumes produced have typically temperatures of the order of a few eV.

The different stages for the generation of laser produced plasmas with high irradiance pulses are illustrated by figure 2.1. This chapter outlines some of the basic mechanisms involved in the three overlapping regimes

that can be identified:

1. Figure 2.1 (a)-(b)-(c): The interaction of laser light with the target material, causing heating, melting and evaporation will be described in section 2.1.1.

2. Figure 2.1 (c)-(d): The interaction of laser light with the evaporated material (section 2.1.2) as well as an isothermal expansion perpendicular to the target surface will be discussed in section 2.2.

3. Figure 2.1(e): An adiabatic three-dimensional expansion of the plume in vacuum after the ablation pulse has terminated (section 2.2) accompanying numerous atomic processes reviewed in section 2.3.

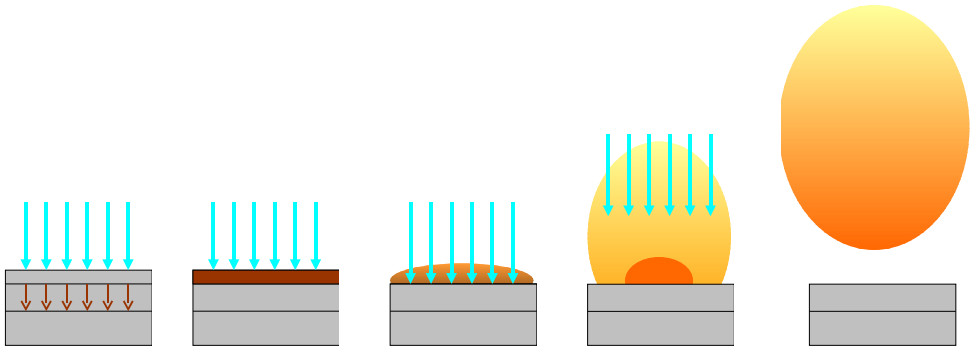

(a) Absorption and thermal diffusion

(b) Melting of target material

(c) Vaporisation of target material, thermally ionised material

(d) Absorption of laser radiation, plasma formation

(e) Adiabatic 3-D plasma expansion

Figure 2.1: Schematic illustration of successive stages of ablation mechanisms and plasma expansion: laser - target interaction (a) - (b) - (c), laser - plasma interaction and isothermal expansion (c) - (d), adiabatic expansion (d) - (e).

This chapter outlines some of the basic mechanisms within each stage of the plasma formation. The plasma expansion dynamics during and after the

laser pulse will then be discussed, as well as some atomic processes occurring during the expansion, and equilibrium conditions often considered in the study of plasmas.

## 2.1 Plasma formation

The properties of the plasmas produced and expansion dynamics are very sensitive to the conditions used to create them. Laser pulse, wavelength, spot size, fluence, even pulse shape are all important factors. The properties of the target material, such as atomic weight, density, surface reflectivity, conductivity, melting and boiling points have to be considered as well.

### 2.1.1 Laser - Solid Interaction

When laser light is incident on a metallic target, some of it is reflected at the surface while some of the radiation penetrates and undergoes an exponential decay in intensity as a function of time t and distance x into the solid [29].

$$I(x,t) = I_0(t)exp(-ax)[1-\Re] \tag{2.1}$$

In this relationship $I_0(t)$ is the laser irradiance at the surface, $\Re$ is the surface reflectivity, and $a$ is the absorption coefficient. The reciprocal of $a$ gives the optical absorption length, penetration distance of the radiation, with

$$a = \sqrt{\frac{2w\sigma_0}{\varepsilon_0 c^2}} \tag{2.2}$$

where $w$ is the angular frequency of the incident radiation, $\sigma_0$ is the target electrical conductivity, $\varepsilon_0$ is the permittivity of free space and c is the speed of light in vacuum [30].

Radiation is absorbed by electrons, raising them to higher energy states in the conduction band defined roughly by the laser spot size on the surface times the optical absorption length. Energy is then transferred to the lattice by collisions of the electrons both among themselves and with lattice phonons. The surface is quickly heated and melted, changing the optical characteristics of the surface [31]. The result is a decrease in reflectivity, thereby increasing the proportion of the laser-light that is absorbed by the target. For a nanosecond pulse, a significant amount of heat is conducted into the bulk of the material, to a depth below the surface determined by the thermal diffusion length, $L_{th}$ [14]

$$Ł_{th} \approx \sqrt{2D\tau_p} \tag{2.3}$$

where $\tau_p$ is the laser pulse duration, and D is the heat diffusion coefficient ($D = \frac{k}{\rho C_T}$, k, $\rho$ and $C_T$ are thermal conductivity, mass density, and specific heat capacity respectively). For nanosecond laser pulses interaction with metallic target materials, the thermal diffusion length is much larger than the optical absorption depth

$$Ł_{th} \gg a^{-1} \tag{2.4}$$

In such a case, the absorbed energy is stored in a layer of thickness of the order of $L_{th}$, and the evaporation of the molten metal layer can occur when the energy absorbed by the skin depth $a^{-1}$ becomes larger than the latent heat of evaporation. The ablation depth can then be evaluated as

$$\Delta Z_\nu \approx \frac{(1-\Re)(F_L - F_{th})}{\rho L_\nu} \tag{2.5}$$

where $F_L$ is the laser fluence, $F_{th}$ represents the minimum energy above which evaporation occurs, and $\rho L_\nu$ is the latent heat evaporation per unit volume [14].

The thermal and optical properties of the sample influence the amount of material removed during the laser pulse, as well as properties of the laser pulse itself. The process is complex to model, especially since optical and thermal properties of the material vary during the laser pulse, which makes it difficult to accurately predict the amount of energy coupled to the target and the quantity of mass removed.

Table 2.1: Physical properties of pure magnesium (99.9%). All values are taken from reference [32] but the reflectivity (see text).

| Parameter | Unit | Magnesium |
|---|---|---|
| Melting point, $T_m$ | K | 923 |
| Boiling point | K | 1380 |
| Reflectivity, $\Re$ | | 0.84 |
| Latent heat of evaporation, $L_\nu$ | $J.kg^{-1}$ | $5.25 \times 10^6$ |
| Specific heat capacity, $C_T$ | $J.K^{-1}.kg^{-1}$ | 1025 |
| Thermal conductivity, $k$ | $W.m^{-1}.K^{-1}$ | 156 |
| Electrical conductivity | $\Omega^{-1}.m^{-1}$ | $22.6 \times 10^6$ |
| Density, $\rho$ | $kg.m^{-3}$ | 1740 |

Using the above formulas, and the thermo-physical properties for magnesium shown in table 2.1, we can evaluate the total mass of Mg ablated by a $248nm$ KrF laser with fluence of $10J.cm^{-2}$ and a pulse duration of $20ns$, corresponding to the ablation condition under study in this work. In the case of nanoseconds laser pulses irradiation, the evaporation takes place from liquid metals, so the laser fluence threshold $F_{th}$ is given approximately by the energy needed to melt a surface layer of the order of $L_{th}$ [14]:

$$F_{th} \approx \frac{\rho C_T \Delta T_m L_{th}}{1 - \Re} \tag{2.6}$$

with $\Delta T_m = T_m - T_0$, difference between the melting and initial target temperature. The calculated fluence threshold for magnesium ablation by the KrF laser is of the order of $\sim 1.4 J.cm^{-2}$, the calculated ablation depth $\sim 1.4 \mu m$ giving an estimation for total mass ablated of $M_{T1} \approx 7.4 \times 10^{-7} g$.

The value of the reflectivity $\Re$ in table 2.1 was calculated for a $248nm$ laser radiation from the following equation [30]

$$1 - \Re = \sqrt{\frac{8w\varepsilon_0}{\sigma_0}} \tag{2.7}$$

However, as mentioned before, the material parameters are expected to change with target temperature and the vapor cloud formed above the target surface is expected to act as a shield absorbing the laser beam. That would lower considerably the target surface absorbance $(1 - \Re)$ and evidently the ablation depth. Amoruso *et.al.* [14], suggest an absorbance of 0.03 for copper laser ablation at $248nm$ instead of the value of 0.1 that can be calculated with equation 2.7. Assuming a similar decrease in the case of Mg ablation, an absorbance of 0.04 can be considered. This value would give an ablation depth of $\sim 200nm$, and a total mass ablated $M_{T2} \approx 1 \times 10^{-7} g$. Furthermore, Lunney *et.al.* [33] developped a model to describe the main physical processes involved in the laser heating and vaporisation of metal targets. The model includes laser absorption and heating of the vaporised material, ionisation dynamics and re-radiation to the target surface. Their model predicts an ablation depth about 6 times smaller than a model not taking into accound absorption mechanisms, which is close to the estimation made above. The amount of material ablated is an important initial parameter when modeling the plume expansion as shown in section 2.2.

The study of the ablation process involving modelling of real systems is further complicated in practice by the modification of the topography of the

target surface exposed to repeated irradiation. Laser ablation-induced cones have been observed producing micron-size particulates in the plume [34]. These particulates are a major issue in the growth of thin films [6], and could compromise as well the use of radiation scattering, which is the plasma diagnostic used in the present study. Rotating the target, as described in section 4.1.1, is a way to avoid repeated irradiation on the same target surface.

Once the surface of the metal rises to the vaporisation temperature and begins to vaporise, the material recoiling against the surface produces a high pressure. This pressure pulse raises the boiling point of the underlying material which becomes superheated as more heat is conducted into the interior. Eventually, as the temperature rises high enough, the emission of this high pressure material can proceed [35]. During this process, electrons are stripped from the atoms by direct and multi-photon ionisation. The free electrons so produced further absorb laser radiation by the process of inverse bremsstrahlung (IB) (see section 2.3.1). This dramatically improves the absorption rate of incident photons. The electrons subsequently transfer their increased kinetic energy to the atoms and ions through collisional ionisation and excitation processes. These ionisation processes increase the electron density thereby further enhancing the absorption of incident radiation. The increased ion density allows us to now refer to the vaporised material as plasma [36].

### 2.1.2 Laser - Plasma Interaction

Once plasma expansion has started, two regions of plasma interacting with the laser radiation can be distinguish (figure 2.2) [36]:

- Region C: close to the target surface, where dense plasma is absorbing laser radiation,

- Region D: plasma is expanding isothermally, transparent to the laser beam due to its lower electron density.

The expansion of the plasma at this stage can be considered isothermal because the plasma still has a small velocity and volume (figure 2.1(c)). Therefore it can thermalise faster than the characteristic plasma expansion time [36]. The other regions represented on figure 2.2 correspond to the volume of the target:

- Region A: Unaffected target,
- Region B: Evaporated target material, of thickness $\Delta Z_\nu$ (equ. 2.2)

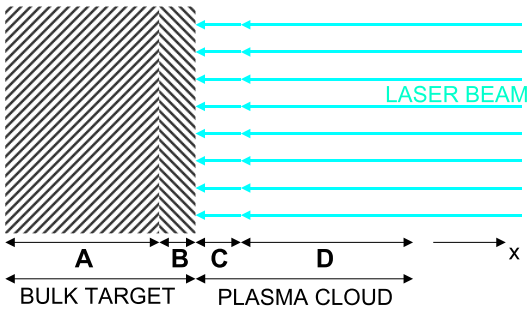


Figure 2.2: Schematic diagram showing the different phases present during laser irradiation of target material.

The presence of the strongly absorbing plasma, region C, results in partial (if not complete) screening of the surface from the incident laser radiation. The type of mechanisms which can be responsible for the absorption of the laser energy within the plasma depend on the ablation laser parameters and the local conditions within the plasma. The two dominant photon absorption processes in laser ablation of metals under typical PLD conditions are inverse bremsstrahlung (IB) and photoionisation (PI) [14]. PI is likely to produce an effective enhancement of the excited and ionised species which in turns enhance the probabilities of photon absorption by IB due to

electron-ion collisions [37]. These two atomic processes will be described in a later section (see section 2.3).

Another form of plasma shielding of the target arises from the plasma frequency $\omega_p$ (equation 1.3). An electromagnetic wave of frequency $\omega$ can only propagate in a plasma provided $\omega_p < \omega$ [31]. As a result, an electromagnetic wave travelling in a plasma will propagate until it reaches an electron density sufficiently large that $\omega_p$ becomes greater than $\omega$. From equation 1.3, this means that the electron density must be less than the critical density given by

$$n_c = \frac{m_e \varepsilon_0 \omega^2}{e^2} \tag{2.8}$$

This gives us a value of $\approx 1.8 \times 10^{22} cm^{-3}$ for the UV excimer laser radiation at 248 nm used in this work. The high value of the critical electron density means that the reflection losses by the plasma are reduced for excimer laser generated plasmas.

The density in region C increases as the target is beeing ablated until shielding of the target surface occurs. In the mean time as the plasma expands, the electron density decreases rapidly allowing once again radiation to reach and ablate the target, and rising the density until shielding of the surface is significant. The absorbtion and shielding of the laser radiation in the plasma produced follows this dynamic "self-regulating" regime [38] until the termination of the laser pulse.

## 2.2 Plasma expansion

After the termination of the laser pulse, the plasma expands rapidly in vacuum due to the large density gradients. The largest acceleration is in

the direction of smallest dimension, due to the larger pressure gradients, so the expansion velocity along the target normal will be significantly larger than its perpendicular component. Therefore, the plume shape will evolve and change from the initial rounded cap to an oblong ellipsoidal plume (figure 2.1(d)). This expansion process can be treated as a self similar expansion, meaning that the velocity is proportional to the distance from the target. Singh and Narayan [36] represent this relationship by the following expression,

$$v(i) = \frac{i}{I(t)} \frac{di}{dt} \tag{2.9}$$

where i represents the distance in any direction (x, y or z), v(i) is the velocity as a function of distance, $di/dt$ is the expansion velocity at the plume edge, and $I(t)$ the dimension of the plume in the respective direction. This expression shows that the direction of smallest initial dimension exhibits the highest velocity, and the velocity will be maximum at the plume edge.

At this stage, the plasma can be considered to expand adiabatically [36] and so described by the adiabatic thermodynamic equation,

$$T\left[X(t)Y(t)Z(t)\right]^{\gamma-1} = constant \tag{2.10}$$

where T is the temperature of the plume, X(t), Y(t) and Z(t) are the dimension of the plume at a time t and $\gamma$ is the ratio of specific heat capacity at constant pressure and volume. Due to this expansion, the plasma density $N$ is decreasing, as well as its temperature $T$, linked by

$$T \propto N^{\gamma-1} \tag{2.11}$$

At late time (typically 100 times the laser pulse length), most of the thermal energy is converted into kinetic energy. The ion acceleration is then

negligible and at even later times, the plume will undergo free expansion into three dimensions. In this situation, conservation of mass requires the position r of a plasma element to be proportional to time t. As a result, the volume of this element V is proportional to $r^3 \propto t^3$, and the density of particles can be expressed as

$$N \propto r^{-3} \propto t^{-3} \tag{2.12}$$

For a monoatomic gas with three degrees of freedom, $\gamma$ is equal to 5/3. It can then be deduced that [39]

$$T \propto r^{-2} \propto t^{-2} \tag{2.13}$$

However, Zel'dovich and Raizer [40] point out that the value of $\gamma$ decreases to 9/7 in the case where excited states and ionised species are taken into account.

Due to the large densities present, the plume can be treated as a fluid and equations of gas dynamics can be applied in order to simulate its expansion [41]. This section does not have the pretention to present a complete simulation of the plume expansion dynamic, which is the subject of study of many groups, who developed complex codes ( [29, 36, 41, 42, 43, 44] and many others). The aim is to get a rough estimation of how the plume can be expected to behave. In this section, the x-axis designates the normal to the target surface (axis of expansion) and the origin of coordinates are at the target surface.

Two approaches have been made to model the gas dynamic analytically. In an isothermal view-point, Singh *et.al.* [36] considers a spatially constant temperature with a Gaussian density profile N at any point (x,y,z) and time t after the end of the laser pulse given by

$$N(x,y,z,t) = \frac{N_T}{\sqrt{2}\pi^{1.5}X(t)Y(t)Z(t)} exp\left[-\frac{x^2}{2X(t)^2} - \frac{y^2}{2Y(t)^2} - \frac{z^2}{2Z(t)^2}\right] \tag{2.14}$$

where $N_T$ is the total number of evaporated particles at the end of the laser pulse, X(t), Y(t) and Z(t) are the dimensions of the expanding plasma in the three orthogonal directions, and $X_0$, $Y_0$ and $Z_0$ their respective values at the termination of the laser pulse.

Similarly, assuming a spatially variable temperature with an ellipsoidal density profile, Anisimov *et.al.* [42] propose an isentropic solution given by

$$N(x,y,z,t) = \frac{N_T}{I_1(\gamma)X(t)Y(t)Z(t)} exp\left[-\frac{x^2}{X(t)^2} - \frac{y^2}{Y(t)^2} - \frac{z^2}{Z(t)^2}\right]^{1/\gamma-1} \tag{2.15}$$

where $I_1(\gamma)$ is an integral expressed in terms of the $\Gamma$ function.[1]

It should be noted here that $N$ refers to the density of all species in the plasma, including atoms, ions, neutrals, small clusters, etc. However, based on the difference in their masses, the expansion velocities may be different for different species [36].

The experimental study, detailed in the following chapters, treats of the $248nm$ excimer laser ablation of Mg targets. The total mass ablated has been estimated in section 2.1.1 giving an estimation of $N_T$, the total number of evaporated particles at the end of the laser pulse. The expansion velocity of the Mg plume material is estimated to be $\sim 1.7 \times 10^6 cm.s^{-1}$ from Doyle's interferometry work [22] under similar ablating conditions. In this case, the density profiles N(0.2,0,0,t) given by equation 2.14 for the isothermal case,

[1] To calculate $I_1(\gamma)$, the Stirling's asymptotic formula was used for the $\Gamma$ function: $\Gamma(x+1) = \sqrt{2\pi x}\ x^x exp(-x)\left[1 + \frac{1}{12x} + \frac{1}{288x^2} - \frac{139}{51840x^3}\right]$

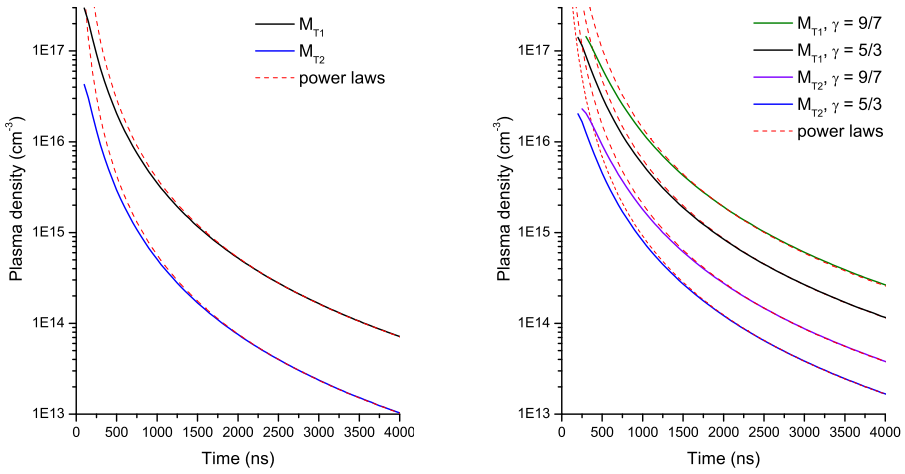


(a) Isothermal (b) Isentropic

Figure 2.3: Plasma density profile $2mm$ from the target surface from the self-similar gas dynamics model from isothermal (a) and isotropic (b) view-points. $M_{T1}$ and $M_{T2}$ refer to the total ablated mass calculated in section 2.1.1. All curves are best fitted with power laws $\propto t^{-2.9}$ at late times.

and by equation 2.15 for the isentropic case were plotted in figure 2.3. The graph gives the evolution with time of the total density of a plasma volume $2mm$ from the target surface. It appears clearly that an accurate estimation of the total ablated mass is needed in the initial conditions of a model for plasma expansion. In figure 2.3 both values, $M_{T1}$ and $M_{T2}$, estimated in section 2.1.1 were used. The density profiles show a good fit to power laws $\propto t^{-3}$ at late time.

This adiabatic expansion region typically extends between $1 - 10mm$ from the surface. As the plume keeps expanding, and the density falling, the system passes into a collisionless free expansion. This can result in the freezing of ionised species [39, 45] and enables the detection of ions several centimeters from the target, making electrostatic ion probe a useful and wide spread diagnostic for this type of plasmas (see section 1.3). In this study, we

will concentrate in the plasma region expanding over a few millimeters (up to 5 mm) and up to a microsecond.

## 2.3 Atomic processes in plasmas

The manner in which radiation is absorbed, transported or emitted from plasmas is governed by atomic processes within the plasma. The relative importance of each of these processes at any given time depends on local plasma conditions such as temperature, ionisation stage, electron / ion / photon densities.

This section will present a short review and classification of the twelve most important mechanisms of absorption and emission, relating to laser-produced plasmas.[2] Working formulas to calculate their rates, will be discussed when directly needed to the interpretation of the data presented in chapter 5. All allowed electronic transitions accompanying the absorption and emission of light are subdivided into three types, free-free, bound-free and bound-bound processes. Table 2.2 shows all the processes considered in the following section, classified in their various sub-categories. Depending on the main method of energy transfer, each process can be further described to be either collisional or radiative.

### 2.3.1 Free-free processes

The two free-free processes significant in laser produced plasmas are bremsstrahlung and its inverse process. In particular, Inverse-Bremsstrahlung (IB) is the most important method of plasma heating by laser radiation in the energy regime of this work.

[2]Unless otherwise indicated, the information in this section is taken from reference [46].

Table 2.2: Main atomic processes in laser-produced plasmas, where $F \Leftrightarrow F$ designates free-free transitions, $B \Leftrightarrow F$ bound-free transitions and $B \Leftrightarrow B$ bound-bound transitions. $e^-$ stands for electron.

| **Process** | **Excitation** | **De-Excitation** | **Type** |
|---|---|---|---|
| $F \Leftrightarrow F$ | Bremsstrahlung | | Collisional |
| $F \Leftrightarrow F$ | | Inverse Bremsstrahlung | Radiative |
| $B \Leftrightarrow F$ | $e^-$ Impact Ionisation | 3-Body Recombination | Collisional |
| $B \Leftrightarrow F$ | Photoionisation | Radiative Recombination | Radiative |
| $B \Leftrightarrow F$ | Autoionisation | Dielectronic Recombination | Mixed |
| $B \Leftrightarrow B$ | $e^-$ Impact Excitation | $e^-$ Impact De-excitation | Collisional |
| $B \Leftrightarrow B$ | Photoabsorption | Spontaneous Decay | Radiative |

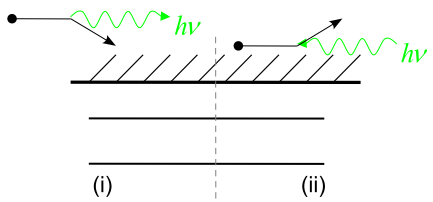


Figure 2.4: Schematic description of Bremsstrahlung and Inverse Bremsstrahlung processes.

**Bremsstrahlung** is the process where a free electron moving close to an ion is accelerated by the ion's Coulomb field, thereby producing radiation. The process is represented in figure 2.4(i), it is a collisional process. Bremsstrahlung is the main contributing factor to the continuum radiation observed in the spectra of hot plasmas.

**Inverse-Bremsstrahlung** is obviously the inverse of the above process. It occurs when a free electron that moves near an ion or a neutral absorbs a photon, thereby increasing its kinetic energy. In order that momentum

be conserved, the nearby ion or neutral carries away the extra momentum. These collisions either ionise or excite atoms or ions present in the plasma. The IB process is shown in figure 2.4(ii). The inverse-bremsstrahlung absorption coefficient $\alpha_{IB}(cm^{-1})$ due to electron-ion collision may be calculated using the following formula from Rybicki and Lightman [47],

$$\alpha_{IB} = 3.7 \times 10^8 \frac{Z^2 n_e n_i}{T^{1/2}\nu^3}\left(1 - e^{-h\nu/k_B T}\right)\bar{g}_{ff} \tag{2.16}$$

where T is the temperature in Kelvin, $n_e$ and $n_i$ the electron and ion densities in $cm^{-3}$, $h$ the Plank's constant in $J.s$, $k_B$ the Bolzmann's constant in $J.K^{-1}$, Z the average degree of ionisation, $\nu$ the frequency of the incoming photons in $s^{-1}$. The Gaunt factor $\bar{g}_{ff}$ will be assumed to be of the order of unity throughout this work.

IB due to electron-ion interactions is usually up to three orders of magnitude larger than that due to electron-neutral collisions when the ion density is high [48]. It can be seen from equation 2.16 that the IB process is less efficient in the ultra-violet than in the visible and infra-red part of the light spectrum. The efficiency depends as well upon the thermo-physical properties and the nature of the species interacting with the electron (ionisation potential and electronic structure of the evaporated atoms). IB is of particular interest in this work, not so much for its role in the plasma formation, but to evaluate the perturbation of the plasma by the probe laser in the scattering experiment described later in this thesis (see section 5.4.2).

### 2.3.2 Bound-free processes

Bound-free processes occur when an ion either receives enough energy to eject one of its bound electrons into the continuum, and increasing its ionisation state, or when an electron in the continuum loses energy and falls into a discrete energy level of an ion, reducing its ionisation state. The different

types of bound-free processes of interest are illustrated in figures 2.5 and 2.6.

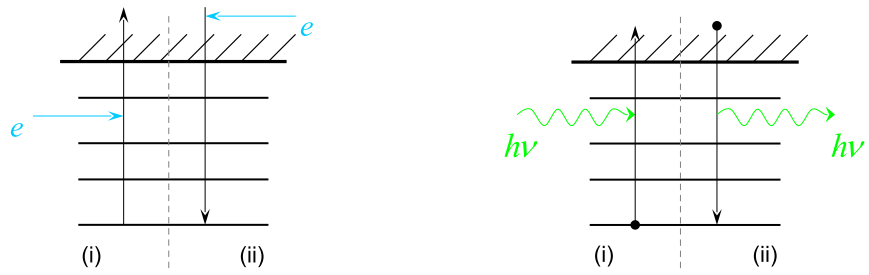


(a) Electron Impact Ionisation and 3-Body Recombination

(b) Photoionisation and Radiative Recombination

Figure 2.5: Schematic description of bound-free transitions frequent in laser-produced plasmas. (a) collisional processes and (b) radiative processes.

**Electron-impact ionisation and three-body recombination (3BR)**

Electron impact ionisation (fig. 2.5(a)(i)) occurs when a free electron $e$ collides with an atom or ion, giving enough energy to ionise it, releasing a bound electron from the atom or ion into the continuum. The collision increase the charge of the ion, as may be represented by

$$A_i^z + e \Longleftrightarrow A_j^{z+1} + e' + e'' \tag{2.17}$$

where A denotes an ion at energy level, $i$ or $j$ corresponding to the charge state $z$ or $z+1$, respectively. $e'$ and $e''$ denotes the energy of the electron after interaction ( $e' < e$) and of the new free electron.

The ionisation rate coefficient $S_z(T_e)$ can be expressed as [49]

$$S_z(T_e) = \frac{1.64 \times 10^{-6}}{\chi_z T_e^{1/2}} \times exp\left[\frac{-\chi_z}{T_e}\right] \qquad (cm^3 s^{-1}) \tag{2.18}$$

where $\chi_z$ is the ionisation potential of charge state $z$, $T_e$ the electron temperature, both expressed in electron volts.

In the 3BR process, shown on figure 2.5(a)(ii), two continuum electrons $e'$ and $e''$ enter the volume of an ion simultaneously. One of the electrons is reduced in energy and decays to a bound state of the ion, the other electron accepts the extra energy and remain in the continuum. One electron has recombined and the ion is reduced in charge represented by the right-to-left reaction in equation 2.17. The 3BR rate coefficient can be expressed as given by Thum-Jaeger *et.al.* [50]

$$\alpha_{3BR}(T_e) = \frac{2.97 \times 10^{-27} \xi_z}{T_e \chi_z^2 (4.88 + T_e/\chi_z)} \qquad (cm^6 s^{-1}) \tag{2.19}$$

where the symbols and units are as in equation 2.18. The 3BR process becomes important at high densities, since it requires two electrons in proximity of an ion, and at low temperature, as its rate is inversely proportional to the electron temperature. Therefore, 3BR will dominate in the late stage of the plasma, when the plume expands and cools.

**Photoionisation (PI) and radiative recombination (RR)**

In the UV laser-ablation processes, IB absorption is less efficient, but photoexcitation (PE) followed by direct PI of excited atoms in the vapor can play a significant role. The $248nm$ KrF excimer laser used in this work provides photons with an energy of $\sim 5eV$. This energy is comparable to the ionisation potential of most metals. In particular for singly ionised magnesium, the first excited level is at $2.71eV$ and the first ionisation at $7.65eV$. Therefore it is possible for bound electrons to absorbs a photon of sufficient energy so that it is ejected into the continuum, ionising the atom or ion, as illustrated in figure 2.5(b) and by the following reaction,

$$A_i^z + h\nu \Longleftrightarrow A_j^{z+1} + e \tag{2.20}$$

PI is an important process in plasmas only if the incident photon density is

high enough to induce photoionisation on a scale comparable with the electron impact ionisation. This is usually the case in optically thick plasmas, where the mean free path of the photons is shorter than the plasma dimension. A simple approximation of the PI cross section of a K-shell electron is given by Salzmann [46]

$$\sigma_{IP,K} \approx \begin{cases} 1.6 \times 10^{-8} \sigma_{Th} Z^5 \left(\frac{m_e c^2}{h\nu}\right)^{7/2} & h\nu \geq E_K \\ 0 & h\nu < E_K \end{cases}$$

where $E_K$ is the binding energy and $\sigma_{Th}$ is the Thomson scattering cross section (see equation 3.4). From this equation, it can be seen that photons with lower energy than the electron binding energy cannot ionise ions. The $532nm$ YAG laser has an energy of 2.3eV which should be low enough not to produce any PI or even PE.

The inverse process is radiative recombination (figure 2.5(b)(ii)), where an incident electron is captured into an ionic bound state and a photon is released with energy equal to the energy lost by the electron. This process will contribute as well to the continuum radiation of atomic spectra of hot plasmas. It is represented by the right-to-left reaction of equation 2.20. The radiative rates coefficient for an ion, in $cm^3 s^{-1}$ is taken from Shull and Steenberg [51]

$$\alpha_{RR}(T_e) = A_{rad} \left(\frac{T_e}{10^4}\right)^{Xrad} \qquad (cm^3 s^{-1}) \tag{2.21}$$

where $T_e$ is the electron temperature in Kelvin, $A_{rad}$ and $X_{rad}$ are radiative fitting coefficient tabulated in reference [51] for Mg ions. For the singly ionised $Mg^+$ ion, $A_{rad} = 1.40 \times 10^{-13}$ and $Xrad = 8.55 \times 10^{-1}$.

**Autoionisation and dielectronic recombination (DR)**

These two processes, illustrated in figure 2.6, both involve doubly excited states. Autoionisation occurs when an electron in the higher bound state is spontaneously excited from its energy level. The energy gained has been accepted from another electron, in the lower state, which rapidly decays from its own level into a lower state. If the energy gained by the excited electron is sufficient, the electron may be ejected into the continuum and autoionisation has occurred, as illustrated in figure 2.6(i).

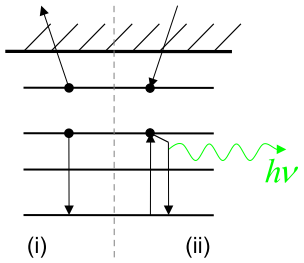


Figure 2.6: Schematic description of autoionisation and dielectronic recombination.

Dielectronic recombination, DR, is a two stage process and is not the exact inverse of autoionisation. In the first stage, an electron in the continuum recombines with an ionic bound state. The extra energy is accepted by an electron in another bound state of the ion, which is then excited to a higher bound state. A doubly excited state is then created, and so far this process corresponds to the inverse of autoionisation. In the second step, this doubly excited ion may decay, via autoionisation or through radiative decay of one of the bound levels (as shown in figure 2.6(ii)). If autoionisation follows the recombination, there is no change in the state of excitation or ionisation due to the reaction. Dielectronic recombination only occurs when radiative decay follows the recombination since, in this case, there is a change in the state of the ion. Dielectronic recombination is not often considered in experiments on laser-produced plasmas of interest in this work. The temperatures

are usually only $\sim 1-5eV$ and the densities greater than $10^{15}cm^{-3}$. Under such conditions, DR is expected to be considerably reduced [52].

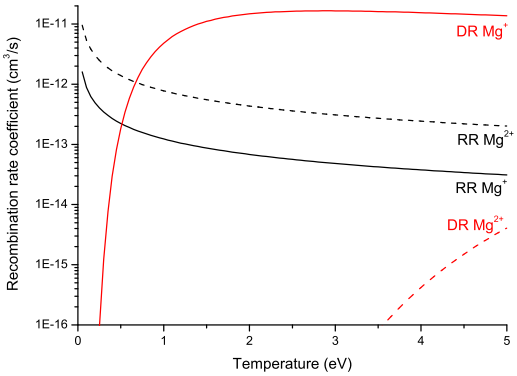


Figure 2.7: Rate coefficient for radiative recombination (RR) and dielectronic recombination (DR) calculated from Shull and Van Steenberg [51] for the $Mg^{+}$ and the $Mg^{2+}$ ions.

The analytical formula, in equation 2.22 of the dielectronic rate coefficient is given by reference [51] and used throughout this work. It provides a total rate of recombination from one ion state to another, in a quasi-static approximation, where the relative populations of excited states within an ion stage are set by collisional and radiative transitions between the levels, and ionisation and recombination from one stage to another is dealt with by global overall rates [51].

$$\alpha_{DR}(T_e) = A_{di}T^{-3/2}exp\left(\frac{-T_0}{T_e}\right)\left[1 + B_{di}exp\left(\frac{-T_1}{T_e}\right)\right] \qquad (cm^3s^{-1}) \tag{2.22}$$

where $T_e$ is the electron temperature in Kelvin. The parameters $A_{di}$, $B_{di}$, $T_0$ and $T_1$ are given in reference [51] for several ions and are the results of fitting experimental data. In particular, for $Mg^{+}$, $A_{di} = 4.49 \times 10^{-4}$,

$B_{di} = 2.10 \times 10^{-2}$, $T_0 = 5.01 \times 10^4$ and $T_1 = 2.81 \times 10^4$. Using this formula and equation 2.21, the recombination rate coefficients for the singly ionised ion of magnesium $Mg^+$ as well as the $Mg^{2+}$ ion were calculated. The result is plotted in figure 2.7 for low temperatures. It appears clearly that in the range of temperature of interest in this work $(0.5 - 2eV)$, and using the rate coefficients stated above, the DR process can be expected to be dominant over the RR process for $Mg^+$ ions. Moreover, Belic *et.al.* [53] made direct measurements of the dielectronic recombination cross section, using of crossed beams of electrons and $Mg^+$ ions. They found that the theoretical cross sections are more than a factor of 5 smaller than the ones they measured [53].

### 2.3.3 Bound-bound processes

The bound-bound transitions correspond to electronic transition in atoms or ions from one discrete energy level to another following collision with another electron, or by absorption or emission of a photon.

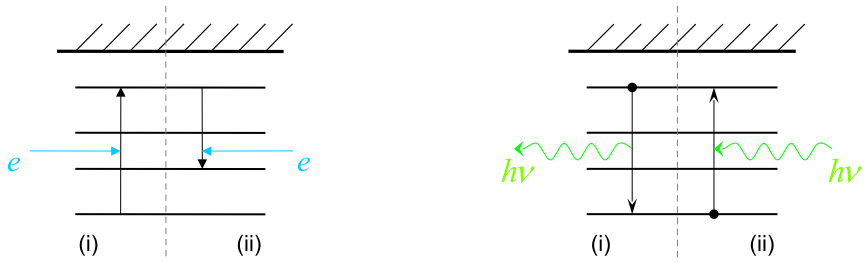


(a) electron impact excitation and de-excitation

(b) Spontaneous decay and resonant photoabsorption

Figure 2.8: Schematic description of bound-bound transitions frequent in laser-produced plasmas. (a) collisional processes and (b) radiative processes.

In the bound-bound collisional pathways, an electron moving near an

ion may induce a transition from a bound electron to a higher excited state (**electron-impact excitation**) or inversely induce a downward transition of an excited bound electron to a lower bound state (**electron-impact de-excitation**). The free electron then looses or gains kinetic energy equal to the energy difference between the upper and lower bound states. This is graphically represented by figure 2.8(a).

As shown in figure 2.8(b) the transition between bound states can be a radiative process. This is a **spontaneous decay** in which an excited ion decays into a lower state, emitting a photon with an energy equal to the difference between the upper and lower states. This radiation process is the main contribution to the spectral line emission detected in emission spectroscopy [19].

The transition probability between levels $i$ and $j$, or Einstein coefficient for spontaneous emission, $A_{j\to i}$ can be expressed using the absorption oscillator strength $f_{ij}$ as

$$A_{j\to i} = \frac{e^2\omega^2}{2\pi\varepsilon_0 m_e c^3}\frac{g_i}{g_j}f_{ij} \tag{2.23}$$

where $m_e$ is the electron mass, $g_i$ and $g_j$ are the statistical weights of the lower and upper levels, respectively.

The inverse of spontaneous decay, **resonant photoabsorption**, occurs when an electron in a bound state of an atom or ion is excited to a higher state $j$ by absorbing a photon whose energy ($h\nu = |E_i - E_j|$) matches the difference between $j$ and a lower state $i$ (see figure 2.8(b)(ii)).

## 2.4 Equilibrium in laser-produced plasmas

A plasma can be said to be in a state of complete thermodynamic equilibrium (TE) when all ions, electrons and photons are in equilibrium, which means that the rate of each process described previously equals exactly the rate of its inverse. In such a case, all of the following validity conditions should be satisfied [46]:

1. All particles; electrons, atoms and ions have a Maxwellian velocity distribution.
2. The population distributions over the states of any atom or ion are given by the Boltzmann relation.
3. The ratio of ions of charge ($z$) to those of charge ($z-1$) is given by the Saha equation.
4. The radiation intensity distribution as a function of frequency and temperature is given by the Planck formula.
5. The electron, ion and radiation temperatures are all equal.

It is very rare that laboratory plasmas approach a state of complete TE. The very fact that plasma radiates and can be otically thin prevents this from happening [54]. For this reason, more practical models, with less stringent validity requirements have been developed to best describe laboratory plasmas. The three most commonly used thermodynamic models in plasma physics are:

1. Local thermodynamic equilibrium (LTE)
2. Coronal equilibrium (CE)
3. Collisional radiative equilibrium (CRE)

The LTE model is applicable to high density, hot plasmas, and is the closest to TE. The CE model deals with low density plasmas, such as the solor corona, hence its name. Finally, the CRE model describes the intermediate density regime and overlaps with LTE and CE at its higher and lower density limits. Figure 2.9 shows the electron density requirements for valid application of LTE and CE as a function of temperature, in the region of interest in this work. The grey area covers more specifically the electron density and temperature ranges measured in this work (chapter 5). The limits are calculated considering that the atoms are no more than singly ionised in the Mg plasma under study in this thesis, using equations 2.24 and 2.30 given in the following sections.

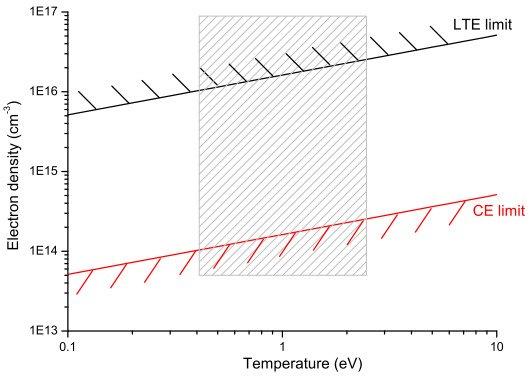


Figure 2.9: Validity range of LTE and CE models in the region of interest in this work, for singly ionised Mg plasma, calculated using equations 2.24 and 2.30. The grey area represents the area in which measurements were made in chapter 5 (cf. figures 5.18 and 5.19).

### 2.4.1 Local thermodynamic equilibrium

LTE describes a type of equilibrium in which collisional processes dominate over radiative ones. Therefore, the electron density in the plasma, must be high enough for the collision frequency to be high. This density requirement is met and deviation from LTE is less than 10% if

$$n_e \geq 1 \times 10^{14} (cm^{-3} eV^{-3}) T^3 \left(\frac{\chi_z}{T}\right)^{5/2} \tag{2.24}$$

where $\chi_z$ is the ionisation energy of charge state $z$[46]. In LTE, all particles can be described by a Maxwellian velocity distribution, a Boltzmann population distribution within each ion stage and a Saha ionisation balance. The Saha equation is given by [55, 19]

$$\frac{n_e n_{z+1}}{n_z} = \frac{2U_{z+1}(T)}{U_z(T)} \left[\frac{2\pi m_e k_B T}{h^2}\right]^{\frac{3}{2}} exp\left(\frac{-\chi_z^{eff}}{k_B T}\right) \qquad z = 0, 1, ...(Z_{max} - 1) \tag{2.25}$$

where $U_z(T)$ is the temperature dependant partition function for the ionisation stage $z$, $\chi_z^{eff}$, is the effective ionisation energy for the ionisation process $z \rightarrow (z+1)$ and $Z_{max}$ is the maximum allowed ionisation stage. The reduction of ionisation energy such as $\chi_z^{eff} = \chi_z - \Delta\chi_z$ has been derived by Griem [19]:

$$\Delta\chi_z = \frac{ze^2}{4\pi\varepsilon_0 \lambda_D} \tag{2.26}$$

where $\lambda_D$ is the Debye length given by equation 1.1. This correction is more important with high densities as $\lambda_D \propto \frac{1}{n_e}$. In the case of the plasma studied in this work ($\sim 1eV$ temperature and $\sim 10^{16} cm^{-3}$ density), it is of the order of $10^{-2}$ eV, and can therefore be neglected. Solving equation 2.25 for Mg, the ratio of each individual charge stage population $n_z$ to the total population $n_T$ of all charge stages can then be calculated as a function of temperature

using the simple relationship

$$\frac{n_z}{n_T} = n_z / \sum_{i=1}^{Z} n_i \tag{2.27}$$

The charge neutrality condition in the plasma obviously also has to be satisfied, so that

$$n_e = \sum_{i=1}^{Z} i n_i \tag{2.28}$$

Figure 2.10 shows the result of this calculation including only the first eight charge stages, and one can see that if the plasma is in LTE with a temperature of $\sim 1eV$ ground state species are expected to be dominant with maybe a small fraction of singly ionised Mg ions.

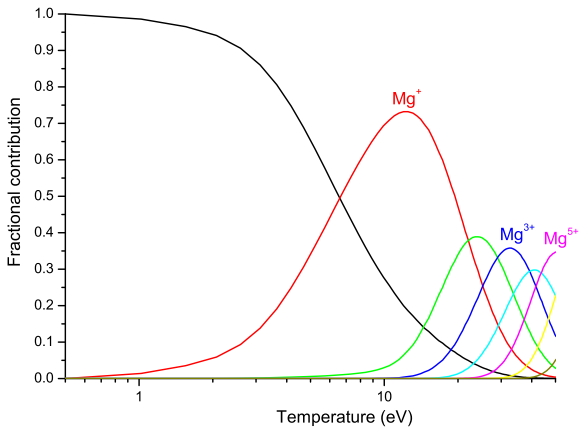


Figure 2.10: Ionisation balance of a Mg plasma as a function of temperature assuming a state of local thermodynamic equilibrium, calculated using the Saha equation (equ.2.25).

The Boltzmann distribution gives the populations of two levels $a$ and $b$, in a plasma in LTE, from the relation [19]

$$\frac{N_a}{N_b} = \frac{g_a}{g_b} exp\left(-\frac{E_a - E_b}{k_B T}\right) \tag{2.29}$$

where $g$ is the statistical weight and $(E_a - E_b)$ the energy between the two levels. Using this equation, one may calculate the relative population of a specific level from any charge stage, as described in section 5.3.

### 2.4.2 Coronal equilibrium

As shown by figure 2.9, coronal equilibrium is at the other density extreme to LTE. It is used to describe low density optically thin plasmas. Such plasmas occur frequently in astrophysical situations such as interstellar nebulae and the sun's corona, as well as in the laboratory, in tokamaks and other discharge plasmas, and in the low density portions of plumes such as the ones studied in this work. The maximum electron density allowable before CE models can no longer be used is when collisions start to interfere. This electron density can be given by [46]

$$n_e \leq 1 \times 10^{12} (cm^{-3} eV^{-3}) T^3 \left(\frac{\chi_z}{T}\right)^{5/2} \tag{2.30}$$

where the symbols used are as in equation 2.24.

In this situation, practically no collisional process will take place, an excited atom will most likely decay spontaneously before another collision occurs [54], and an ionised atom recombines by photon recombinations. The ionisation equilibrium is a balance between electron impact ionisation and two-body recombinations (radiative and dielectronic) and leads to the corona equation [46]:

$$\frac{n_{z+1}}{n_z} = \frac{S_z}{\alpha_{RR,z+1} + \alpha_{DR,z+1}} \tag{2.31}$$

where $S_z$ is the collisional ionisation coefficient corresponding to the ionic charge state $z$, $\alpha_{RR,z+1}$ and $\alpha_{DR,z+1}$ are respectively the radiative and dielectronic recombination coefficients corresponding to the ionic charge state $z+1$. Expressions for these coefficients are given in section 2.3 (equ. 2.18, 2.21

and 2.22 respectively).

### 2.4.3 Collisional Radiative Equilibrium

Collisional radiative equilibrium is applicable in the intermediate density regime, between LTE and CE. CRE is an extension of the CE model and it includes electron collision processes causing transitions between excited state levels, as well as three-body recombination. In CRE it is assumed that a Maxwellian electron velocity distribution pertains. In a steady-state CRE model, the ion densities in two consecutive charge states $n_z$ and $n_{z+1}$ are related as [50]

$$\frac{n_{z+1}}{n_z} = \frac{S_z}{\alpha_{RR,z+1} + \alpha_{DR,z+1} + n_e \alpha_{3BR,z+1}} \tag{2.32}$$

Using equation 2.32, the ionisation balance as a function of temperature was calculated in a similar maner to the LTE case. The results are plotted in figure 2.11 including only the first eight charge stages. All ionisation energies needed to calculate the collisional ionisation coefficient $S_z$ (equ.2.18) and the 3BR rate coefficient (equ.2.19) are taken from the National Institute of Science and Technology data bases [56], the RR rate coefficient and DR rate coefficient are taken from reference [51], as detailed in section 2.3.2.

## 2.5 Summary

In this section, the basic theory used during the remainder of this work was discussed as far as the expansion of the laser produced plasma goes. The fundamental plasma processes were described as well as plasma formation and expansion due to the interaction of laser radiation with matter. The complexity of the overall process was underlined. All the heating mechanism do not occur in isolation, as one process can enhance another, which in

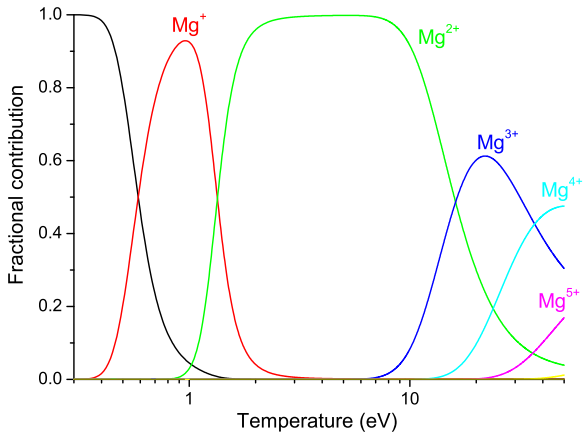


Figure 2.11: Ionisation balance of a Mg plasma as a function of temperature assuming a state of collisional radiative equilibrium, calculated using equation (equ.2.32).

turn, triggers another, and so on, hence the ungoing research work to study these plumes experimentally and theoretically. Thermodynamic equilibrium models have been discussed as they are often necessary to data interpretation.

In the next chapter, the theory of scattering by interaction of laser radiation with an expanding plasma will be outlined. We will discuss how scattering spectra may be used to determine information about density and temperature of laser produced plasmas.

# Chapter 3

# Light scattering from a plasma

*"Where observation is concerned, chance favors only the prepared mind. "*

Louis Pasteur

## 3.1 Introduction

In this chapter we consider the scattering mechanisms observed in this study, when passing laser light through a plasma: Rayleigh scattering, Thomson scattering, and Raman scattering. The three mechanisms will only be briefly explained, as a more complete theoretical approach can be found in many references in the literature [2, 31, 57, 58]. The stress is put on the application of light scattering as a diagnostic tool for plasmas. As a result, the Thomson scattering mechanisms and their applications will be described in more detail, especially for the case of low temperature laser produced plasmas; the subject of this study.

### 3.1.1 Scattering history

The study of light scattering can be said to have begun as a result of interest in the blue colour of the sky. The scattering from small dust particles in the atmosphere was first demonstrated by John Tyndall in 1869 [59]. Subsequently, Lord Rayleigh showed that the intensity of scattered light $I_s$ is related to the light wavelength $\lambda$ by

$$I_s \propto \lambda^{-4} \tag{3.1}$$

Blue radiation from the sun is scattered preferentially by molecules in the atmosphere and the result is that a cloudless sky appears blue.

In 1906, J.J. Thomson was awarded the Nobel prize for his discovery of the electron, from his studies of cathode rays, that he describes as corpuscular in nature. Further studies of the nature of these new particles led him to present a theory for the scattering of electromagnetic radiation from free electrons, the process that now carries his name.

Motivated this time by explaining the blue colour of the sea, and more consistently by extending the work of Compton in the optical regime, C.V. Raman showed experimentally in 1928 that a small amount of radiation scattered by a gas, liquid or solid is of increased or decreased wavelength. This effect is now known as the Raman Effect and is used extensively in atomic and molecular spectroscopy.

### 3.1.2 Early laser-produced plasma scattering experiments

The need for an intense monochromatic light source to produce scattering from a plasma containing a high electron density and low background meant that the phenomena was not observed until 50 years later. It is only when

lasers became available in the early 1960s that it became possible to develop Thomson scattering in laboratories. Fiocco and Thompson [60] first reported laboratory measurements of Thomson scattering from an electron beam, using a pulsed ruby laser. This was rapidly followed by observation of plasma light scattered from a theta pinch [61] and has been since developed for a variety of plasmas, including Tokamaks [62, 63], high temperature laser plasmas [64], RF discharge and arc plasmas [23, 26, 65].

However, very little work has been done on laser ablation plumes of the sort that are interesting for PLD work. Probably the first experiment that can be reported on density measurements of laser produced plasma by laser light scattering is attributed to Izawa *et.al.* in 1968 [66]. They realised a scattering experiment of a carbon plasma probed with a ruby laser $5mm$ from the target. They obtained a temporal evolution of the electron density and the carbon neutral particles density up to $15\mu s$ delay, with electron density decreasing rapidly from $10^{19}cm^{-3}$ to $10^{17}cm^{-3}$.

In 1970, T.V. George *et.al.* [67] reported Thomson scattering measurements from laser-produced aluminum plasmas using a Q-switched ruby laser delivering 3-5J in 10-15ns. The signal was recorded using a multichannel system of seven photomultipliers giving a $140\mathring{A}$ spectral window. Readings were made at six different wavelengths to obtain enough points on the spectrum to distinguish the shape of the spectrum. Average values of the electron density and temperature across the entire plasma were obtained at four different time delays between 80 and 200 ns. Most values were obtained by fitting theoretical curves. For some cases, the value of the electron density was also obtained by comparing the signal to the Rayleigh scattering of $N_2$ gas. They obtained very uncertain results with big temperature discrepancies.

Soon after, P.T. Rumsby *et.al.* [39] presented a complete study of an expanding plasma from a carbon target irradiated at $7 \times 10^{10} W cm^{-2}$. They used a range of diagnostics, including photon scattering, when the plasma had expanded 20 to 50 mm from the target surface. The scattered spectra measured were fitted to theoretical spectra to obtain $n_e$ and $T_e$. The method of calibration using the Rayleigh scattering from $N_2$ gas was also used giving electron densities in good agreement with those obtain by theoretical fitting.

The research work 40 years ago was limited by the detectors used; only allowing few points of the spectrum to be recorded at one time. However, after these papers no significant work appeared to be published on applying Thomson scattering diagnostics to diagnose low temperature laser plasmas. One reason may be that for a low temperature extended plasma, the absorption of the laser beam is a consideration, as heating of the plasma by the probe may invalidate results. This is something that will be discussed in the case of the present experiment.

## 3.2 Rayleigh scattering

The physical phenomenon of light scattering by particles of size small compared to the wavelength of the incident light, known as Rayleigh scattering, is well understood, both from a theoretical as well as an experimental perspective and is descibed extensively in the literature [2, 58, 68]. Rayleigh scattering is an elastic process and as such, the wavelength of the scattered light remains unchanged. It is also incoherent scattering due to the fact that it is coming from the bound electrons in the atoms or the ions.

The calculation of Rayleigh scattering cross-sections has been the subject of research for many years, and as a result cross-sections are well tabulated

for common gases such as Argon or Nitrogen [68]. This is particularly useful for calibrating the scattering signal from a plasma and subsequently plays a significant role in determining the electron density in a plasma during a Thomson scattering experiment. This technique will be fully described in chapter 4.

The intensity of the Rayleigh signal could also give us the density of neutral atoms and ions present in the plasma and eventually the state of ionisation if compared to the relative strength of the Thomson signal. This requires knowledge of the cross sections for ground states and excited states of the element under study. In the case of magnesium, calculations were performed at Queen's University [69] and the cross sections for the ground state of $Mg(3s^2)$ and $Mg^+(3s^1)$ states at a wavelength of $532nm$ were found to be $\sim 4.65 \times 10^{-25}\ cm^2$ and $2.19 \times 10^{-25}\ cm^2$ respectively. However, the cross section for $Mg(3s3p)$ metastable state was found to be $\sim$ 40 times higher than the ground state one. Thus the Rayleigh peak is expected to be very sensitive to the ratio of metastables to ground state. It is therefore difficult to get any relevant information on the state of ionisation without further calculations and investigations, at the time of this thesis.

## 3.3 Thomson scattering

Because of the advantages that it presents, Thomson scattering is now a long established technique for measuring electron density and temperature in many plasma experiments. To start with, it is a non-disturbing diagnostic method, as long as the probing laser is chosen appropriately. The second point is that the detected signal is relatively simple to interpret and absolute values of both the electron number density ($n_e$) and electron temperature ($T_e$) can be determined quite easily without any assumption of local thermodynamic equilibrium. Provided that the wavelength and the angle of ob-

servation are properly chosen, the spectrum of the scattered light represents a direct image of the electron velocity distribution and the scattered light intensity is directly proportional to the electron density. For these reasons, Thomson scattering is considered to be the most reliable method for measuring electron properties in a plasma.

This section contains a summary of the Thomson scattering theory and a review of the most important features relating to the application of Thomson scattering. The different calculations are not detailed, only the results are discussed as far as they will be needed for the interpretation of obtained scattered spectra.

### 3.3.1 Laser — plasma interaction

When a laser is injected into a plasma, the laser radiation scatters non-resonantly from the free and bound electrons in the plasma. In other words, the oscillating electric field of the incident beam induces the electrons in the plasma to oscillate in resonance with the field and radiates light, as illustrated in the figure 3.1 adapted from Sheffield [2]. This is, in essence, Thomson scattering.

Using the classical picture of a free electron oscillating in the electric field of a linearly polarized laser beam, the radiated power into the full solid angle of $4\pi$ is given by [31]:

$$P_S = \frac{8\pi}{3} r_e^2 I_0 \tag{3.2}$$

where $r_e = \frac{e^2}{4\pi\epsilon_0 m_e c^2}$ is the electron radius and $I_0$ is the laser beam intensity in $Wm^{-2}$.

The scattering cross-section is obtained by dividing the power scattered into the solid angle $d\Omega$ (in the direction of $k_s$ as illustrated in figure 3.2) by

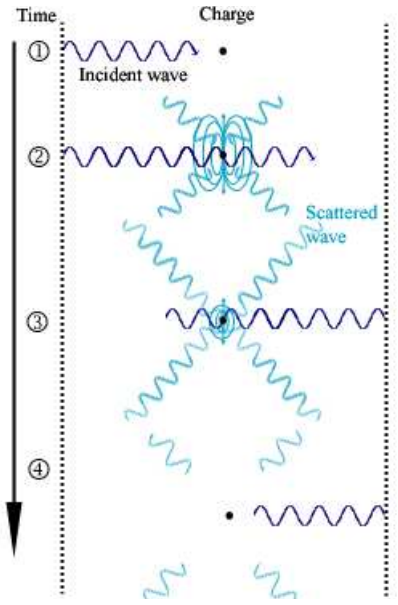


Figure 3.1: The scattering of radiation by a free charge. Illustration adapted from Sheffield [2].

the incident power per unit area. In the case of polarized incident radiation it can be expressed as:

$$\frac{d\sigma}{d\Omega} = r_0^2(1 - \sin^2\theta\cos^2\varphi) \tag{3.3}$$

Observing equation 3.3, it is interesting to note that the scattering is maximum in a plane perpendicular to $E_0$ when $\varphi = 90°$.

Integrating over the entire solid angle, the total Thomson scattering cross-section is found to be [2]:

$$\sigma_{Th} = \frac{8\pi}{3}r_e^2 = 6.65 \times 10^{-29}m^2 \tag{3.4}$$

The exceedingly small value of the cross-section explains why Thomson scattering is difficult to detect. Even with a powerful source, low electron number densities are difficult to detect. Any other source of light, stray light, plasma background emission, has to be as minimum as possible to make any valuable measurement. This point is disscussed in practice in the following chapters.

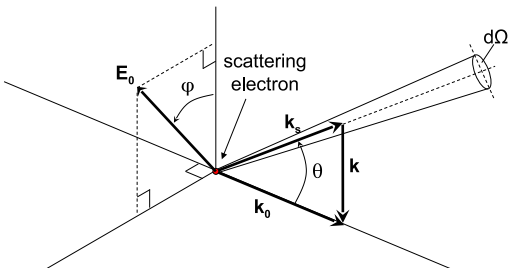


Figure 3.2: Scattering geometry showing the wave vectors $k_0$ and $k_s$ of the incident and the scattered wave, respectively, the electric field polarisation and the detected solid angle $d\Omega$.

The wavelength of scattered radiation that reaches a detector is doubly Doppler shifted because the radiating charge is moving rapidly with respect to both the laser beam and the detector. In practice, reliable measurements of the Thomson scattering spectrum can be obtained from the wings of the signal, where there is no significant contribution from the Rayleigh scattering and the stray light.

We can define a scattering vector $k = k_s - k_0$ as the difference between the wave vectors of the scattered and the incident waves (see figure 3.2). In the non-relativistic case, the velocity of the scattered particle being small compared to the speed of light, the magnitude of $\mathbf{k}$ can be expressed as a function of the laser wavelength $\lambda_0$, and the detection angle $\theta$ between $\mathbf{k}_0$ and $\mathbf{k}_s$.

$$|\mathbf{k}| = k \cong \frac{4\pi}{\lambda_0} \sin\frac{\theta}{2} \tag{3.5}$$

And the Doppler shift can be expressed as [2, 31]

$$\Delta\lambda = \lambda - \lambda_0 = -\frac{(\mathbf{k} \bullet v)\lambda_0^2}{2\pi c} \tag{3.6}$$

where $\lambda_0$ is the wavelength of the incident laser radiation, $v$ is the velocity of the scatterering electron, $\lambda$ is the scattered wavelength, and $c$ is the speed of light.

The differential scattering vector $\mathbf{k}$ and the Debye length $\lambda_D$ are the two most important parameters that govern the shape of a Thomson scattering spectrum. They are combined to define the scattering parameter, $\alpha$:

$$\alpha = \frac{1}{k\lambda_D} = \frac{\lambda_0}{\sin\left(\frac{\theta}{2}\right)} \left\{ \frac{n_e e^2}{4\pi k_B T_e} \right\}^{\frac{1}{2}} \tag{3.7}$$

The value of $\alpha$, which is clearly affected by the laser wavelength, the electron temperature, the number density, and the scattering geometry, determines the character of the scattering observed in a particular experiment. Different scattering regime will produce different spectra. Typical scatter spectra are shown in figure 3.3 for values of $\alpha$ both less than and greater than unity for typical plasma conditions in a low temperature laser-plume.

- figure 3.3(a): $\alpha \ll 1$ The two ways of looking at this case are if k is large, so the resolution is high and individual electrons can be seen, and $\lambda_D$ is large so plasma effects are important. In other words, the effect of individual electrons are important. The phases of the waves arriving at the different electrons is random as will be the phases of their scattered waves. The scattering is *incoherent*.

- figure 3.3(c): $\alpha \gg 1$ the incident wave interacts with the shielded charges, causing them to undergo group motion and producing what is known as *coherent scattering*.

As a result, it is important to consider the value of $\alpha$ for an experiment, and for a given plasma with particular values of $n_e$ and $T_e$, $\alpha$ can be adjusted by changing the incident laser wavelength or the detection angle $\theta$.

The scattered spectrum is usually written in terms of the spectral density function $S(\mathbf{k}, \omega)$, which is a function of the wave vector $\mathbf{k}$, $\alpha$, the frequency $\omega$ and plasma properties, including the electron temperature, and the ion temperature. It describes the frequency shifts resulting from electron motion, and the effect of correlations between electrons when $\alpha > 1$. The form of the spectral density function is complex, and detailed derivation of the function can be found in [2]. In this work, we used formulas of the structure factor derived by Sheffield [2] in the case of an unmagnetised, collisionless, stable, low-temperature plasma. The Salpeter approximation was then used to obtain simulated spectra for different plasma conditions, as explained in the following section.

### 3.3.2 Salpeter approximation

This section briefly outlines how the scattered spectra was simulated using the Salpeter approximation. These theoretical spectra were then fitted to the experimental Thomson spectra measured in this work to obtain the electron density and temperature of the plasma plumes under study. The reader is refered to chapter 7 of Sheffield textbook [2] on scattering from a low-temperature stable plasma for a more detailed derivation of the following formulas.

The structure factor can be expressed as the sum of the electron feature and the ion feature [70]

$$S(\mathbf{k},\omega) = S_e\left(\frac{\omega}{\sqrt{2k^2\kappa_B\frac{T_e}{m_e}}}, \alpha(k, n_e, T_e)\right) + S_i\left(\frac{\omega}{\sqrt{2k^2\kappa_B\frac{T_i}{M}}}, Z, \frac{T_e}{T_i}\alpha(k, n_e, T_e)\right) \tag{3.8}$$

and is a function of the electron density $N_e$, the electron $T_e$ and the shift in wavenumber $\mathbf{k} = \mathbf{k}_s - \mathbf{k}_0$ given by equation 3.5. Where M is the ion mass,

$T_i$ the ion temperature, Z the charge of the ions, $m_e$ the electron mass, and $\omega$ the shift in frequency. $S_e$, the electron feature, contains the fluctuations of electrons which move freely, and $S_i$ the ion feature, contains the fluctuation of electrons which are correlated with the motion of the ions. In the case of our experiment, the ion feature is not resolvable and plays a negligible role. Only the electron feature is considered in the theoretical calculation.

In the case where $\frac{T_e}{T_i} \cong 1$ Salpeter has shown that the spectrum takes a relatively simple form. Sheffield derives the expression of the electron feature as

$$S_e(\mathbf{k},\omega) \cong \frac{2\pi^{\frac{1}{2}} exp(-x_e^2)}{ka[(1+\alpha^2 Rw(x_e))^2 + (\alpha^2 Iw(x_e))^2]} \tag{3.9}$$

where a is the thermal velocity of the particles,

$$a = \left(\frac{2\kappa_B T_e}{m_e}\right)^{\frac{1}{2}} \qquad x_e = \frac{\omega}{ka} \tag{3.10}$$

$$\alpha = \frac{1}{k\lambda_D} \qquad \lambda_D = \left(\frac{\epsilon_0 \kappa_B T_e}{e^2 n_e}\right)^{\frac{1}{2}} = 743 \times \left[\frac{T_e(eV)}{n_e(cm^{-3})}\right]^{\frac{1}{2}} \tag{3.11}$$

The expression of Rw(x) and Iw(x) can be found in Fried and Conte [71]. For a collisionless plasma, the imaginary part, the Landau damping term is

$$Iw(x) = \pi^{\frac{1}{2}} x exp(-x^2) \tag{3.12}$$

For real x,

For $x < 1$, i.e., $\omega/k < a$

$$Rw(x) \cong 1 - 2x^2\left[1 - \frac{2x^2}{3} + \frac{4x^4}{15} - \frac{8x^6}{105} + ...\right] \tag{3.13}$$

For $x \geq 1$

$$Rw(x) \cong 1 - (3.1052 - 12.206x + 22.492x^2 - 18.7844x^3 + \\ + 8.0544x^4 - 1.7418x^5 + 0.15119x^6 - ...) \quad (3.14)$$

For $x \gg 1$

$$Rw(x) \cong -\frac{1}{2x^2}\left[1 + \frac{3}{2x^2} + \frac{15}{4x^4} + ...\right] \quad (3.15)$$

The spectral density function is plotted as a function of the frequency shift $\omega = x_e ka$ or the wavelength shift $\lambda = \frac{\omega\lambda_0^2}{2\pi c}$.

The shape of the spectral density function for various values of the scattering parameter $\alpha$ has been plotted using the Saltpeter approximation on figure 3.3. In this case the electron temperature and the ion temperature have been set to $T_e = T_i = 1eV$, the view angle to 90 degrees, and the probe wavelength to 532 nm. These parameters are close to the experimental conditions at Queen's University. The ion component of the structure factor is not shown in figure 3.3 since it's a very narrow feature ($\sim 0.01nm$) and is not resolvable in the plasma we are interested in. Figure 3.3 illustrates that for $\alpha \gg 1$, the electron component is very small, except for a resonance due to the plasmon oscillations in the plasma. The position of the peak is the plasma frequency away from the incident light frequency and is given by:

$$\omega^2 = \omega_p^2 + \frac{3k_B T_e k^2}{m} \quad (3.16)$$

The overall level of scatter is proportional to the electron density.

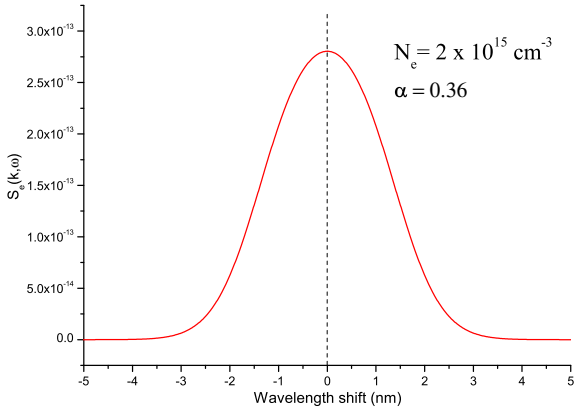


(a) $\alpha = 0.36$

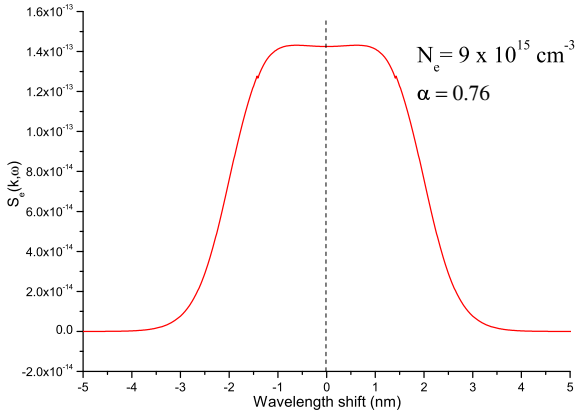


(b) $\alpha = 0.76$

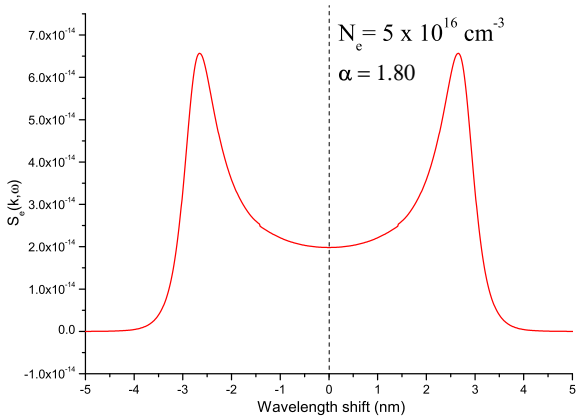


(c) $\alpha = 1.80$

Figure 3.3: Scattered spectra calculated using the Salpeter approximation and equation 3.9, for three different values of $\alpha$ obtained by varying the density, with same view angle of 90 degrees, $T_e = T_i = 1eV$, the probe wavelength $532nm$, and for a magnesium plasma.

## 3.4 Calculating $n_e$ and $T_e$ when $\alpha \ll 1$

### 3.4.1 Electron temperature

Assuming a Maxwellian distribution function for the electrons, the scattered power from an electron into a solid angle $d\Omega$ can be expressed in terms of $\Delta\lambda = \lambda_S - \lambda_i$ as [2]:

$$\begin{aligned} P_S(\mathbf{R},\lambda_S)d\lambda_S d\Omega &= \frac{P_i r_0^2 d\Omega n_e L}{2\pi^{1/2} sin(\theta/2)} \left[\hat{S}\times(\hat{S}\times\hat{E}_{i0})\right]^2 \\ &\quad \cdot \frac{c}{a} exp\left\{\frac{-c^2\Delta\lambda^2}{4a^2\lambda_i^2 sin^2(\theta/2)}\right\}\frac{d\lambda_S}{\lambda_i} \end{aligned} \tag{3.17}$$

where $\mathbf{R}$ is the position vector of observation point from origin, $\lambda_S$ the scattered wavelength, $\lambda_i$ the incident wavelength, $P_i$ the incident power, $r_0$ the classical electron radius, $L$ the length of scattering volume, $\theta$ the scattering angle, and $c$ the speed of light.

Since the incident radiation in the present experiment is polarized, the factor

$$\left[\hat{S}\times(\hat{S}\times\hat{E}_{i0})\right]^2 = 1 - sin^2\theta cos^2\varphi \tag{3.18}$$

where $\varphi$ is shown on figure 3.2.

Substituting $\alpha$ (from expression 3.7) and expression 3.18 in equation 3.17, we have:

$$\begin{aligned} P_S(\mathbf{R},\lambda_S) &= \frac{P_i r_0^2 n_e L c m_e^{1/2}}{2k^{1/2}\lambda_i sin(\theta/2)}\left(1 - sin^2\theta cos^2\varphi\right) \\ &\quad \cdot \frac{1}{\sqrt{2\pi}\sqrt{T_e}} exp\left\{\left[\frac{-c^2 m_e}{8k\lambda_i^2 sin^2(\theta/2)}\right]\left(\frac{\lambda-\lambda_i}{\sqrt{T_e}}\right)^2\right\} \end{aligned} \tag{3.19}$$

The equation of a normalised Gaussian can be expressed as:

$$y = \frac{1}{\sigma\sqrt{2\pi}} exp\left\{-\frac{1}{2}\left(\frac{x-x_0}{\sigma}\right)^2\right\} \tag{3.20}$$

where the Half Width Half Maximum (HWHM) $x_{HWHM} = \sqrt{2ln2}\sigma$.

If we introduce two constants $C_1$ and $C_2$, equation 3.19 can be rewritten as:

$$P_S = \frac{C_1}{\sqrt{2\pi}\sqrt{T_e}} exp\left\{-C_2\left(\frac{\lambda - \lambda_i}{\sqrt{T_e}}\right)^2\right\} \tag{3.21}$$

The comparison of the expression of a normalised Gaussian 3.20 and the rewritten expression of the scattered power 3.21 is clear, and by considering the terms in the exponentials $\left(-\frac{C_2}{T_e}\right)$ is directly equivalent to $\left(-\frac{1}{2\sigma^2}\right)$.

An expression of the electron temperature in eV ($kT_e$) can be deduced as a function of the HWHM of the Gaussian shaped scattered signal, $x_{HWHM}$:

$$kT_e = \frac{m_e c^2}{2ln2}\left(\frac{x_{HWHM}}{2\lambda_i sin(\theta/2)}\right)^2 \tag{3.22}$$

### 3.4.2 Electron density

The total scattered light intensity is directly proportional to the electron density $n_e$.Therefore, with an absolute calibration of the intensity axis, accurate value of $n_e$ could be determined. In practice, this calibration can be done using Rayleigh scattering from a cold gas, by filling the vaccum chamber with a cold gas of known pressure instead of the plasma. In this situation, the scattered signal intensities $I_p$, from a plasma of electron density $n_e$, and $I_g$, from the cold gas of density $n_g$, are given by:

$$I_p = n_e \sigma_{Th} \Delta\lambda_p f_{system} \tag{3.23}$$

and

$$I_g = n_g \sigma_{Ray} \Delta\lambda_g f_{system} \tag{3.24}$$

Where $\sigma_{Th}$ is the differential cross section for Thomson scattering, given in 3.4, $\sigma_{Ray}$ the cross section for Rayleigh scattering of the calibration gas, $\Delta\lambda_p$ and $\Delta\lambda_g$ are the spectral widths of the scattered spectra from the plasma and the gas, and $f_{system}$ is a function of the probing laser energy and the efficiency of the detection system. If both measurements are made using the same laser, collection optics and detection systems, $f_{system}$ is the same in both cases. In practice, the electron density in the plasma can be deduced by comparing the total area under the scattering curves:

$$n_e = n_g \frac{\sigma_{Ray}}{\sigma_{Th}} \frac{A_{Th}}{A_{Ray}} \tag{3.25}$$

The ratio of the Rayleigh to Thomson scattering cross section $\frac{\sigma_{Ray}}{\sigma_{Th}}$ is known for a number of gases [68]. $A_{Th}$ and $A_{Ray}$ refer to the total area under the Thomson and the Rayleigh scattering signals respectively.

## 3.5 Raman scattering

When atoms or molecules are irradiated by non-resonant radiation, a fraction of the radiation is scattered elastically. This is known as Rayleigh scattering (described in section 3.2) with no wavelength changes. A much smaller fraction of the atoms or molecules can be scattered inelastically. This is called the Raman effect, and the scattered radiation with decreased or increased wavelength is referred to as Stokes and anti-Stokes Raman scattering respectively. It is molecules that are much more frequently involved in Raman scattering processes [58] and as such only few references refer to Raman scattering of atoms [72].

The difference in energy observed between the incident and scattered

photons is made up by a change in the excitation energy (rotational, vibrational or even electronic) of the atom or molecule. Raman scattering can be seen with virtual levels that mediate the scattering, as shown in figure 3.4. The atom is excited by absorption of a photon to a virtual level of extremely small lifetime. The atom decays instantaneously by emission of a second photon to its original state (Rayleigh scattering), or to a different state (Raman scattering).

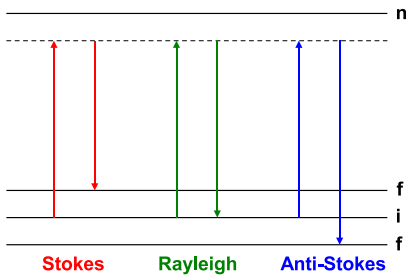


Figure 3.4: Rayleigh and Raman scattering. The dash-line represent a virtual level at some distance from a real level n.

It was found during this experimental work that Raman scattering could potentially be a useful diagnostic in plasma physics to infer the density of a particular atom if the cross section is known (see chapter 5). In the case of magnesium plumes studied in this work, the density of Mg atoms in the metastable first excited state could be inferred from the satellites produced by Raman scattering. Theoretical work is ongoing at the time of writing to calculate the expected cross-sections.

Figure 3.5 shows first results of calculations done at Queen's University [69] for the metastable $Mg$ $(3s3p)$ states. The total cross-section for Rayleigh and Raman scattering are indicated as a function of energy, and

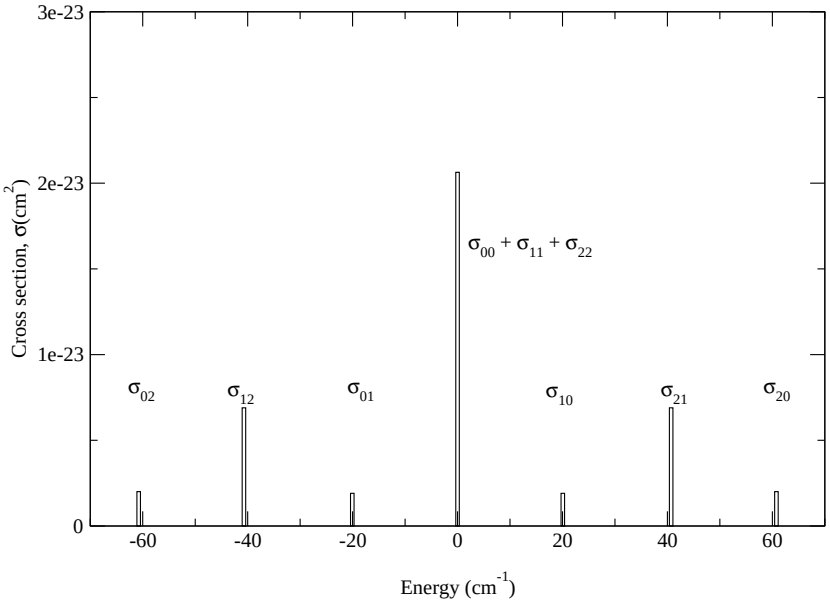


Figure 3.5: Calculated cross-sections of Rayleigh and Raman scatter from metastable $Mg$ $(3s3p)$ states, $J = 0, 1, 2$ with an incident energy corresponding to a wavelength of $532nm$ [69].

their exact values are summarised in table 3.1. The central peak at 0 is the Rayleigh scattering cross-section, the Raman satellites are shown on either side. The cross-sections $\sigma_{JJ'}$ were obtained by considering the transitions from $J = 0, 1, 2$ to $J' = 0, 1, 2$ at an incident energy of $2.33eV$ corresponding to a wavelength of $532nm$.

Calculations of the Rayleigh scattering cross-sections for the ground state of $Mg$ $(3s^2)$ at the same energy was found to be 40 times smaller than the one for metastables [69]. These results will be discussed further in section 5.3.2, in view of the experimental scattering results.

Table 3.1: Rayleigh and Raman scattering cross-sections of metastable states of Mg atom at an incident energy of $2.33eV$.

| Energy ($cm^{-1}$) | Cross-section $\sigma$ ($cm^2$) | Transition $J \leftrightarrow J'$ | Scattering mechanism |
|---|---|---|---|
| 0 | $2.06 \times 10^{-23}$ | $0 \leftrightarrow 0$ ; $1 \leftrightarrow 1$ ; $2 \leftrightarrow 2$ | Rayleigh |
| $\pm 20$ | $1.91 \times 10^{-24}$ | $0 \leftrightarrow 1$ | Raman |
| $\pm 40$ | $6.90 \times 10^{-24}$ | $1 \leftrightarrow 2$ | Raman |
| $\pm 60$ | $2.01 \times 10^{-24}$ | $0 \leftrightarrow 2$ | Raman |

## 3.6 Summary

In this chapter we have discussed the light scattering phenomena observed during the experimental work of this thesis. The theory necessary to use these scattering phenomena as plasma diagnostics was reviewed.

In the next chapter, the experimental system will be described in detail, from the target ablation set-up to the diagnostic system. The aim will be to show the steps that had to be followed to set up a Thomson scattering experiment for laser ablated plumes, and the problems that had to be overcome working with laser plasmas compare to previous experiments with other types of plasmas.

# Chapter 4

# Scattering experimental set-up


"Rouxel, *Philosophie Shadok*[1]"

The transient nature of laser-produced plasmas, with steep density and temperature gradients, high expansion velocities and small volumes compared with other plasmas, make them challenging entities to study using a Thomson scattering diagnostic. In order to detect enough signal to track the evolution of laser-produced plasmas, significant demands are placed on the experimental equipment; high temporal, spatial and spectral resolution is

[1]By continuously trying, you eventually succeed. So: the more it fails, the more likely it is to start working.

required, in order to discriminate any unwanted signal, and obtain relevant information about the plume.

The understanding of the complex processes that occur in such plumes relies as well on measurements to be made under well controlled irradiation conditions. This chapter will first give a brief outline of the system used for producing the laser ablated plume. More details will then be given on the Thomson scattering diagnostic system which includes a description of the probing laser characteristics and focusing, the alignment, noise reduction issues and timing of the experiment. The scattered spectra were recorded with a double grating spectrometer and a gated intensified CCD (ICCD). Details and specifications of the detection system will be discussed below.

## 4.1 Laser ablation

The laser ablation apparatus used in this work was adapted from previous research works and further details of some aspects of the laser ablation set-up can be found in previous theses [9, 10, 12, 13]. However, a completely new experimental configuration had to be set up to implement the Thomson scattering diagnostic. A vacuum chamber more appropriate to the diagnostic was used (see section 4.1.1) and the ablation laser was incident normal to the target. This configuration facilitated the alignment procedure to probe different part of the plasma plumes (see section 4.2.5). A schematic of the experimental set-up to produce the plasma is presented in figure 4.1.

### 4.1.1 Vacuum system and targets

The vacuum system consists of a cylindrical stainless steel chamber approximately 350 mm in height and with a diameter of 470 mm, with 8 entrance tubes (see figure 4.1). This chamber was choosen for its advantages for set-

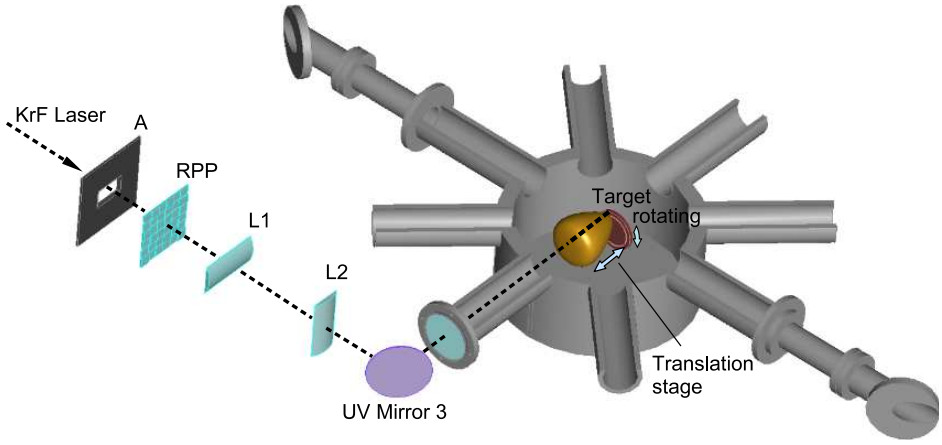


Figure 4.1: Schematic of experimental set-up for plasma plume production. In the excimer laser beam path, components include aperture (A), Random Phase Plate (RPP), cylindrical lenses (L1 and L2). The target is rotating and can be translated along the axis of the laser beam.

ting up a Thomson scattering experiment: a larger chamber reduces the reflections from the chamber walls, and the tubes can be used to install baffles along the probing laser direction. All these points are detailed in section 4.2.2 when discussing the stray light reduction in such an experiment. The chamber has various ports fitted with different windows depending on their function: a quartz window for access of the UV ablation laser, quartz windows at Brewster angle for the probing beam, and a BK7 glass window in the top viewing port. It is evacuated to a pressure less than $1 \times 10^{-4}$ mbar by a turbo-pumping unit (model TW 250 s, Leybold) backed by an oil free two-stage vacuum pump (model SC 5D, Leybold). The turbo was water cooled constantly throughout the experiment. The pressure was measured using a full range gauge (model PKR 261, Pfeiffer Vacuum)

The targets were cut into the form of a disk, mounted on a rotating spin-

dle inside the vacuum chamber. Single element metallic targets were used, magnesium (purity 99.9%) and aluminum (90% purity). The targets were polished just before being placed in vacuum to get a surface as flat and clean of impurities as possible. The target was mounted on a linear translation stage (model Zaber technologies, T-CON3) and could be moved along the beam axis with a precision of $< 50\mu m$. The ablating laser beam was incident normal to the target so that the position of the plasma plume was not moving when the target was translated along the axis of that laser. The laser spot on target was off centered by over a centimeter and the target rotated to avoid overlap of successive laser pulses. This was creating a circular track on the target surface that had to be repolished after $\sim$ 20000 *shots* so not to crater the target, which would then change the condition of the plasma formation (see section 2.1.1).

### 4.1.2 KrF excimer laser

The plasma plume was created with a Lambda Physik 210i krypton fluoride excimer laser system. Its important parameters have been summarised in table 4.1. It consists of a laser head, a power supply unit, a gas handling system, all computer controlled. The gas mixture used consists of 150 mbar of rare gas (krypton, $>$ 99.995% purity, Spectral Gases Ltd), 70mbar of halogen gas (fluorine $>$ 99.9% purity, 5% fuorine in helium, Spectra Gases) completed up to 3000 mbar by a buffer gas (neon, $>$ 99.995% purity, Spectral Gases Ltd). The gas mixture is excited by a fast electrical discharge to create ionic and electrically excited species that react and produce the excimer molecules KrF*. Transitions between a bound excited KrF* complex and a weakly bound ground state provide the ultra-violet laser pulse at 248nm.

The temporal profile of the typical laser pulse was measured with a

Table 4.1: Specifications Lambda Physics KrF excimer laser.

| | |
|---|---|
| Lasing medium | gas mix: Krypton, Fluorine and Neon |
| Wavelength | 248 nm |
| Energy/pulse | up to 320 mJ |
| Pulse length (FWHM) | 20 ns |
| Repetition rate | 10 Hz |
| Trigger jitter | $< 5ns$ |

fast diode (1ns raise time) and is shown in Figure 4.2. When operated at a repetition rate of 10Hz and a constant input voltage of 24 kV, the laser outputs a pulse of 20ns (FWHM) with an energy up to 320mJ. The output obtained from the laser is rectangular ($\sim$ 20mm x 9mm). The central most uniform section of this beam is selected using an aperture (18mm x 8mm), shown in figure 4.1. The pulse energy of the output beam was monitored using a Gentec calorimeter calibrated by the manufacturer in the UV with $2.82V/J$. The output energy was measured daily before and after a set of measurements and no more than 5% loss of energy was measured during a day of run. The energy was dropping with the number of shots fired using a given gas fill due to the depletion of fluorine in the gas mixture. To maintain the energy constant from day to day over the course of an experimental run, a small quantity of fluorine mix was added ($\sim 15mbar$) to the cavity mix. After a period of prolonged use, impurities were building up in the system, making the energy drop as well. The cavity mirrors had to be cleaned and realigned and consequently, the gas mix had to be replaced. The use of a gas purifier (Model GP2000, Oxford Instruments Ltd.) prolongated the time a same gas mix could be used. The gas purifier was running with liquid nitrogen to freeze out the impurities produced in the laser head.

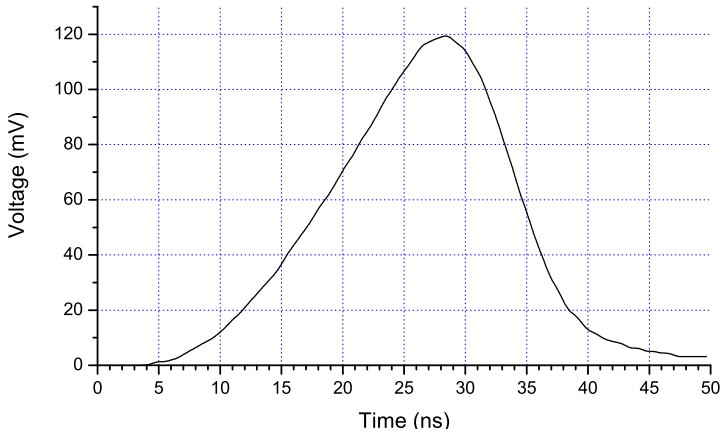


Figure 4.2: Typical temporal profile of the excimer laser pulse used in this study. The voltage is measured with a photo-diode detector.

### 4.1.3 Ablation optical system

The beam was directed into the target chamber by three high reflectance dielectric mirrors (mirror 1: 99%, mirror 2: 90% and mirror 3: 90% reflection for a 248nm beam incident at 45°) directing about 60% of the laser output energy on target. The laser spot was then focused on the target using two quartz plano-convex cylindrical lenses of focal lens $\sim 69cm$ (L2) and $\sim 94cm$ (L1). Their optical axes are aligned perpendicular to the laser beam and orthogonal with respect to each other. In this configuration, the horizontal and the vertical dimension of the ablation spot can be controlled independently by moving these two lenses. A uniform intensity distribution of the laser spot was obtained by using a random phase plate (RPP) [73]. A random phase plate is a binary diffractive optics which enlarges a focal spot whilst imposing a smooth spatial profile. It consists of randomly distributed elements of phase 0 or pi etched onto a flat substrate to a depth $D = \frac{\lambda}{2(n-1)}$, where $\lambda$ is the laser wavelength and n is the refractive index of the substrate. The equal areas of 0 and $\pi$ destructively interfere exactly on axis, and the

energy contained within large scale beam hot spot is transformed into a high spatial frequency speckle pattern in the far field of the focusing lens. The RPP used in the lab contains a 3x3 array of 9 different RPP designs to provide a wide range of spot sizes on target. Each RPP is a 25mm square containing rectangular pixels with dimensions from $200\mu m$ to $700\mu m$. Detailed study of the effect of the RPP on similar KrF laser focal spot to the one used in this study can be found in reference [10]. The focusing optics was adjusted to obtain a spot of $\sim 1.5 \times 1.5mm^2$ giving a fluence on target of $\sim 10Jcm^{-2}$.

## 4.2 Thomson scattering diagnostic

In this section, the experimental arrangement and techniques used to implement a Thomson scattering diagnostic in laser produced plasma are discussed. An overview of the diagnostic set up is shown in figure 4.3. There are six main aspects influencing a Thomson scatter experiment. Each of these aspects will be discussed individually in the following sub-sections, they are:

1. Which probing laser?
2. How to reduce the stray light?
3. The optical spectrometer
4. Which detector?
5. How to align and calibrate the system?
6. Synchronisation of the ablating laser, probing laser and detection system

An overview of the Thomson scattering diagnostic set up is shown in figure 4.3. The scatter signal is collected at 90° and exits through the top flange of the chamber. It is focused into the slit of a double grating spectrometer,

and the spectrum is then detected with a gated intensified charge coupled device (ICCD).

### 4.2.1 Probing laser

The light source used to scatter electrons in the plasma was a Spectra Physics GCR-4 Nd:YAG pulsed laser. Table 4.2 summarises the important parameters relating to the Spectra Physics Nd:YAG laser. This is a Q-switched laser system, and the laser medium is a rod crystalline yttrium aluminium garnet ($Y_2Al_{12}O_{12}$) doped with neodymium ions ($Nd^{3+}$), leading to the abreviation Nd:YAG. $Nd^{3+}$ ions are pumped optically into their upper states using a flashlamp and lasing occurs for transitions at $1.06\mu$. The laser used in this study is using a Q-switching technique to allow the population inversion to build up in the Nd:YAG rod producing $\sim 1J/pulse$. Both the flashlamp and the Pockels cell were triggered externally by two TTL pulses to reduce the jitter. The jitter measured in that configuration was $< 10ns$. Details about the triggering system can be found in section 4.2.6. The maximum output signal was found for a delay of $229\mu s$ between the flashlamp and the Pockels cell trigger. The laser was water cooled during operation to prevent the laser rod from overheating from the large amount of heat dissipated by the flashtube.

A Quanta Ray HG-4 harmonic generator installed within the laser housing held a crystal to produce the second harmonic at 532 nm. Maximum conversion efficiency (approximately 50%) was achieved by tuning the crystal to the optimum angle giving an output pulse energy up to $500mJ$. All experiments were preformed using the second harmonic beam. Rotation of the main housing of the crystal about the optical axis changed the polarisation of the output laser beam. Since the Thomson scatter signal is maximum when the polarisation of the probing beam is perpendicular to the scattering

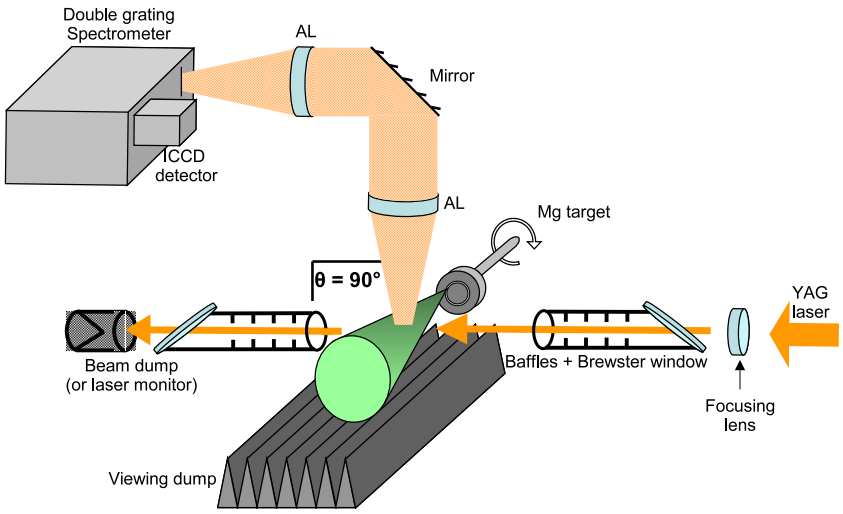


Figure 4.3: Schematic of set-up for Thomson scatter. The scattered signal is collected at 90° from the probing beam axis using two achromatic lenses (AL). The angle of the Brewster window is only for representation.

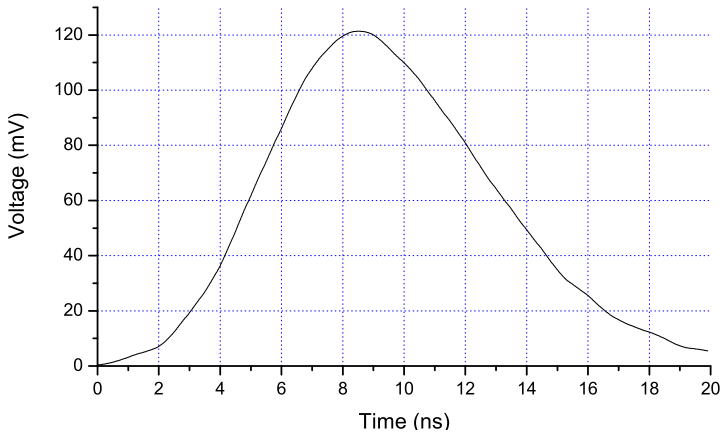


Figure 4.4: Typical temporal profile of the Nd:YAG laser pulse used in this study. The voltage is given by a photo-diode detector.

plane (see section 3.3.1), the YAG laser polarisation was set to be horizontal.

Table 4.2: Specifications Spectra Physics GCR-4 Nd:YAG laser .

| Lasing medium | Nd:YAG | |
|---|---|---|
| | fundamental | $2^{nd}$ harmonic |
| Wavelength (nm) | 1064 | 532 |
| Energy (J)/pulse | 1 | 0.5 |
| Pulse length (FWHM) | 9 ns | |
| Repetition rate | 10 Hz | |
| Trigger jitter | $< 10ns$ | |

The laser beam was directed into the chamber using three dielectric mirrors (99% reflection at 45 degrees) and loosely focused (f/200) using a lens of 1 meter focal length. The focal spot was $\sim 0.5mm$ FWHM giving a fluence of $\sim 50J/cm^2$. The perturbation of the plasma that such a probe might generate is investigated and discussed in the following chapter. In order to be able to control the intensity of the laser beam, a half wave plate and a polariser were used. The polariser was set for a horizontally polarised signal, and by rotating the half wave plate, placed before the polariser, the polarisation of the beam could be rotated, and the intensity of the beam after the polariser could then be controlled.

### 4.2.2 Noise reduction

One of the most critical aspect of a Thomson scattering experiment is background noise reduction. As discussed in section 3.3.1 the Thomson cross-section of an electron is very small, causing a Thomson scattering spectrum to be very weak. The three factors to take into account in the background

noise in such an experiment are:

- stray light
- Rayleigh scattering
- background plasma emission

The plasma emission can be present at all wavelengths and for higher temperature and density can have significant effects on the Thomson scattering measurements. Several measures were taken to encounter this effect:

- The probing laser wavelength, and the target element were chosen so that there was no intense line radiation in the wavelength region of interest.
- The detector was gated to the pulse length of the probing laser (10ns) to limit the detection to the time when scattering occurs (see section 4.2.6).
- Frequent background measurements with the ablation laser on and the probing laser off were taken. These backgrounds of plasma emission signal were then substracted from the scattering signal (see chapter 5).

Stray light and Rayleigh scattering are both limited to a narrow wavelength range, so the Thomson scatter signal can be deduced from the wings of the scattered signal. However if the signal of the central wavelength is too strong, it can affect the adjacent wavelength region, especially at lower density and temperature when the Thomson scatter signal is weaker and narrower. The Thomson signal being weak, it is necessary to accumulate the signal over several laser shots. If the other signals are too strong, the detection system saturates before any Thomson signal is detectable. In the case of a laser produced plasma, the Rayleigh scattering signal cannot be

measured independently like in gas discharge experiments [74]. As a result, great care was taken to equip the chamber with opaque material and apparatus to reduce the stray light. These apparatus are represented in figure 4.5 and detailed in the following paragraphs.

The laser beam enters and leaves the chamber in which the plasma is created, through vacuum windows. Transmission through these windows, and reflection from these windows generates stray light. Both entrance and exit windows are placed at the Brewster angle to reduce this stray light (see figure 4.5(a)). Since the probing laser beam is horizontally polarized, the Brewster windows were arranged to minimise back reflections. The windows are also placed at the end of long entrance and exit tubes to distance the windows from the plasma. Both entrance and exit tubes were fitted with apertures of different sizes to act as baffles, from 12 mm further away from plasma to 8 mm closer to the plasma. The entrance and exit tubes were threaded and blackened close to the Brewster windows (see 4.5(c)) to trap any reflection. The probe beam was then dumped in a beam dump outside the chamber. This beam dump was replaced by a power meter before and after any set of data was taken. Figure 4.5(b) shows how cones were inserted to reduce reflection from the chamber walls. Any stray light reduction apparatus inside the chamber was blackened using vacuum compatible matt black paint (aquadag) or anodised if the pieces were made of aluminum (apertures, window flanges, threaded tube). Another important aspect of the stray-light reduction is the need for the background of the viewing area of the detector to be completely black. This was accomplished with a viewing dump opposite the detection angle shown on figure 4.5(d). Recycled heat sinks from computer CPUs stacked together and painted matt black were used. This was a quick and low cost way of obtaining a wedge type viewing dump. Great care was taken as well to keep all the optical components clean

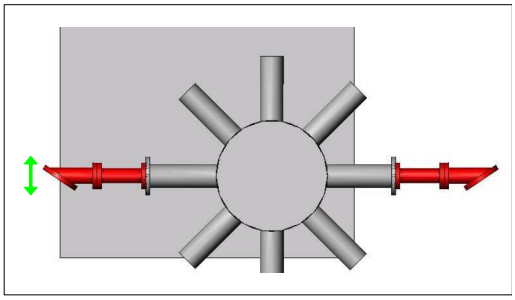

(a) Brewster windows

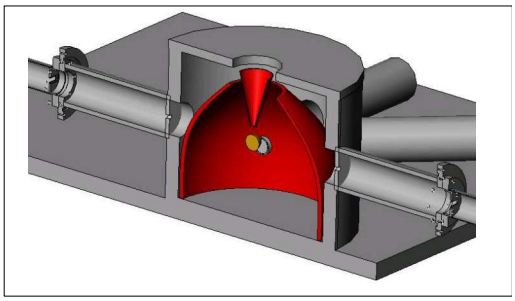

(b) Cones

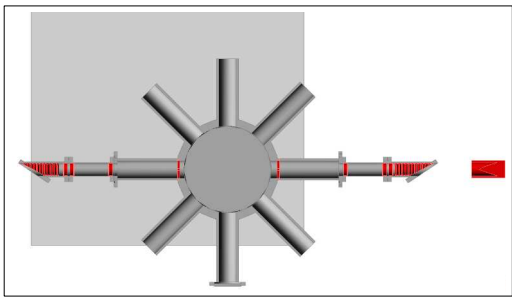

(c) Baffles

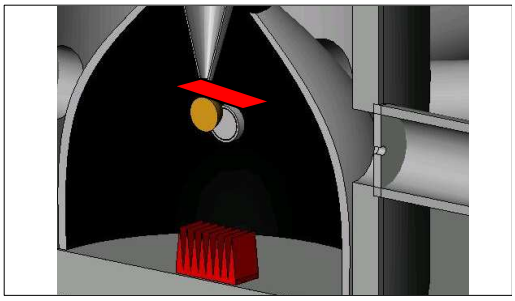

(d) Light trap and block

Figure 4.5: Diagram of the experimental apparatus to reduce stray light. Features to reduce stray light have been underlined in red, all features were simultaneously used during the Thomson scattering measurements.

of dust, both to avoid damage by the laser beam and to limit stray-light production.

The features described so far to reduce stray-light have been adapted from what has been described in previous experiments [2, 24, 25, 75]. However in an experiment involving laser produced plasmas, the main source of stray-light is coming from the scattering of the target itself. To counter this problem, a wedge was installed to cover the surface of the target from the viewing area. This is illustrated in figure 4.5(d). The wedge was set to cover no more than 1 mm of plasma from the target surface and in this configuration, the Thomson signal could be measured up to 2 mm from the target. Any closer, the stray-light was becoming too strong to make any good measurements. When the plasma was probed further away from the target surface, the stray-light was dropping significantly, as shown in figure 4.6.

The optical table and the chamber were covered with black material to minimise any stray light from the laboratory entering the spectrometer. The stray light signal, with only the probing laser on, was taken for every data and substracted from the total signal when analyses were done.

### 4.2.3 Collecting optics and Spectrometer

The scattering signal was imaged onto the entrance slit of the spectrometer using two 250 mm focal length achromatic doublet lenses (AL), of 40 mm diameter, as shown in figure 4.3 . The lenses were coated to limit reflection in the visible ($MgF_2$ coating). The signal was directed using three aluminum mirrors not represented in figure 4.3. In this configuration, the direction of the probing laser was aligned with the slit of the spectrometer, so that maximum signal was directed into the spectrometer, and the lateral expansion of the plasma was recorded onto the camera with a 1:1 ratio.

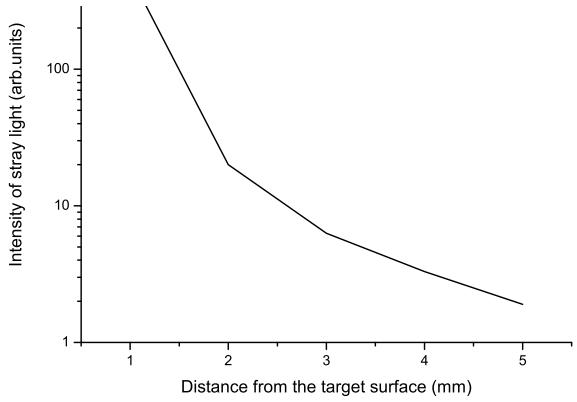


Figure 4.6: Intensity of the stray light evolution with distance from the target normal.

The spectrometer used was a SPEX 750mm monochrommator with two 1200l/mm gratings (G1 and G2), represented in figure 4.7. The spectrometer could be used with a single grating by rotating mirror M1, giving a dispersion of 1.15 nm/mm. When using the double grating the dispersion was 0.58 nm/mm. The instrument function and the calibration of the spectrometer were determined using a mercury lamp (doublet at 576.9 and 579.0 nm) and a neon lamp because it has three lines at 533.0 nm, 534.1 nm and 540.0 nm close to the wavelength region of interest. The adjustable slit at the entrance of the spectrometer was set to $100\mu m$ providing an instrument function of width $\sim 0.20nm$.

### 4.2.4 Detector

The detector used to capture the Thomson scattering spectra is an ICCD camera (Intensified Charged Coupled Device) from Oriel Instruments, model InstaSpec V. The camera had $27\mu m$ square pixels arranged in a $256 \times 1024$ 2-D array. This array was coupled to a gated image intensifier of 18 mm diameter.

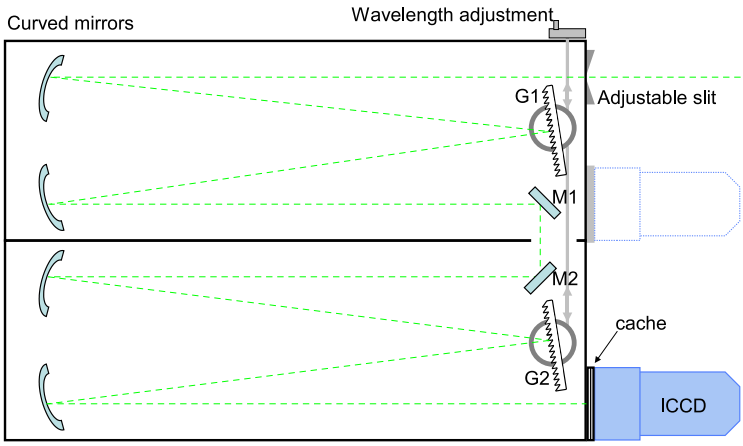


Figure 4.7: Double grating spectrometer layout.

This image intensifier, placed before the CCD chip serves two functions. The first is to amplify incoming light in order to detect very small signal. The second is to act as a very fast shutter (up to 5 ns gate times), as it can be rapidely switch on and off. The image intensifier consists of a photocathode, a microchannel plate (MCP) and an output phosphor screen. The image is focused onto the front window, and the photons hitting the photocathode emit electrons which then enter capillaries (or channels) of the MCP. A large potential difference (500 to 1000V) accelerates the electrons, and a cascade of secondary electrons is released as they collide with the channel walls. The original signal is amplified with gain up to $10^4$ [76]. The voltage across the channel plate can be varied in order to control the gain. On the InstaSpec V system, this is realised with a 10 positions switch on the detector head. In the present experiment, maximum gain was used.

The photocathode can also act as an optical shutter. A potential is applied to the photocathode, and when it is positive with respect to the entrance of the MCP, the electrons cannot leave the surface of the photocathode and the intensifier is switched off. As a result, an electric pulse applied

to the photocathode provides the gating of the ICCD.

The ICCD camera has a linear response to light exposure up to its charge saturation limit, which is the point at which it could no longer store any more charges. It had a dynamic range of 64 000 determinded by the 16-bit analogue-to-digital converter. In practice, the response is no longer linear above a maximum of approximately 32 000 counts.

A three-stage cooler allowed the ICCD head to be cooled to $2°C$, which minimised the noise due to the dark current from the random thermal motions of the electrons. The system software of the detector allowed the substraction of background images in order to correct for ambient room light and dark signal. The camera was triggered externally as described in section 4.2.6.

### 4.2.5 Alignment and calibration

In a Thomson scattering experiment on laser produced plasmas, precise alignment is essential to the success of the measurements. To facilitate this alignment, a geometry at right angle was chosen; this is represented on figure 4.8.

The nature of the expanding plasma requires precise alignment between

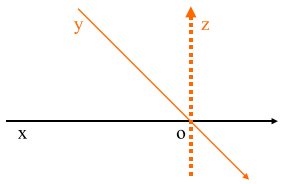


Figure 4.8: Geometry of the Thomson scattering experiment, x represent the ablating laser axis, y the probing laser axis and z the viewing direction.

the ablating laser beam (along x axis) and the probing laser beam (along y axis) to measure the spacial evolution of the plasma. The origin (o) was set at the center of the chamber and the tip of a $200\mu m$ wire could be positioned in and out of o to check and adjust the alignment. The target, perpendicular to x, could be moved along x to probe different part of the beam. A standard procedure was used to align both laser beams to the center of the chamber using cross wires at the entrance and exit ports of the chamber. However, once in place, the Brewster windows shifted the path of the probing laser beam. The probing laser direction had to be adjusted so it was going again through all the apertures along the laser path and the wire tip at the center of the chamber.

As mentioned before, the Thomson scattering cross-section is small compared to the other signals, making it difficult to detect. Geat care had to be taken to ensure that maximum scattering signal was reaching the spectrometer. For that, different procedures were used to achieve the best alignment possible.

A green He-Ne laser at 543.5 nm was passed through the spectrometer and directed toward the chamber using three aluminum mirrors (see section 4.2.3). The laser had to be adjusted to pass through the center of each mirror and grating, and to then hit the tip of the alignment wire at the center of the chamber (following the inverse path of the scattering signal). The two collecting lenses were then inserted so not to modify the path of the laser. This provided a first rough alignment of the spectrometer.

The green He-Ne laser was then shone directly onto the tip of the alignment wire. The scattered light from the tip could be followed and optimised first by eye on the slit of the spectrometer and then using the ICCD detector

by tuning the spectrometer to the correct wavelength.

To get a final fine adjustment, the chamber was filled with gas (usually Nitrogen or Argon was used) and the scattering of the YAG laser was recorded with the ICCD detector. This final stage was usually necessary to ensure that the scattering signal was parallel to the slit. Correction could be made using the collecting mirrors. An example of an optimised image from the scattering of a cold gas by the YAG laser is shown in figure 4.9.

The two last procedures had to be repeated everytime the target was changed, and the last procedure before every experimental run.

In the case of incoherent scattering ($\alpha \ll 1$), the scattered intensity is proportional to the electron density (see chapter 3). As a result, the intensity axis must be calibrated to determine the value of the electron temperature in the plasma, $n_e$. An easy and accurate way to calibrate the system is to observe the Rayleigh scattering light from a cold gas at relatively high pressure in place of the plasma. Using this method is useful to avoid absolute calibration of the laser output and the detecting system. In the case of this experiment, the chamber was regularly filled with $N_2$ or Ar for alignment purpose as described previously. It was found that the calibration from Ar gas was easier to use. Molecular Raman scattering features could be ob-

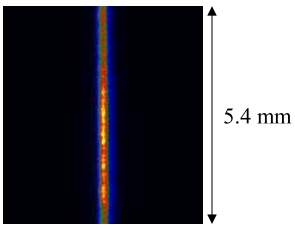


Figure 4.9: Scattering from 20mbar of $N_2$ gas. The image is showing 5.4 mm of the lateral extension of the plasma.

served from the $N_2$ gas, making it harder to estimate the intensity of the Rayleigh scattering signal at the wings.

Once the Rayleigh scattering from a cold gas and the Thomson scattering spectra are obtained, the electron density is given by (see section 3.4.2):

$$n_e = n_g \frac{\sigma_{Ray}}{\sigma_{Th}} \frac{A_{Th}}{A_{Ray}} \tag{4.1}$$

Sneep *et al*, in ref. [68] measured a value for the Rayleigh scattering of Ar gas at 532 nm of $(4.45 \pm 0.3) \times 10^{-27} cm^2$. This value was used to interpret the data in the present work.

The main issue with this calibration method can be the presence of dust particles in the chamber. The scattering from micrometer-sized dust particles being enormous, it can lead to an overestimate of the Rayleigh scattering, and as a result, an underestimate of $n_e$. During this experiment, the gas was left in the chamber overnight to give time to dust particles to settle.

### 4.2.6 Synchronisation

The experiment was synchronised using three Standford DG-535 delay generators (trigger box). The first delay generator (trigger box 1) constituted the master trigger box, it generated a reference pulse $T_0$ at 10 Hz. This pulse was used to trigger the flashlamp of the YAG laser, and the two other trigger boxes. The different trigger pulses used for the lasers and illustrated in figure 4.10(b) were set according to the manufacturer's guidelines [77, 78]. The delay between the flash lamp and the Q-switch was optimised and best output energy of the YAG laser was found for a delay of $229 \mu s$. The timing

of the system: ablation of target, probing and detection, was done using a photodiode. The jitter of the probe with respect to the ablating laser was found to be $< 15ns$. The gate of the ICCD was optimised to collect light only during the length of the probe laser pulse. The minimum gate to collect all the scattering signal was found at 24ns on the trigger box (effective optical gate of $\sim 10ns$ [76]) with a delay of $229\mu s + 258ns$. The initial time of plasma formation was found with an accuracy of 10ns by looking at the self emission of the plasma. A summary illustrating the timing set-up with the delays of each instrument is shown in figure 4.10.

To investigate the plasma at different times, only the trigger pulse controlling the KrF laser was shiffted in time. The master trigger box was run on burst mode. This meant that the lasers were triggered at 10Hz in bursts of 100 to 500 shots. Regarding the ICCD detector, the gate mode was set to "gate AND fire" (Gate mode switch to position 1). In this way, any trigger on the controller card of the detector was ignored until it had been armed. The ICCD was set to external trigger, single shot, and the exposure time

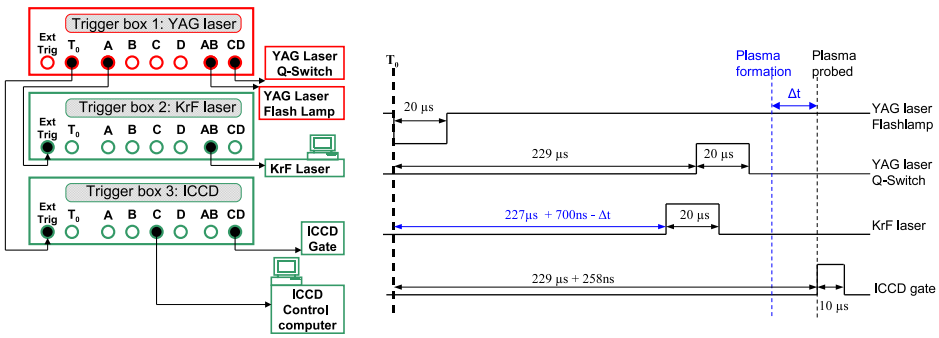


(a) Trigger box set-up (b) Timing diagram

Figure 4.10: Diagram showing the set-up used to synchronise the ablating laser system, the probing laser system and the detection system. $\Delta t$ is the delay between the plasma formation and the probing, $T_0$ is the reference time of the master trigger box.

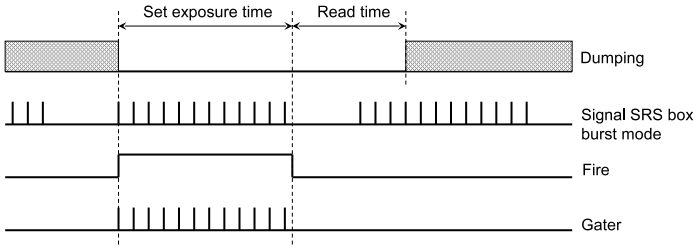


Figure 4.11: Timing diagram illustrating the integration of many shots on the CCD chip when set to gate AND fire mode. The exposure time was set to accumulate the number of shots in one burst. A delay, not represented in this diagram was induced in the SRS boxes, or between the controller card external trigger and the Fire out.

adjusted to accumulate the number of shots in one burst. ANDing the fire and gate signals prevented extra signal beeing accumulated on the CCD during readout, as shown in figure 4.11.

## 4.3 Summary

In this chapter, the important features of the experimental set-up used during this work have been discussed. An overview of the ablation system was given. This was followed by a detailed description of the systems developed to collect the scattering signal, with particular emphasis on the techniques used to optimise the signal and reduce the stray light as much as possible.

In the next chapter, experimental results obtained using the Thomson scattering diagnostic set-up developed at Queen's University will be presented and discussed.

# Chapter 5

# Optical scattering from $Mg$ plumes

*"If the entire population of the world were to spend their working day doing nothing else, it would take them fifty years to count a thimble full of atoms"*

Ernest Rutherford

Once the experimental challenges had been overcome, spectra were obtained by Thomson scattering, unquestionably providing a quicker way of counting electrons than the one suggested by Rutherford. The electron density and temperature of an expanding magnesium laser produced plasma were deduced. This chapter will present how.

First scattering measurements were made using a titanium target as it has been widely studied before under similar ablation conditions [9, 11, 12, 13, 79, 80] and the diagnostic techniques could then be compared or complemented. However, the spectrum from titanium has a large number

of transitions that compromised any scattering measurements. Magnesium was then chosen as the target material because its spectrum has few strong transitions, and in particular none around 532 nm, wavelength region of the probing beam. Magnesium plasmas have also been studied experimentally with other diagnostics [9, 10, 22, 81] as well as theoretically with simulation of the emission spectra [52] and simulation of the ablation of targets using hydrodynamic codes [82, 83].

The sequence of this chapter is as follows. We will first discuss the data acquisition methods and the procedure to extract the Thomson scatter data from a spectrum. The features observed along with the Thomson scatter signal are clarified, and their possible use in identifying the presence of particular excited states is considered. The effect of the plume heating by the probing laser is then examined, especially when the plasma is denser and the heating can be significant. And finally, the evolution of the plume is looked at in detail with the Thomson scatter diagnostic developed in the present thesis.

## 5.1 Data collection

The Thomson scatter cross section being small (see section 3.3.1), great care had to be taken in collecting the scattering data, and several measurements were carried out to complement the actual scattered spectrum.

Every day, without breaking the vacuum in the target chamber, the alignment of the system was checked as follows:

- Probing laser with respect to the spectrometer: by filling the chamber with gas, and if required optimising the signal, as described in section 4.2.5.

- Probing laser with respect to the plasma (or in practice, with respect to the ablating laser): this could be done visually by bringing the target tangent to the probing laser beam and checking if the track left by the ablating laser beam was aligned with the probing beam. Several back reflections along the path of both laser beams were marked in the far field to monitor any displacement of the beams.

Scattered signal of similar plasma conditions were compared from one day to another. No major changes were observed, as shown in figure 5.15, in the later section discussing uncertainties (section 5.4.1).

Each data required to take four spectra in order to extract the Thomson scatter signal:

- Background: Lasers off, this was the background room light and the electron noise in the detector. The background thermal noise could be reduced by cooling the camera to 2 degrees, and was then subtracted automatically by the software of the camera.
- Emission: This is the self emission of the plasma only: ablating laser on, probing laser off.
- Stray light: This is the light coming from various reflections, in the experimental room and the vacuum chamber, of the probing laser light when there is no plasma: ablating laser off, probing laser on.
- Scattering: This is the raw scattered spectra of the probing laser light from the plasma: both lasers on, aligned and synchronised.

Lasers on and off, does not necessarily mean that they were actually turned off, which would compromise the stability of the lasers, but that they were blocked in such a way that they were not affecting the signal

taken.

In the case of a laser-produced plasma experiment, it is not possible to measure the Rayleigh scattering from neutral species independently, the way it is done in gas discharge experiments [84]. The way the contribution of the Rayleigh signal was taken into account to extract information from the Thomson scatter signal will be discussed below 5.2.1.

A slice of the plume was probed at a time, at a predetermined distance $d$ from the target surface ranging from $d = 2mm$ to $d = 5mm$ away from the target surface. For each position, the time delay $\Delta t$ between the two laser pulses was varied from $\Delta t = 100ns$ to $\Delta t = 1\mu s$, the time zero being the initial plasma formation. This gives a broad image of the spatial and temporal evolution of the plasma. For each position in space $d$, three images were taken: Emission corrected (E), Stray Light corrected (SL) and Scattering corrected (Scat). The correction here accounts for the background, automatically subtracted by the software of the camera when recorded prior to any measurement. For each time delay $\Delta t$, only signal E and signal Scat were recorded, as the stray light was not changing.

Each individual image recorded is an accumulation of a certain number of laser shots, which is determined by the ICCD exposure time (see section 4.2.6). The number of shots per image was set so not to saturate the ICCD camera (i.e. no pixel with more than 32000 counts) and varied depending on the intensity of the signal detected. Several images of the same time and position were recorded and then summed. Typical example of the three images measured for one scattering spectrum are shown in figures 5.1 and 5.2. The spectra were taken $2mm$ from the target surface, with a delay of $200ns$ for figure 5.1 and at later time, with a delay of $600ns$ for figure

figure 5.2. The ablating laser energy was $\sim 280mJ$, for images (a) and (b) of each figure. The probing laser energy was measured to be $\sim 400mJ$. In figures 5.1 and 5.2 the probing laser-beam travels from bottom to top. It should be noted that the color-scales differ from one image to another in order to make the observed signal perceptible. The signal sometimes has to be presented with the brightest data out of the color-scale since the signal that presents the most interest in this study, the Thomson scattering signal, is weak compared to the strong central peak at $532nm$ which superimpose stray light and Rayleigh scattering signals. However, the signal was never saturated. The exposure time for the present images was set to 10 seconds, recording 100 shots at a time, 5 different images were added together in images 5.1(a) and 5.2(a), and 2 in image 5.1(c). For images 5.2(b) and 5.2(c), the signal was not as strong so it was possible to change the exposure time to 50 seconds and accumulate 500 laser shots in one acquisition. To facilitate the comparison between each data set in figure 5.1 and 5.2, the images have been normalised to 1 shot.

From the first raw scattering images in figures 5.1(a) and 5.2(a), a contribution of several signals can clearly by seen. The bright Rayleigh signal at the central wavelength is sitting on a broad weaker Thomson signal, as expected. Some interesting satellite features are also present. These features have been identified as atomic Raman transitions and will be discussed in more detail in section 5.3.

Magnesium was chosen as a target material because there was no strong emission line around 532 nm according to the National Institute of Science and Technology data base [56]. Figure 5.1(b), and figure 5.2(b) confirms experimentally that there is no significant emission in the wavelength region of interest (528 - 536 nm). The continuum emission still present at $200ns$

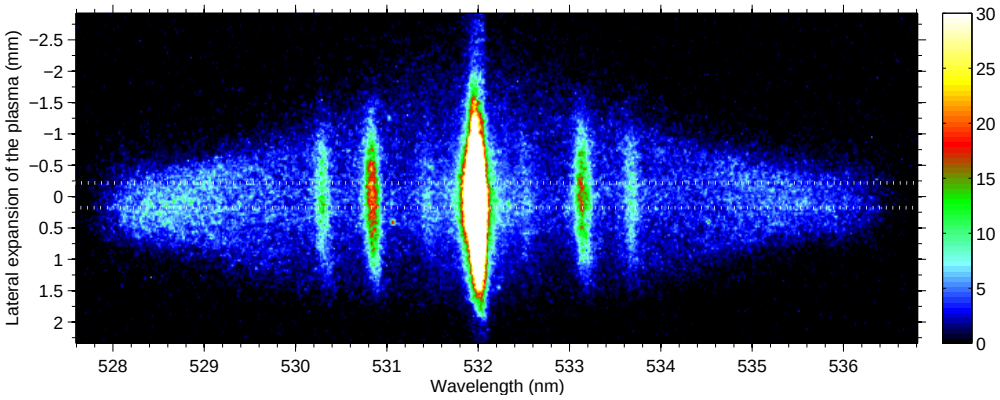


(a) $d = 2mm$ ; $\Delta t = 200ns$ ; Scattering spectrum

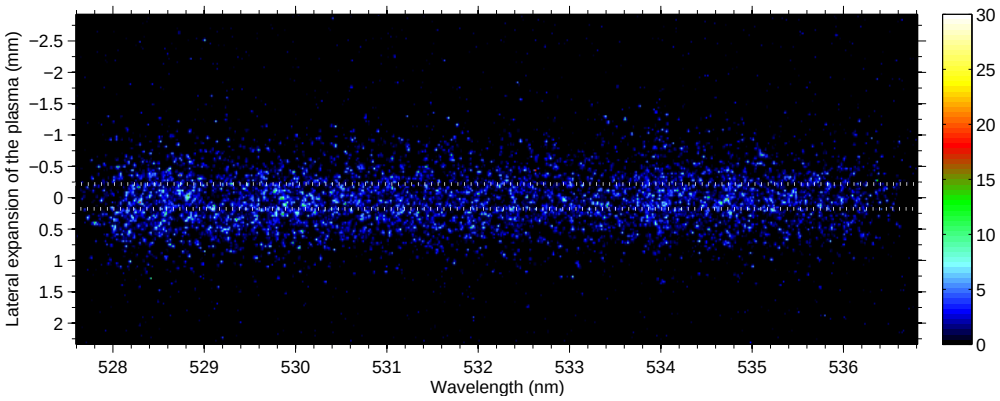


(b) $d = 2mm$ ; $\Delta t = 200ns$ ; Self emission

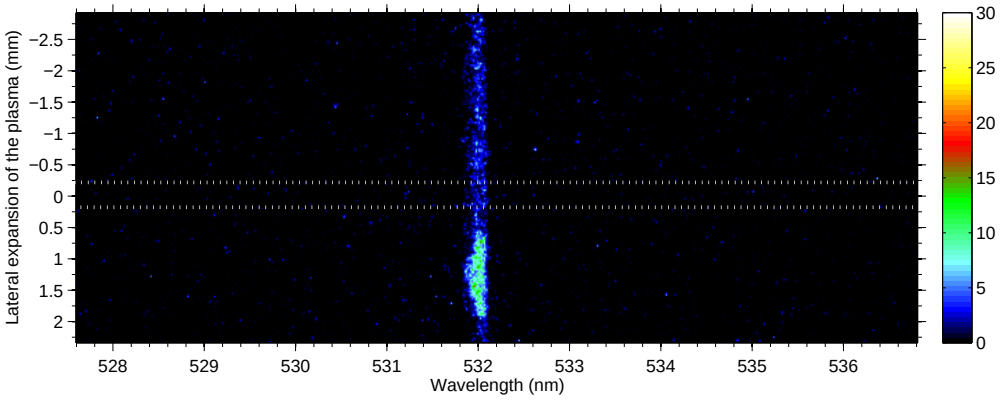


(c) $d = 2mm$ ; $\Delta t = 200ns$ ; Stray light

Figure 5.1: Set of images recorded to obtain a scattering spectrum from a Mg laser plasma, $2mm$ from the target surface, $200ns$ delay. The three images are background corrected and normalised to 1 shot. The white lines indicate the center part of the plasma binned for the analyses following in this chapter. The colour bar refers to the number of counts of the camera, image (a) is purposely out of scale for the center peak at 532 nm to show the rest of the signal, but is not saturating (maximum $<$ 32000 counts).

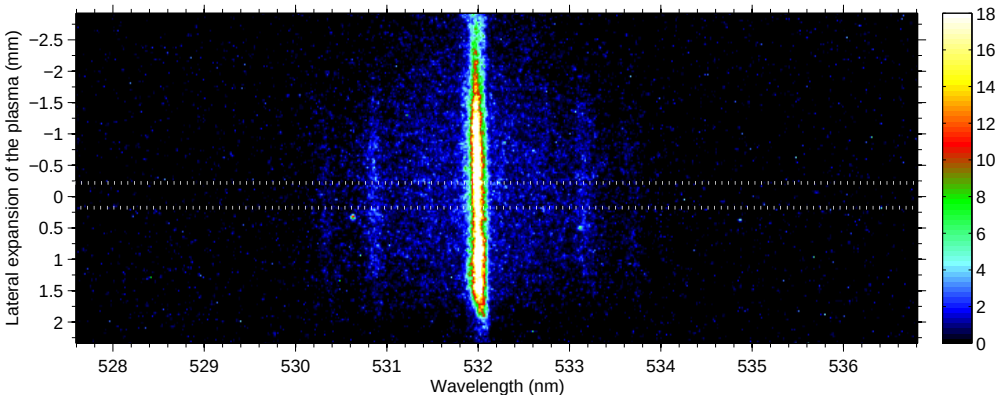


(a) $d = 2mm$ ; $\Delta t = 600ns$ ; Scattering spectrum

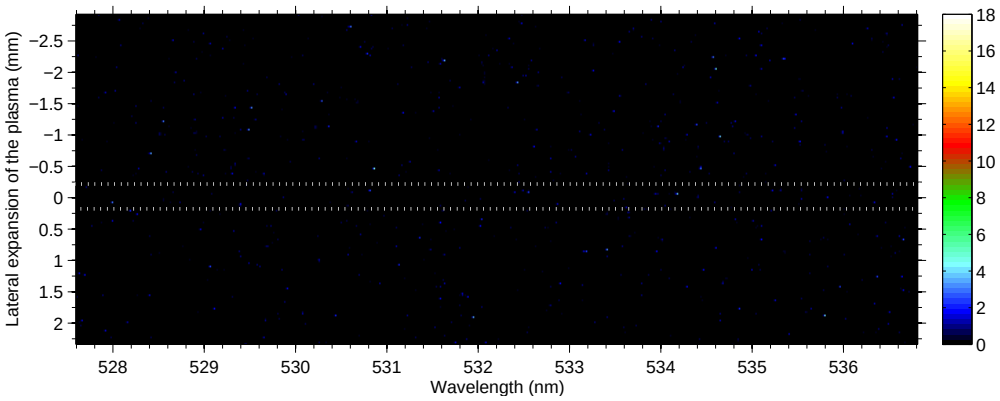


(b) $d = 2mm$ ; $\Delta t = 600ns$ ; Self emission

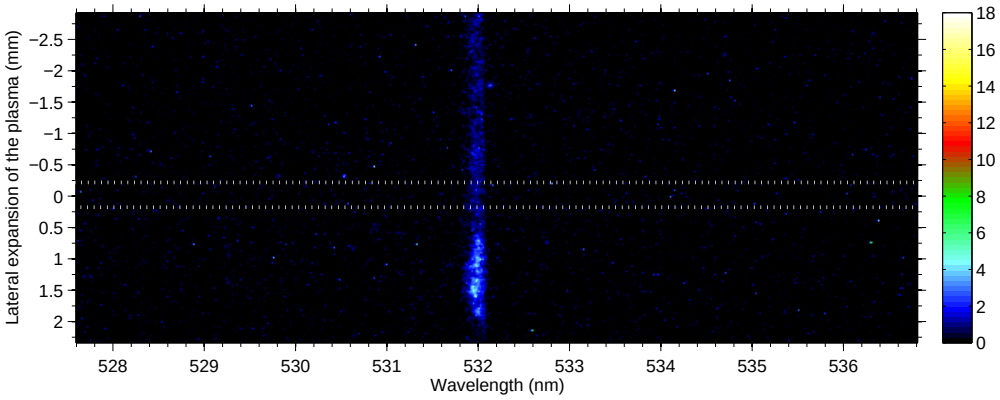


(c) $d = 2mm$ ; $\Delta t = 600ns$ ; Stray light

Figure 5.2: Set of images recorded to obtain a scattering spectrum from a Mg laser plasma, $2mm$ from the target surface, $600ns$ delay. The three images are background corrected. The three images (a), (b) and (c) are an accumulation of 500 shots, normalised to 1 shot. The rest is similar to figure 5.1.

disappears rapidly. For the case $2mm$ away from the target plane and $200ns$ delay (shown in figure 5.1), the self emission represents less than half the raw scatter signal (as shown in figure 5.3), and once subtracted, the corrected scatter signal is still significant (as shown in figure 5.5).

The stray light signals shown in figure 5.1(c) and 5.2(c) were taken at the beginning, and at the end of an experimental run, respectively. During this run, the target was kept fixed, and only the delay between the two lasers was varied. As a result, the stray light is not expected to change. Experimentally, the difference between the two signals is $< 10\%$. A brighter point of stray light can be seen on the two figures, due to the scattering from the edge of the target. It does not affect the data analysis following in this chapter, since it is not in the region of plasma studied (center part of the plasma, between the two white lines on figures 5.1 and 5.2 ). In general, the stray light signal is much weaker than the scattering signal, and does not represent a problem to the analysis of the data since it can be subtracted easily. In the case of figure 5.1, the scattering signal at the central wavelength of 532 nm is more than 100 times stronger than the stray light (see figure 5.3(a)), and in the case of figure 5.2, it is still 10 times stronger.

## 5.2 Signal processing

The 3D spectra were full vertically binned to be analysed. The central part of the plasma was first studied. For that, the sum of 15 rows of data (corresponding to 0.4 mm of plasma) was plotted against the wavelength shift, as shown on figure 5.3. The lateral expansion of the plasma was analysed by summing 5 rows of pixels at a time on the same image, which corresponded to steps of $0.13mm$, as illustrated in figure 5.22(a).

To extract the scattering only signal from the raw scattering data, the

stray light signal and the emission signal were subtracted living a corrected scattering spectra. However, this correction still leaves a scattering signal composed of the Rayleigh scattering, the Thomson scattering, and the Raman features. The three signals had then to be added in the fitting procedures to encounter for the contribution of each scattering process in the total scattering signal. Depending on the shape of the spectrum, two methods were used to fit the scattering signals and extract information on the electron density and temperature from the Thomson signal. To illustrate the methods used to obtain the electron density and temperature from the plasma, spectra from the same data set as in figure 5.1 and figure 5.2 are used in the following section. That is experimental spectra recorded when probing the plasma $2mm$ from the target surface, with different time delays, with a probing laser energy of $\sim 400mJ$ and an ablating laser energy of $\sim 280mJ$. Depending on the intensity of the scatter signal, spectra were taken with accumulation from 500 shots to 2000 shots. All following spectra presented in this analysis are normalised to 1 shot so they can be compared one to another.

### 5.2.1 Analysis of late time spectra

In figure 5.3(c) and 5.3(d), the spectrum from scattering of Mg plasma at late time shows a broad Thomson scatter feature exhibiting a Gaussian profile. As discussed in section 3.4, if we assume that the electron energy distribution function is Maxwellian, the Thomson scattering spectrum can be fitted with a Gaussian. The value of the electron temperature can be calculated from the width of the scatter signal, as given by equation 5.2. The electron density can be calculated from the intensity of the scatter signal. For that, the intensity axis was calibrated using the Rayleigh scattering of a cold gas of known density, as described in sections 4.2.5.

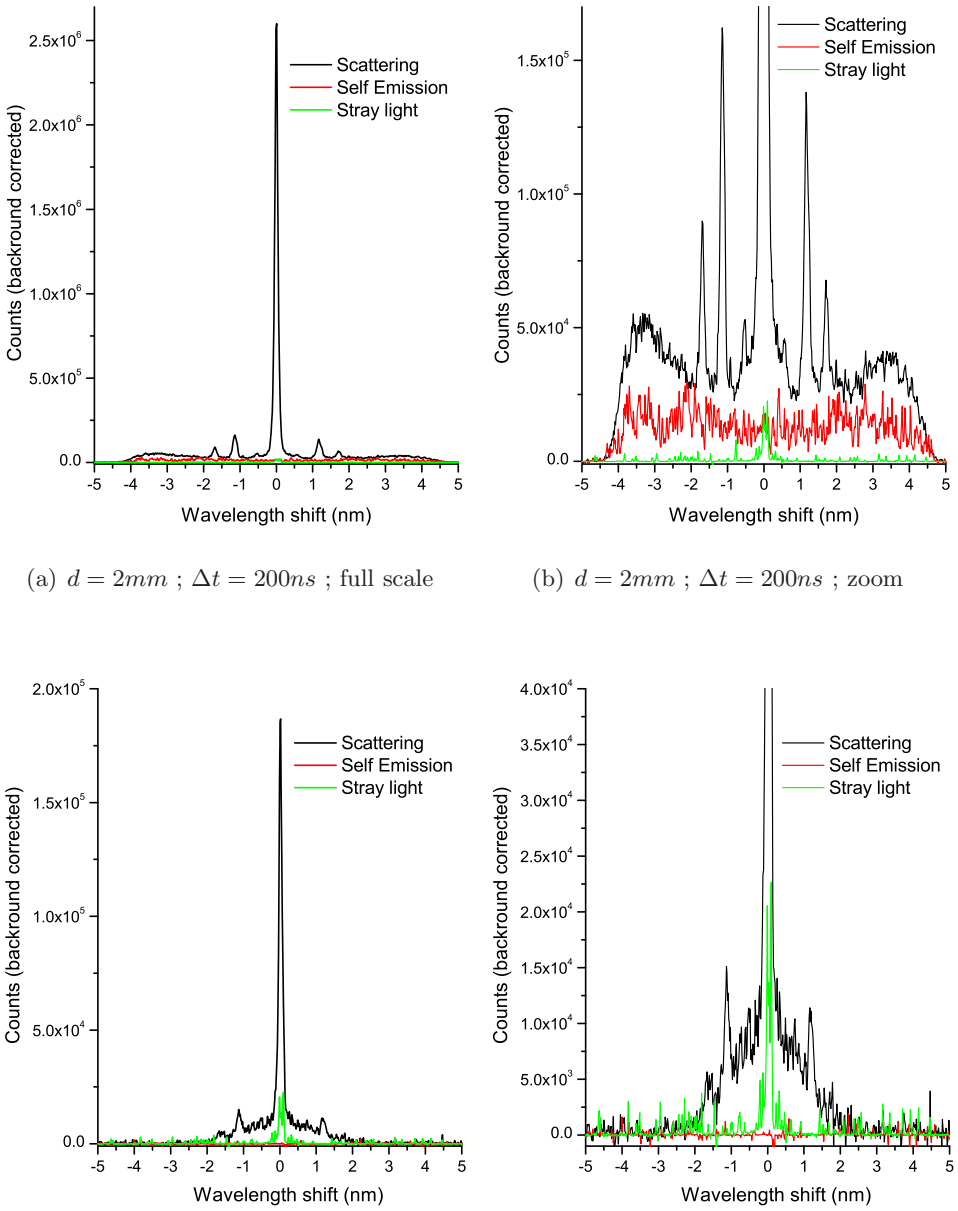


(a) $d = 2mm$ ; $\Delta t = 200ns$ ; full scale

(b) $d = 2mm$ ; $\Delta t = 200ns$ ; zoom

(c) $d = 2mm$ ; $\Delta t = 600ns$ ; full scale

(d) $d = 2mm$ ; $\Delta t = 600ns$ ; zoom

Figure 5.3: Typical set of measurements, result of the binning of the images in figure 5.1 and 5.2, obtained 2 mm away from the target surface, at early time (a) and (b), and late time (c) and (d). Each data set is the result from the accumulation of images corresponding to 500 laser shots.

A Rayleigh scattering spectrum from Ar gas is shown in figure 5.4. The spectrum was taken with a probing laser intensity of $\sim 400mJ$. It results of the accumulation of 800 shots, and is the sum of 15 rows of the image spectrum, normalised to 1 shot. The stray light from the probing laser passing the chamber with no gas, the ambient room light and the noise of the camera were subtracted from the raw data to produce the spectrum shown in figure 5.4. Both integration method (fig. 5.4(b)) and fitting method (fig. 5.4(a)) were compared to calculate the area under the curve. The result in the value of the electron density differed by less than 1% so the fitting method was privileged as it does not require to fix an interval of integration. It was found that a Voigt profile, convolution of a Gaussian profile with a Lorentzian profile, was best fitting the Rayleigh signal.[1] The gauge used to measure the pressure in the chamber was calibrated by the manufacturer to insert Argon gas. According to the conversion curves provided [86], the chamber was filled with 10 mbar of Argon gas (4mbar read on the gauge). A systematic error of 1 mbar was assumed. Using the equation of a perfect gas, the density of Argon gas in the chamber was estimated to $n_g = (2.4 \pm 0.2) \times 10^{17} cm^{-3}$.

The plasma scatter spectra were then analysed to extract information on the underlying Thomson signal: half width of the signal, $x_{HWHM}$ and area under the signal, $A_{Th}$. For that, the contribution from the three types of scattering were fitted with a Voigt profile for the Rayleigh scattering and Gaussian profiles for the Raman features and the Thomson scatter, as shown in figure 5.5. As discussed in chapter 3.4, the value of the electron density and electron temperature of the plasma for a given time and a given plasma volume is given by the following expressions, reviewed here for the reader's

[1] Fitting of the data was performed with the Levenburg Marquardt algorithm, using the open source program *Fityk* [85].

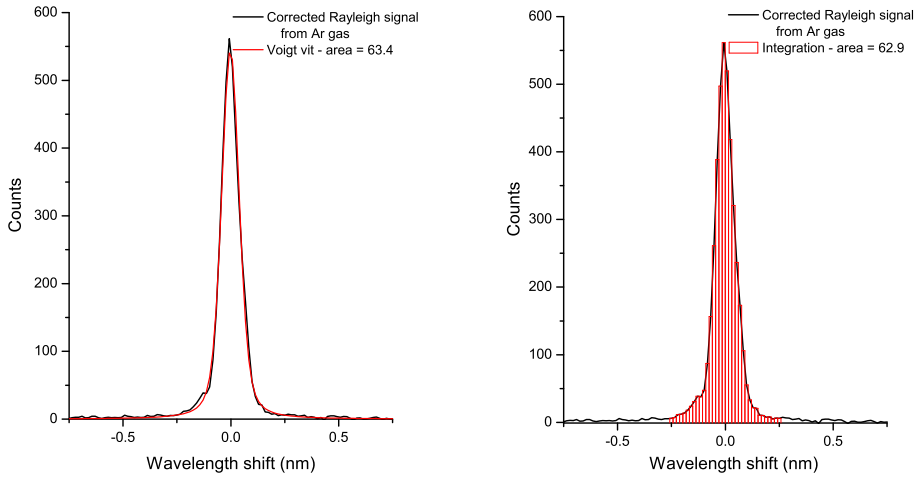


(a) Voigt fit (b) Integration method

Figure 5.4: Rayleigh scattering spectrum of argon gas, obtained with a probing laser of $\sim 50 J/cm^2$.

convenience:

For the electron density in $cm^{-3}$:

$$n_e = n_g \frac{\sigma_{Ray}}{\sigma_{Th}} \frac{A_{Th}}{A_{Ray}} \tag{5.1}$$

where in the case of Ar gas and in the present data set,

$n_g = (2.4 \pm 0.2) \times 10^{17} cm^{-3}$

$\sigma_{Ray} = (4.45 \pm 0.3) \times 10^{-27} cm^2$ [68]

$\sigma_{Th} = (6.65 \pm 0.003) \times 10^{-25} cm^2$ [2]

$A_{Th}$ and $A_{Ray}$ are given when fitting a profile to the data as described previously.

For the electron temperature in eV:

$$kT_e = \frac{m_e c^2}{2ln2} \left( \frac{x_{HWHM}}{2\lambda_i sin(\theta/2)} \right)^2 \tag{5.2}$$

where in the case of the present experiment,

$\lambda_i = 532nm$

$\theta = \frac{\pi}{2}$

$x_{HWHM}$ is given when fitting a Gaussian profile to the data as described previously.

The results from the fitting of the data shown on figure 5.5(a), at 500 ns delay is giving an electron density $n_e(\Delta t = 500ns) = (1.6 \pm 0.2) \times 10^{15} cm^{-3}$ and an electron temperature $T_e(\Delta t = 500ns) = 0.65 \pm 0.17eV$. For figure 5.5(c), at 700 ns $n_e(\Delta t = 700ns) = (3.1 \pm 0.4) \times 10^{14} cm^{-3}$ and $T_e(\Delta t = 700ns) = 0.48 \pm 0.16eV$. A full study of the plume expansion using density and temperature calculated by Thomson scattering is presented in section 5.5.

### 5.2.2 Analysis of early time spectra

For the results earlier in time, shown in figure 5.3(a) and 5.3(b), it can clearly be seen that a Gaussian could not be fitted to the Thomson spectrum, and electron features are evident in the data. In this case, the electron temperature and density of the plasma were measured by fitting calculated spectra using the Salpeter approximation (see section 3.3.2). At $200ns$, the electron features are still spectrally separated from the Raman and Raleigh signals, but it is critical to consider the Raman and Rayleigh features in the analysis as they overlap the electron features in the data taken later in time, as can be seen on figure 5.6(f) . As a result, the Rayleigh scattering signal and the Raman features, fitted with Gaussian profiles were added to the fitting procedure. A Gaussian profile was chosen in that case to fit the Rayleigh signal, as it was easier to implement in the fitting routine, limiting the number of parameters. However, the complexity of the corrected overall scatter signal, the large intensity of the Rayleigh and Raman features compared to the Thomson signal, and the non negligible noise in the spectra made it hard for the fitting procedure to converge to a solution where the underlying

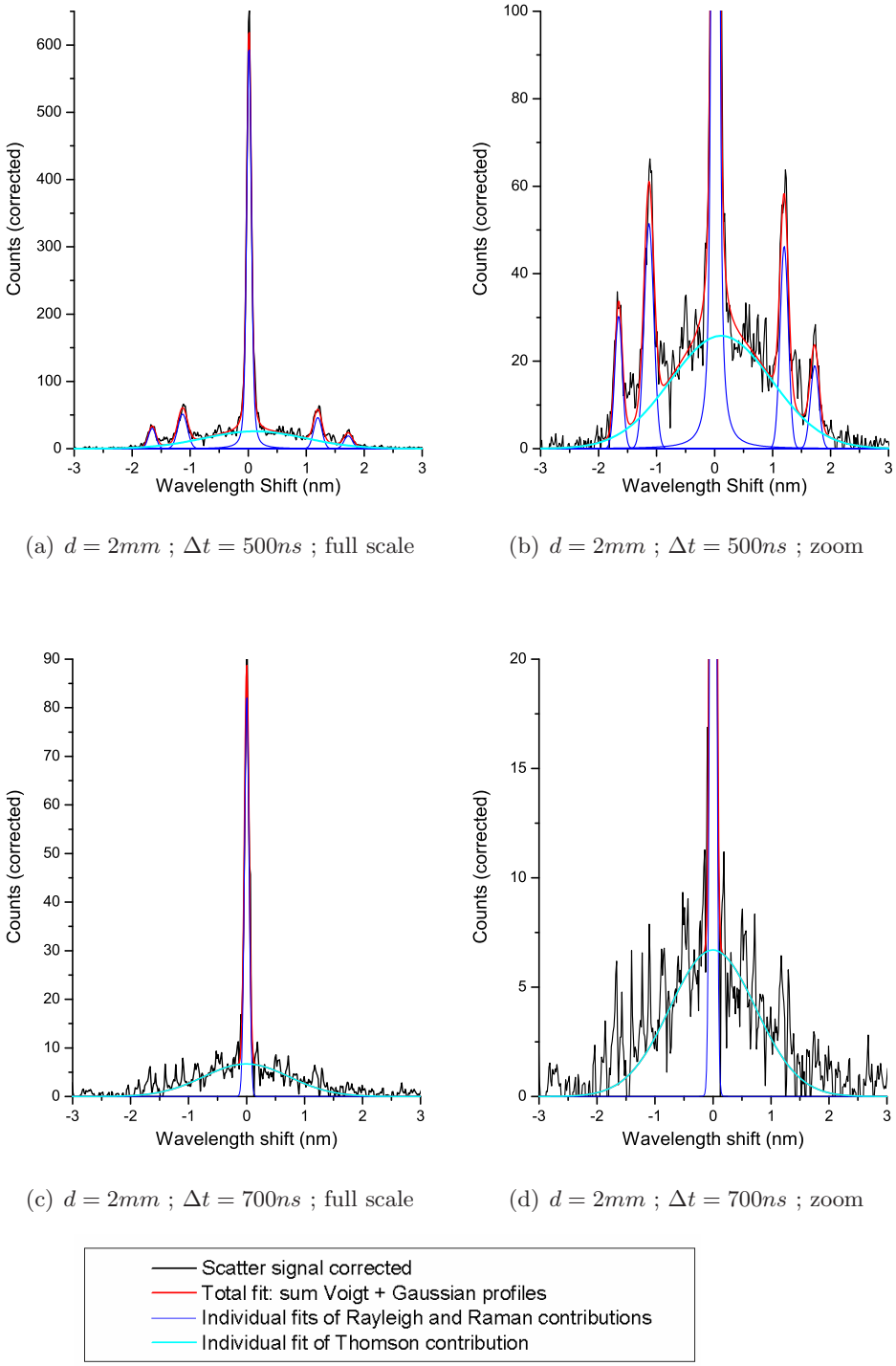


(a) $d = 2mm$ ; $\Delta t = 500ns$ ; full scale

(b) $d = 2mm$ ; $\Delta t = 500ns$ ; zoom

(c) $d = 2mm$ ; $\Delta t = 700ns$ ; full scale

(d) $d = 2mm$ ; $\Delta t = 700ns$ ; zoom

Figure 5.5: Example of late time scatter spectra fitted with the sum of a Voigt profile for the Rayleigh signal and Gaussian profiles for the Raman features (when still present) and the Thomson signal, using Fityk [85]. The scatter signal has been corrected for stray light and self emission.

Thomson signal was properly fitted. It was found that an approximate value of the electron temperature and density had to be input as starting values for the fitting procedure, to obtain a better fit of the Thomson signal. These first values were determined by considering only the underlying Thomson spectra and the theoretical Thomson spectra. The best fit of the Thomson signal was then found by trial and error. The results of these fits are shown in figure 5.6 and figure 5.7. The latter figure shows as well the result of the fit for spectra taken with delays $\Delta t > 400ns$, when the Thomson signal has a Gaussian shape. In this case, the electron density and temperature were determined using the calibration of Argon gas, as described in the previous subsection, and the values were used to plot theoretical curves. Figure 5.7 (c)-(f), shows that the theoretical curve fits the experimental data with the calculated density and temperature. This validates the first method using a calibration of the intensity axis.

In the scatter spectra at early time, presented in figure 5.6(d), we note an obvious asymmetry between the two electron features. This effect has been observed before on the ion feature [64] and is usually explained by a relative drift between electrons and ions which is driven by electron heat flow [2]. It is not clear at present whether we should observe such a drift in our experiment where the plasma only reaches modest temperature ($< 2eV$). This asymmetry is more likely to be due to spatial gradients in the probed plasma. As shown in figure 5.6(d), the positive and the negative part of the spectrum were fitted independently. In the case of the positive part of the spectrum, the fitting resulted in $n_e = 9.5 \times 10^{16} cm^{-3}$ and $T_e = 1.7eV$, the best fit of the negative part of the spectra was found for $n_e = 8 \times 10^{16} cm^{-3}$ and $T_e = 1.25eV$. The values of the electron density and temperature for the volume of plasma probed $2mm$ away from the target surface and with $200ns$ delay were then estimated as the average from both fittings with an

associated standard deviation error.

Table 5.1: Electron densities and temperatures for a Mg plasma, $2mm$ from the target surface and at different time delays, determined from the data in figure 5.6 and 5.7.

| Delay $\Delta t$ (ns) | Electron density $n_e$ $(cm^{-3})$ | Electron temperature $T_e$ $(eV)$ | Figure |
|---|---|---|---|
| 100 | $n_e = (5 \pm 1) \times 10^{16}$ | $T_e = 3 \pm 1$ | 5.6(b) |
| 200 | $n_e = (8.8 \pm 0.8) \times 10^{16}$ | $T_e = 1.5 \pm 0.3$ | 5.6(d) |
| 300 | $n_e = (2.5 \pm 1) \times 10^{16}$ | $T_e = 1.2 \pm 0.3$ | 5.6(f) |
| 400 | $n_e = (8 \pm 3) \times 10^{15}$ | $T_e = 0.9 \pm 0.1$ | 5.7(b) |
| 600 | $n_e = (9 \pm 1) \times 10^{14}$ | $T_e = 0.5 \pm 0.02$ | 5.7(d) |
| 800 | $n_e = (1.1 \pm 0.3) \times 10^{14}$ | $T_e = 0.4 \pm 0.1$ | 5.7(f) |

The electron densities and temperatures resulting from the fittings of spectra presented in figure 5.6 and 5.7 are summarised in table 5.1. A full study of the spatio-temporal evolution of the plume is presented in section 5.5.

## 5.3 The Raman features

In this section, we will discuss the satellites which are symmetric about the Rayleigh peak, present in the scatter spectra. Traditionally, when it comes to analysing spectra in atomic spectroscopy, it is wavenumbers that are commonly used, in units of $(cm^{-1})$, number of waves in $1cm$. Figure 5.8 shows a scatter spectrum represented in terms of shift in wavenumber from the central Rayleigh peak, taken from scattering of the plasma 2 mm from the target surface and with 200 ns delay.

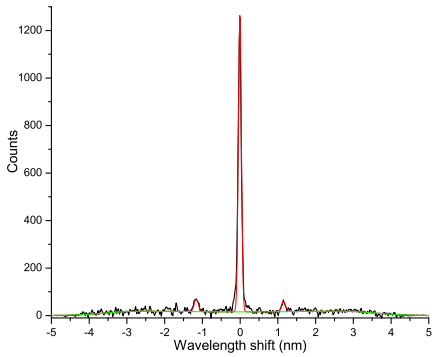


(a) $d = 2mm$ ; $\Delta t = 100ns$ ; full scale

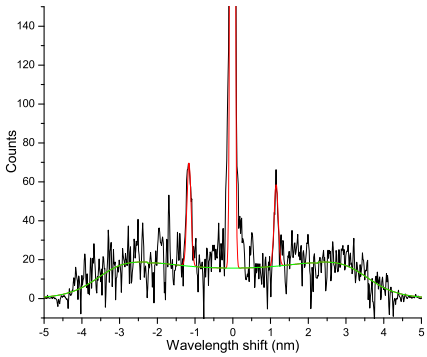


(b) $d = 2mm$ ; $\Delta t = 100ns$ ; zoom

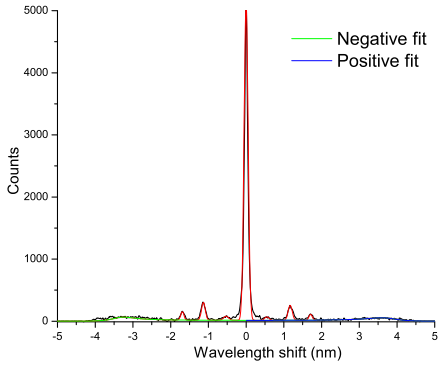


(c) $d = 2mm$ ; $\Delta t = 200ns$ ; full scale

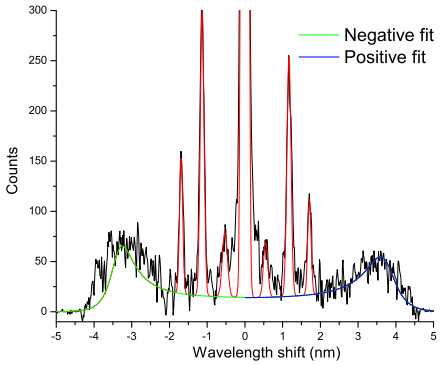


(d) $d = 2mm$ ; $\Delta t = 200ns$ ; zoom

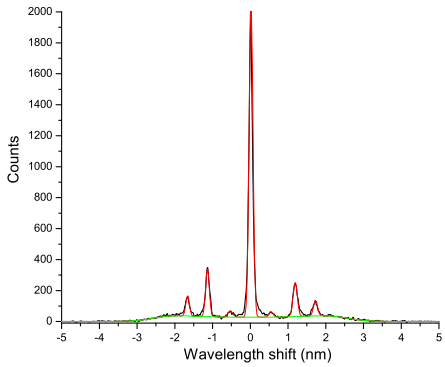


(e) $d = 2mm$ ; $\Delta t = 300ns$ ; full scale

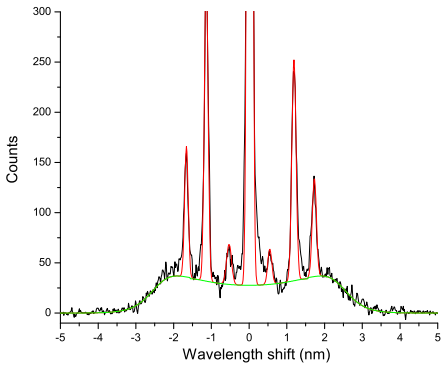


(f) $d = 2mm$ ; $\Delta t = 300ns$ ; zoom

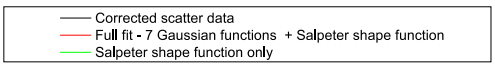


Figure 5.6: Corrected scatter spectra fitted with Gaussians for the Raman and Rayleigh features, and using the Salpeter approximation for the Thomson signal. These spectra were obtained $2mm$ from the target surface and at different time delays, $100ns$ (a) - (b), $200ns$ (c) - (d), and $300ns$ (e) - (f). Each data set results from the accumulation of several laser shots, normalised to 1 shot and corrected for stray light and self emission.

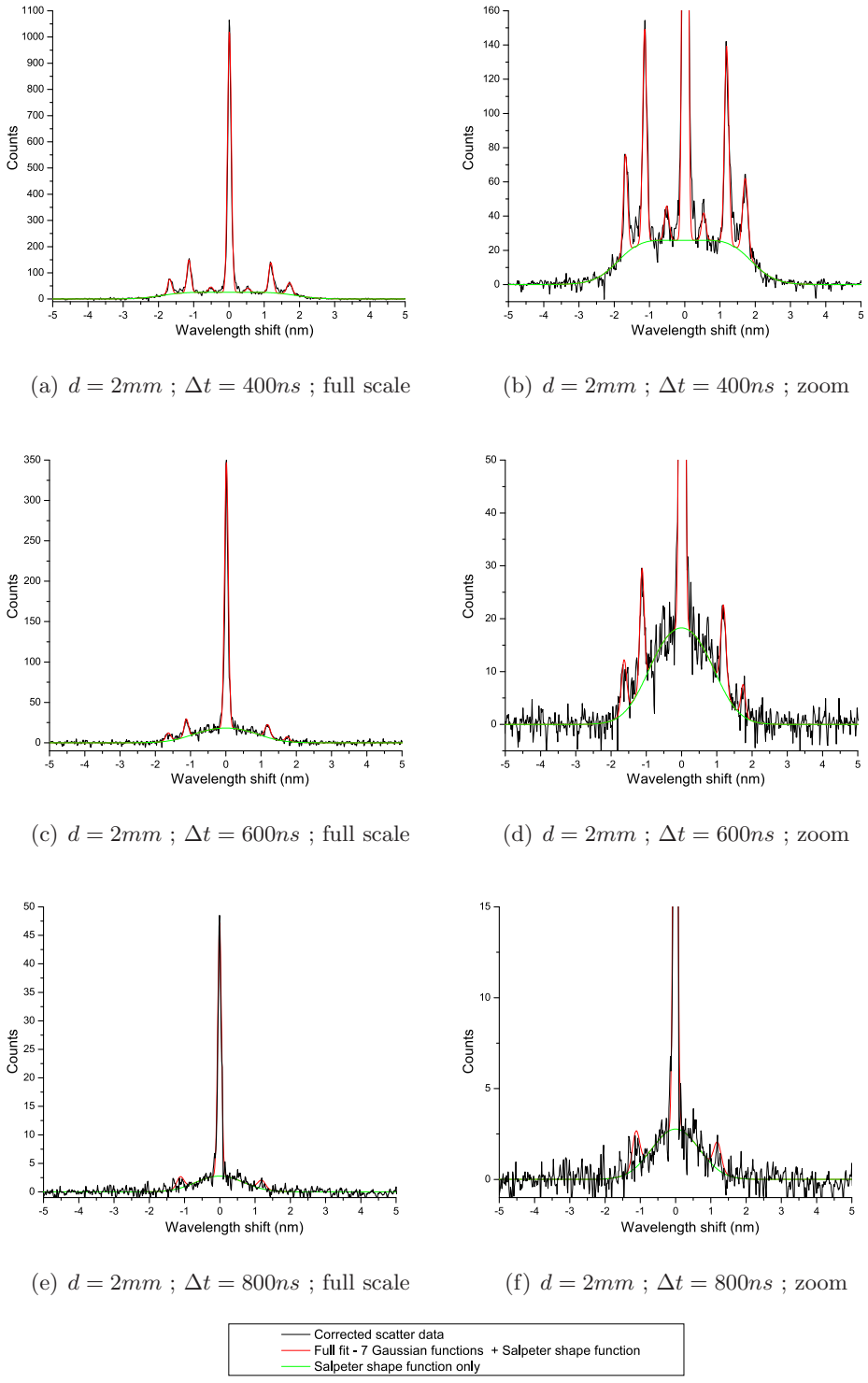


(a) $d = 2mm$ ; $\Delta t = 400ns$ ; full scale

(b) $d = 2mm$ ; $\Delta t = 400ns$ ; zoom

(c) $d = 2mm$ ; $\Delta t = 600ns$ ; full scale

(d) $d = 2mm$ ; $\Delta t = 600ns$ ; zoom

(e) $d = 2mm$ ; $\Delta t = 800ns$ ; full scale

(f) $d = 2mm$ ; $\Delta t = 800ns$ ; zoom

Figure 5.7: Corrected scatter spectra fitted with Gaussians for the Raman and Rayleigh features, and using the Salpeter approximation for the Thomson signal. These spectra were obtained $2mm$ from the target surface and at different time delays, $400ns$ (a) - (b), $600ns$ (c) - (d), and $800ns$ (e) - (f). Each data set results from the accumulation of several laser shots, normalised to 1 shot and corrected for stray light and self emission.

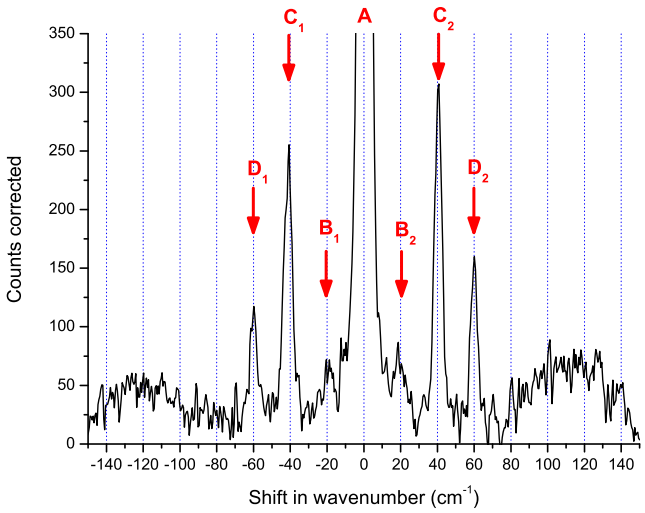


Figure 5.8: Line out of a scatter spectrum from a Mg plume shown in figure 5.1(a). The probe is $2mm$ from the target surface, $200ns$ after the plasma formation. The feature A is the expected Rayleigh peak. Features, $B_2$, $C_2$ and $D_2$ are respectively $\sim 20cm^{-1}$, $\sim 40cm^{-1}$ and $\sim 60cm^{-1}$ on high wavenumber side (short wavelength side) of the Rayleigh peak as are $B_1$, $C_1$ and $D_1$ on the low wavenumber side (long wavelength side).

### 5.3.1 Atomic Raman scattering

There are evidently 3 peaks at separations of $\sim 20cm^{-1}$, $\sim 40cm^{-1}$ and $\sim 60cm^{-1}$ from the Rayleigh peak. Figure 5.9 is showing the evolution with time delay at a fixed distance and the evolution with distance at a fixed time delay of two of these peaks, satellite $C_2$ and satellite $D_2$ on the higher wavenumber side. It is clear that the position of the peaks do not vary with plasma conditions. The presence of molecules such as $MgH$, $MgO$ or $Mg_2$ resulting in a molecular Raman scattering signal was considered. However, care was taken experimentally to lower the chamber vacuum by an order of magnitude, and the target was polished to reveal a clean surface. No dif-

ference in the satellite intensity was observed when changing the chamber pressure or with the number of shots fired successively on the target to generate the plasma. Moreover, the spacing is not consistent with rotational Raman features of any of these molecules. The probing laser frequency is not resonant with any of the Mg plasma transitions [56], so they are not satellites of the type observed previously [87, 88, 89]. We identify them as atomic Raman type transitions from neutral Mg.

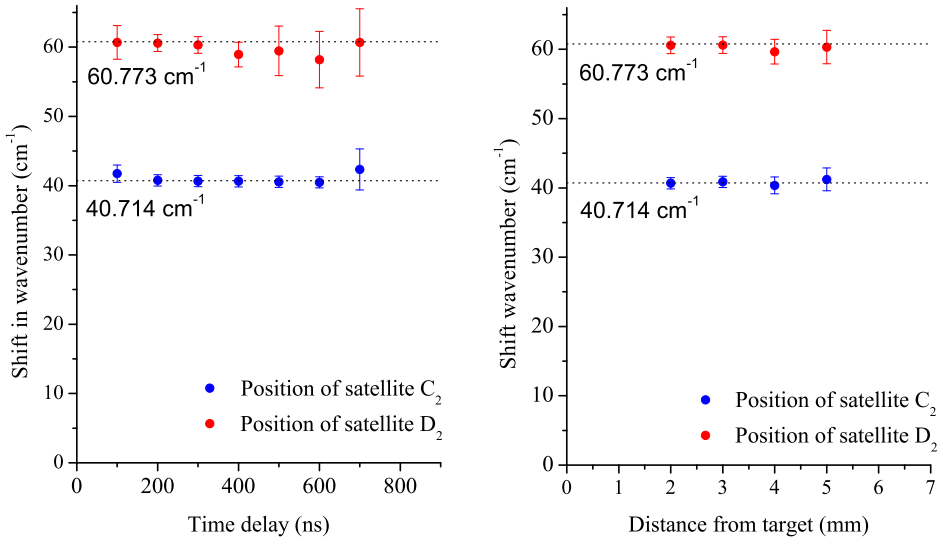


(a) $d = 2mm$ (b) $\Delta t = 200ns$

Figure 5.9: Position of the Raman satellites $C_2$ and $D_2$ (see figure 5.8) for different time delays (a) and different distances from the target surface (b).

For $MgI$ the ground state is $^1S^0$ and the first excited term is $^3P^0$ - this is a metastable radiative decay to the ground state with a decay time of $\sim 3.9ms$ ($A_{ji} = 2.54 \times 10^2 s^{-1}$ [56]) and so it might be expected to be present in the ablated plume in significant numbers. To get an estimate of the population distribution of a state, partial local thermodynamic equilibrium (PLTE) can be assumed. In that case, the population distribution of any two

states with energies $E_a$ and $E_b$ can be related by the Boltzmann factor [19]

$$\frac{N_a}{N_b} = \frac{g_a}{g_b} exp\left(-\frac{E_a - E_b}{k_B T}\right) \tag{5.3}$$

N refers to the population in the given quantum state, and g is the statistical weight.

The relative population can be computed as a function of temperature. Figure 5.10 shows the results of this calculation including the first 40 excited states of $MgI$ as given in the National Institute of Science and Technology [56]. If we consider the case of the plasma $2mm$ from the target surface and $200ns$ delay, the temperature $k_B T \sim 1.5eV$, and we can then estimate $\sim 23\%$ of ions in metastable state.

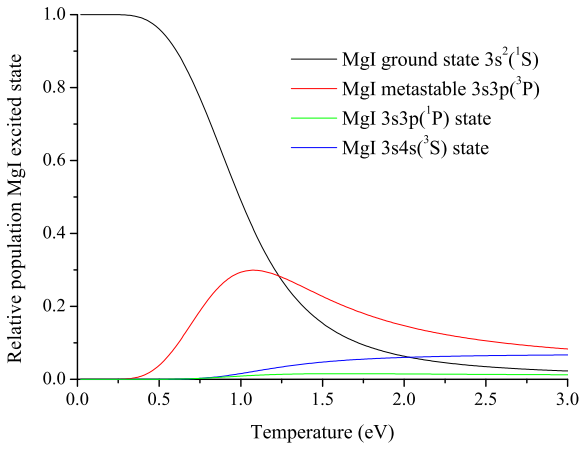


Figure 5.10: Relative population of $MgI$ excited states calculated using the Boltzman equation 5.3 including 40 excited states. Only the first four states are represented for clarity, the other 36 curves lying under the blue curve.

The energy levels for the ${}^3P^0$ term are represented in figure 5.11. If an incoming photon is absorbed by an atom in one of the J levels of this term and

then on emission the electron returns to another J level the emitted photon wave-number will differ from the incoming photon by $\sim 20.059cm^{-1}$, $\sim 40.714cm^{-1}$ and $\sim 60.773cm^{-1}$. This matches very well, the recorded shifts (see figure 5.9), in particular for early time data, when the intensity of the satellites is significant.

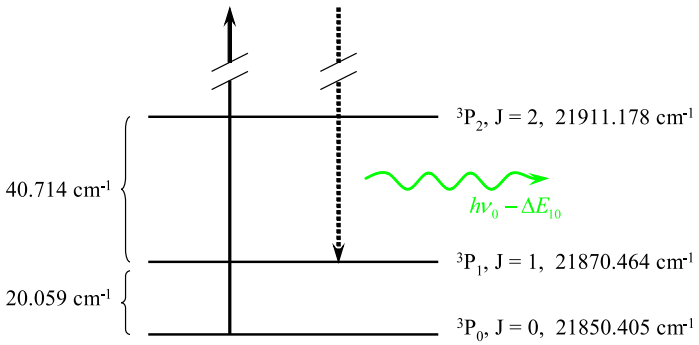


Figure 5.11: Energy levels for the $^3P^0$ term of $MgI$.

We have checked the hypothesis of the origin of the satellites by using an aluminium target. Scatter spectra from an Al plasma at different time delays are shown in figure 5.12. The spectra were taken under similar ablation and probe condition, and with the same scattering geometry than the spectra of magnesium plasma presented so far. The ablating laser energy per pulse was measured to be $\sim 290mJ$, and the probing laser about $\sim 400mJ$. We observed similar satellites at a separation of $\sim 112cm^{-1}$ either side of the Rayleigh peak. From the National Institute of Science and Technology data bases [56], the separation of the J = 1/2 and J = 3/2 levels of the $AlI$ ground state term is $112.061cm^{-1}$. This second observation supports strongly the hypothesis of the origin of these satellites.

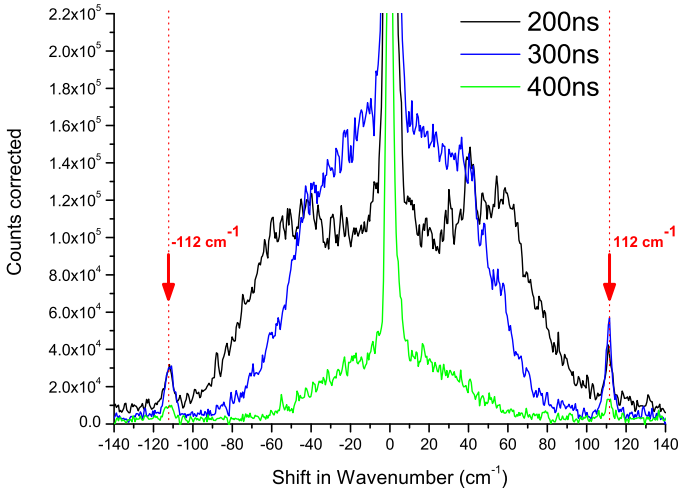


Figure 5.12: Line out of scatter spectra from an Al plume. The probe is $2mm$ from the target surface at different time after the plasma formation.

### 5.3.2 Raman satellites discussion

These unexpected results, triggered a theoretical work on Rayleigh and Raman cross-sections, briefly presented in section 3.5. Sahoo started with calculating these cross-sections for the $Mg$ $(3s3p)$ metastable state, as well as the ground state of $Mg$ $(3s^2)$ for Rayleigh scattering [69]. These calculations were done for an incident energy corresponding to the wavelength of $532nm$ of the probing laser used in the present experiment, and are presented in figure 3.5.

Figure 5.13 shows the evolution of ratios of Rayleigh signal over Raman signal with time, $2mm$ away from the target surface (fig. 5.13(a)) and with distance for a fixed time delay of $200ns$ (fig. 5.13(b)). A relatively early

time was chosen for figure 5.13(b) so that the features are strong enough even further away from the target surface. All data presented concern $Mg$ plasma probed with a fluence of $\sim 50J/cm^2$, generated with an ablating laser of fluence $\sim 10J/cm^2$. Since experimentally, an asymetry was observed between the Raman features on the positive side of the spectrum and their equivalent on the negative side, the ratios were calculated for both low and high wavenumber sides. The results of these ratios from the values of the calculated cross-sections are represented in red. Although calculations are only on a preliminary stage at the time of this thesis, a few conclusions may be brought forward from figure 5.13 and section 3.5.

The metastables might be a small fraction of the total atomic density, contrary to initial thoughts lead by the relatively long lifetime of the metastable state of $Mg$ ($3.9ms$). This revised assumption follows calculations of the cross section from metastable state, found to be about 40 times greater than the ground state [69], so the Rayleigh scattering from species in metastable state would dominate even if their relative population is small.

Figure 5.13(a) shows that the ratio of Rayleigh signal to Raman satellite C signal starts high, then drops close to the expected ratio for metastables and then rises again. This can be explained by variations in the population of metastables relative to the ground state and ions. At first the ionisation level can be expected to be higher so that the total Rayleigh signal includes the scattering from many ions from the ground state of singly ionised $Mg$, as well as other excited species. For example, species from the ($^1P$) excited level might produce a strong Rayleigh signal and not show any satellite as there is only one $J$ state [56]. At a later time, from $300ns$, recombination processes would result in more contribution from neutral $MgI$, and the metastables might dominate as we have seen that the cross section is about

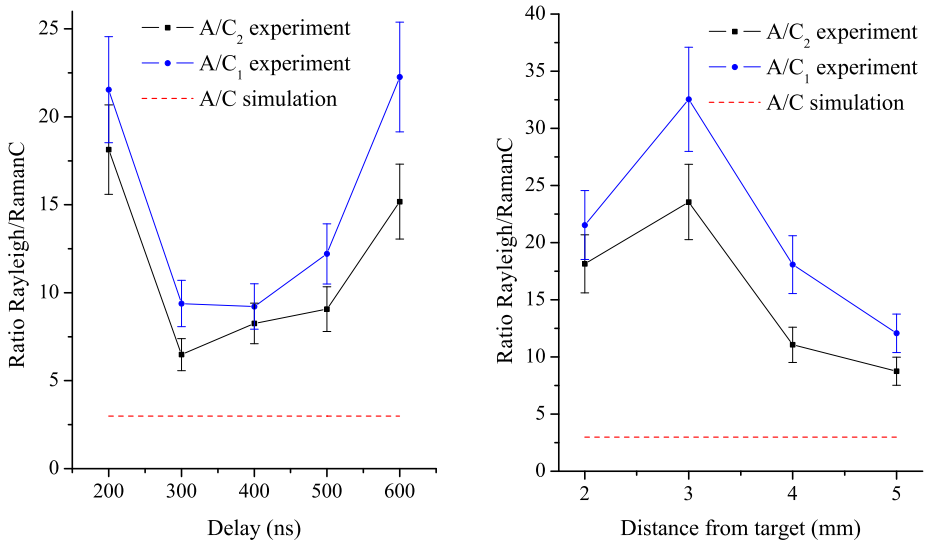


(a) $d = 2mm$ (b) $\Delta t = 200ns$

Figure 5.13: Ratios of the Rayleigh peak intensity over the Raman peaks C intensity of spectra such as presented in figure 5.8 of Mg plasma (a) probed at $d = 2mm$ away from the target surface with different delays and (b) probed at a time $\Delta t = 200ns$ after the initiation of the plasma at different distances from target surface. The red lines are similar ratios from the calculated Rayleigh and Raman cross-sections (figure 3.5). This is giving indications of the ratio of total number of ions and atoms over the number of metastable ions.

40 times larger than for the ground state. Finally, the rise after $400ns$ indicates that there might be fewer species in metastable state relative to the ones in ground state, perhaps because it is colder plasma vapor, so the total Rayleigh signal rises relative to the satellites.

Similarly, in figure 5.13(b) we can see that the ratio is peaking at $3mm$ and then falling away from the target surface, showing that the concentration of species is not uniform in the plume at any one time. A higher relative population of ionised species might be concentrated in the region $3mm$ from the target surface, at a time $\Delta t = 200ns$. Further out, recombination to

the metastable state might occure. The presented sequences of evolution of atomic species within the plume have to be considered as hypothetical. As a matter of fact, there are many different species involved in the processes, and excited states are likely to dominate with large cross sections even if their relative population is small.

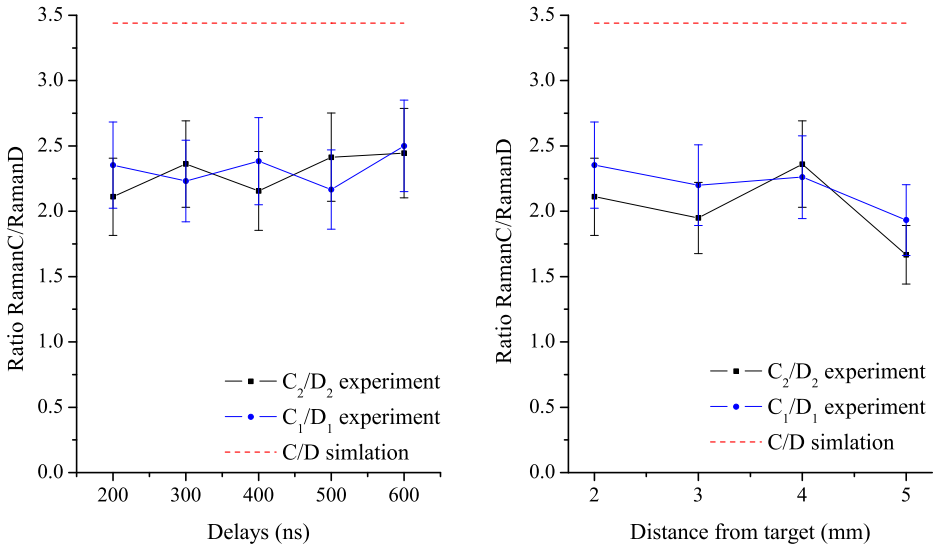


(a) $d = 2mm$ (b) $\Delta t = 200ns$

Figure 5.14: Ratios of Raman peaks C intensity over Raman peaks D intensity (on the positive and negative side of the spectra) varying with time at a fixed distance from target (a) and with distance at a fixed time delay from the initiation of the plasma (b). The expected value from figure 3.5 is represented in red.

Figure 5.14 shows a relatively constant ratio between the Raman feature intensity of peaks C and D, at a fixed distance from target and varying the time delay, or at a fixed time delay and different distances from target. The ratio is of the same order of magnitude as the expected value from the calculated cross-sections. The peaks B in the experimental data are much weaker and affected by the underlying Thomson signal, and the wings of

the strong Rayleigh signal. Nevertheless, the three features on each side of the central peak still seem consistent with the expected ratio of $1 : 3.6 : 1.1$ going outwards from the central Rayleigh peak. However, the calculated Raman peaks presented in section 3.5 (shown in figure 3.5) appeared to be very sensitive to the accuracy of the energy levels for intermediate states of Mg and might require experimental data as a benchmark [69].

Atomic Raman scattering has the potential to be used as a diagnostic of the relative population of some excited states, thus helping to get absolute measurements of the ionisation fraction in plasma plumes. Further experimental and theoretical work are still needed to reach conclusive results.

## 5.4 Uncertainties

In this section, the validity of the Thomson scattering results, and the resolution by which the electron density and temperature are measured in the plasma will be discussed. There are a number of sources of errors that need to be considered in order to evaluate the uncertainties associated with the Thomson scattering measurements in laser produced plasmas. These errors can be classified in three categories, the ones associated with the plasma formation and evolution, the ones associated with the probe laser and interaction of photons with the plasma, and the ones associated with the detection and interpretation of the data. The uncertainties in this work were mostly determined by the accuracy by which the scatter spectra could be fitted, as described in the later discussion. Before that, sources of errors, matter for the first two categories will be discussed.

### 5.4.1 Reproducibility

Change in the scattering signal from one spectrum to another can occur due to a statistical error induced by:

- reproducibility of the plasma, associated with the reproducibility of the ablating laser pulse,
- changes in the plasma during the sequence of measurements,
- reproducibility of the probing laser pulse.

Figure 5.15 shows series of spectra taken at different times of the day, or the week, under similar conditions. The spectra are row data and each of them is the result of the accumulation of 100 shots. A small difference can be observed from one spectrum to another, but one can note that the general shape of the spectrum remains constant. There are therefore reasons to believe that by accumulating a large number of shots, this error can be neglected and the scattering signal can be considered as reproducible. Changes in the spectral shape might occur as well from the substraction process to obtain the corrected Thomson scattering spectrum. Once again, a large accumulation of data reduces any changes.

### 5.4.2 Perturbation of the plasma by the probe

The main issue we have to address regarding the validity of the scatter results is perturbation of the plasma by the probe. If we assume absorption of the probe pulse in the plume occurs by inverse bremsstrahlung, we can calculate the absorption coefficient $\alpha_{IB}$ for a given plasma electron density and temperature (see section 5.4). Rybicki [47] gives an expression for the free-free absorption coefficient in $cm^{-1}$ as follows:

$$\alpha_{IB} = 3.7 \times 10^8 \frac{Z^2 n_e n_i}{T^{1/2} \nu^3} \left(1 - e^{-h\nu/k_B T}\right) \bar{g}_{ff} \tag{5.4}$$

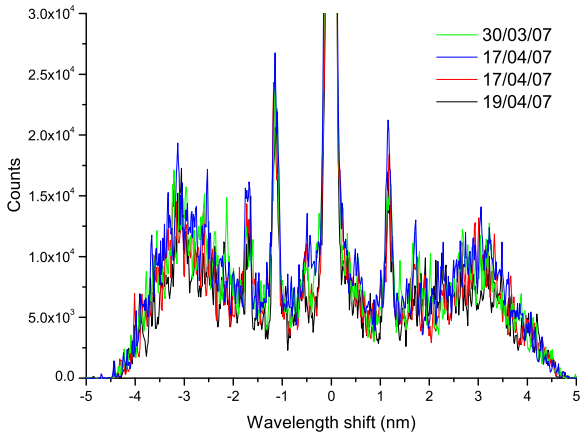


Figure 5.15: Line out of scatter spectra of Mg plasma ($d = 3mm$, $\Delta t = 200ns$) recorded at different moment within the same day, from one day to another, and from one week to another.

In this expression, the temperature T is in kelvin, $h$ is the Planck's constant $= 6.625 \times 10^{-27} erg.s$, $k_B$ is the Bolzmann's constant $= 1.38 \times 10^{-16} erg.K^{-1}$, the average degree of ionisation Z is taken as 1, $\nu$ is the frequency of the incoming photons, the Gaunt factor $\bar{g}_{ff}$ is assumed to be of the order of unity. The electron and the ion density are assumed to be equal. Using this formula, it was found that for the highest density case, where $n_e = n_i = 8.7 \times 10^{16} cm^{-3}$ and $T_e = 1.5eV$ or $17400K$ the absorption coefficient $\alpha_{IB} \approx 9.3 \times 10^{-5} cm^{-1}$.

If we assume, in the worst case scenario, that the energy absorbed is not conducted away during the pulse, then the heating per electron is $\sim (F \cdot \alpha_{IB})/n_e$, where F is the fluence of the probe. In our case, the fluence of the laser beam on the plasma volume probed is $F \sim 50 J/cm^2$. The heating per electron for a portion of plasma $2mm$ from the target surface and at

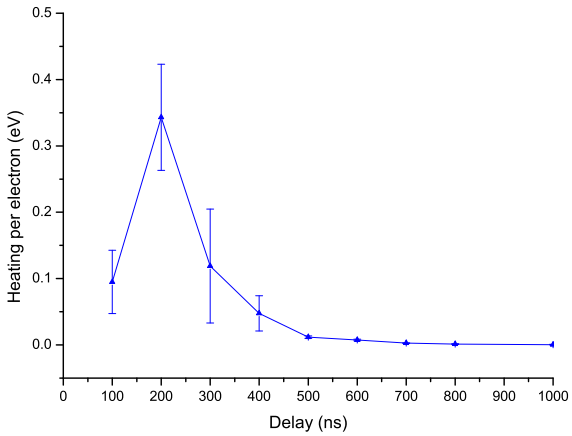


Figure 5.16: Heating per electron of the plasma by the probe beam considering absorption of the probe pulse is by inverse bremsstrahlung. The heating is calculated for plasma at different time delays, probing the plasma $2mm$ from the target surface.

different time delays is shown in figure 5.16. As expected, the perturbation of the plume is the most critical when the plasma is denser with a heating of $\sim 0.34eV$. This is $\sim 20\%$ of the total temperature assuming the worst case. This value drops below 10% for the next point ($300ns$), and as the plasma cools and expands, it becomes an even more marginal effect, as shown in figure 5.16.

In order to investigate further the effect of plume heating by the probe, the experiment was repeated for the higher density case, for $d = 2mm$ and $\Delta t = 200ns$, for different probe laser energies. To control the intensity of the probe laser beam a polariser and a half wave plate were used, as described in section 4.2.1. For this set of data, the Rayleigh peak was suppressed by placing a physical block directly in front of the CCD chip. The data could then be accumulated for longer without risking to saturate the detector. Figure 5.17 shows the results of the scatter signal using three quarter of the probe energy or half of the probe energy. The spectra, corrected for stray

light and self emission, are the result of the accumulation of 1000 shots, normalised to 1 shot, and then multiplied by a factor corresponding to the loss of probe energy ( $\times 1.3$ when the probe energy is $\sim 310mJ$ and $\times 2$ when the probe energy is $\sim 200mJ$) to facilitate the comparison. The resulting scatter spectra were fitted with the Salpeter model to get the electron temperature and density from the experimental spectra, as described in section 5.2.2. The results are summarised in table 5.2.

The temperature was measured to be $\sim 1.5eV$ when using the full probe energy, so it is clear that the probe has an effect on the plasma in the higher density case. This effect represent $\sim 23\%$ of the total temperature and is the major source of error for the higher density case. However, in these last measurements, the position could have been affected when lowering the energy (i.e. rotating the half-wave plate). This would affect as well the scattering signal detected.

An intense laser beam can increase the ionisation degree in partially ionised plasmas in addition to the heating discussed in the previous paragraphs. However, in the case of the present experiment, the probe photon energy ($2.33eV$) is smaller than the ionisation energy from the ground state ($7.65eV$) and the first excited levels [56] and thus, it is unlikely that photo-

Table 5.2: Investigation of the effect of the probe laser energy.

| Probe energy (mJ) | Electron density $n_e$ ($cm^{-3}$) | Electron temperature $T_e$ ($eV$) |
|---|---|---|
| $\sim 400$ | $n_e = (8.7 \pm 0.8) \times 10^{16}$ | $T_e = 1.5 \pm 0.2$ |
| $\sim 300$ | $n_e = (4.9 \pm 0.3) \times 10^{16}$ | $T_e = 1.29 \pm 0.08$ |
| $\sim 200$ | $n_e = (4.1 \pm 0.3) \times 10^{16}$ | $T_e = 1.15 \pm 0.05$ |

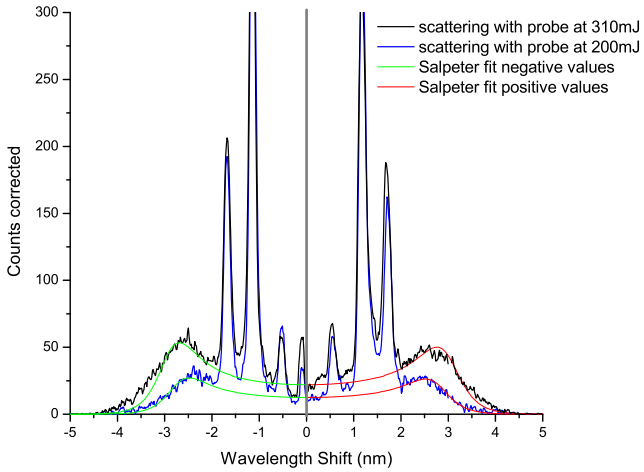


Figure 5.17: Line out of scatter spectra of Mg plasma ($d = 2mm$, $\Delta t = 200ns$) probed with the laser set to different energies of $\sim 300mJ$ (3/4 of full energy) and $\sim 200mJ$ (1/2 of full energy). The spectra are normalised to the full energy. Each spectrum is fitted with the Salpeter model (section 3.3.2). The Rayleigh peak is suppressed using a block placed in front if the CCD chip and represented by the grey line.

absorption plays any role in the atomic plume. Experimentally, no obvious increase in emission was observed as a result of the probe.

### 5.4.3 Evaluation of error bars for $n_e$ and $T_e$

For each electron density and electron temperature measured, an associated error was evaluated, depending on the method used to analyse the experimental scatter spectra.

For the late time plasmas, analysed by fitting a Gaussian, as described in section 5.2.1, the error bars shown in figures 5.18 and 5.19 were estimated by calculating the propagation of errors in equation 5.2 for the electron temperature and equation 5.1 for the electron density. The errors in the Rayleigh

and Thomson cross-sections are taken respectively from [68] and [2].The error on the width of the scatter signal and the area under the scatter signal are given by the fitting procedure. The other sources of errors that were considered are the scattering angle estimated by 5%, the probe laser wavelength known by $0.2nm$ [78], the pressure of cold gas in the chamber which accuracy was determined considering a systematic error of $\pm 1mbar$.

For early time plasmas, analysed by fitting a theoretical spectra, as described in section 5.2.2, the error bars were estimated from the fitting itself. In order to estimate these uncertainties along with the fit, the data was fitted manually until the fit was judged unacceptable, defining an upper and lower limit reflected in the error bars on the result graphs 5.18 and 5.19. The errors are particularly significant when the Raman features are overlapping the electron features of the Thomson signal, making it harder to distinguish the contribution of each phenomena. Moreover, for these data, the electron features are no longer sharp, as the value of the scattering parameter $\alpha$ (from equation 3.7) is getting close to 1. When $\alpha \gg 1$, small variations in the density and the temperature induce significant changes in the shape of the calculated scattered spectra. This is no longer the case when $\alpha$ gets close to 1. As a result, the steps at which $T_e$ and $n_e$ were varied had to be larger to induce a noticeable change, reducing the accuracy of the results, as shown by the error bars in figure 5.18 and 5.19.

## 5.5 Results and discussion

In this section, the spatial and temporal distributions of electron temperature and density of the Mg laser produced plasma were determined from Thomson scatter spectra.

### 5.5.1 Axial expansion of the plasma

All data presented in this section relate to species travelling perpendicular to the target surface along the symmetry axis of the plasma.

Figure 5.18(a) shows the evolution of the electron density and temperature with time at $2mm$ from the target plane, corresponding to the spectra shown so far in this chapter. The three other graphs in figure 5.18 and 5.19 are showing the evolution further away from the target surface, $3mm$ (fig. 5.18(b)), $4mm$ (fig 5.19(a)) and $5mm$ (fig. 5.19(b)).

These densities and temperatures are consistent with previous results. Measurements using interferometry and combined absorption spectroscopy and laser induced fluorescence were performed previously on laser ablated Mg plume [9, 10, 22, 81]. The ablation conditions were similar to the ones of the Mg plasma under study in this work. Due to each diagnostic restrictions, the time, space and species of the plasma studied are not necessarily the same as the ones resulting from Thomson scattering measurements performed here. However, it is still interesting to summarise what is already known about the plume, to put the new results in perspective. Some of these previous measurements are presented in table 5.3. From this summary, it appears that the time of expansion between $100ns$ and $1\mu s$ (presented in figure 5.18) has not been studied before. However, it is not surprising to see that close to the target and at early times, the electron density was found to be nearly 2 orders of magnitude higher than the maximum of $\sim 8.7 \times 10^{16} cm^{-3}$ measured with the Thomson scattering diagnostic developed in this work. The density of ground state species ($MgI$) is an order of magnitude higher than the electron density measured 2mm from the target at $1\mu s$ delay which in turn is higher than the density of singly ionised species ($MgII$). This would be explained by a significant number of neutrals in the plume at late times

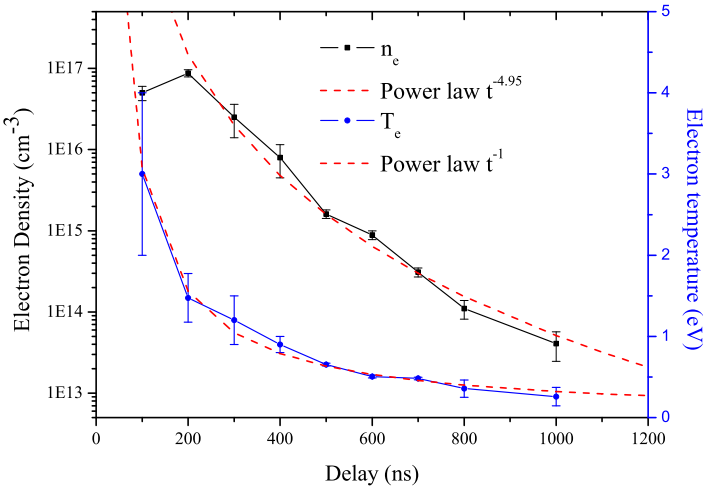


(a) $d = 2mm$

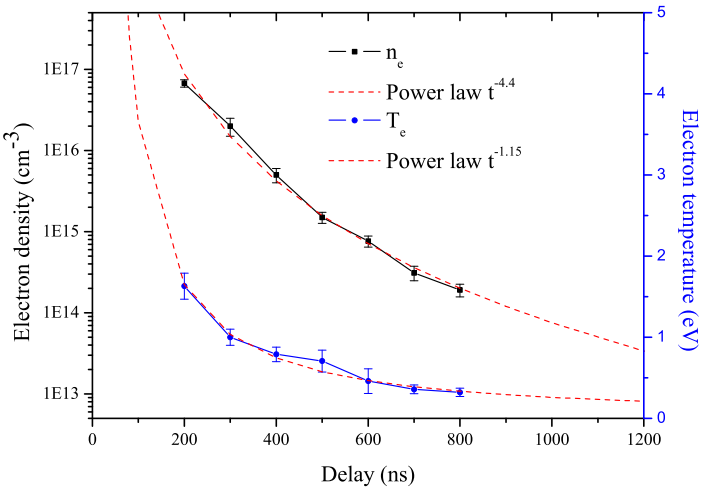


(b) $d = 3mm$

Figure 5.18: Axial evolution of the electron density and temperature with time delay, for plasma probed $2mm$(a) and $3mm$(b) from the target surface. The ablating laser had an energy of $\sim 10J/cm^2$ and the probing laser $\sim 50J/cm^2$. Up to $500ns$ delay, $T_e$ and $n_e$ were obtained from theoretical fits (section 5.2.2); after $600ns$ delay, the method using an Ar gas calibration was used (section 5.2.1). The data at late times are fitted with power laws of the form $bt^{-a}$ where a and b are constants determined by the best fit, and t the time delay.

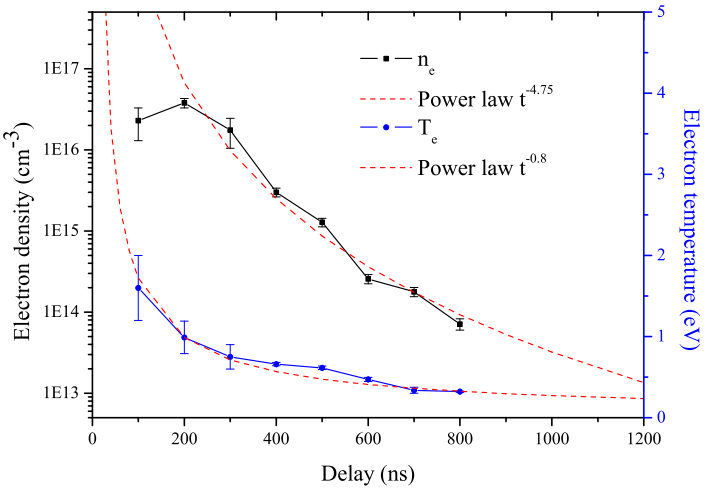


(a) $d = 4mm$

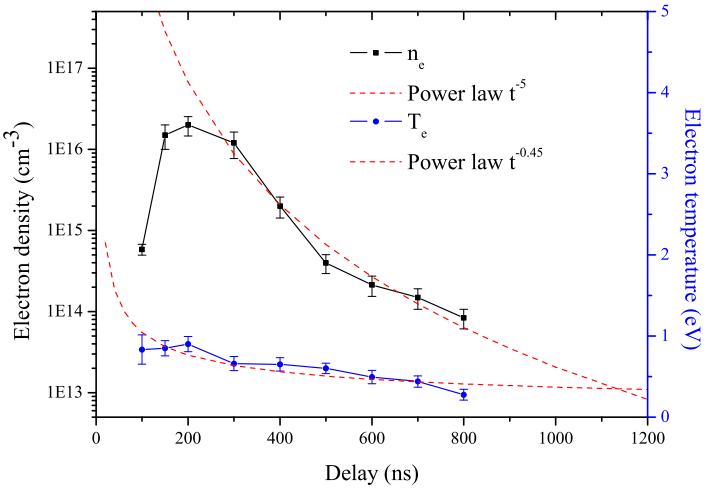


(b) $d = 5mm$

Figure 5.19: Axial evolution of the electron density and temperature with time delay, for plasma probed $4mm$(a) and $5mm$(b) from the target surface. The ablating and probing conditions are the same than in figure 5.18. Up to $400ns$ delay, $T_e$ and $n_e$ were obtained from theoretical fits (section 5.2.2); after $500ns$ delay, the method using an Ar gas calibration was used (section 5.2.1). The data at late times are fitted with power laws of the form $bt^{-a}$ where a and b are constants determined by the best fit, and t the time delay.

and will be discussed further in the next section.

Table 5.3: Densities of electrons, ground state species ($MgI$) and singly ionised species ($MgII$) mesured by interferometry (Interf.), absorption spectroscopy (AS) and laser induced fluorescence (LIF), at different times and positions of an expanding Mg plasma.

| Species | Delay ns | Distance from target mm | Density ($cm^{-3}$) | Diagnostic | Ref. |
|---|---|---|---|---|---|
| $e^-$ | 50 | 0.5 | $n_e \approx 4 \times 10^{18}$ | Interf. | [22] |
| $e^-$ | 85 | 0.5 | $n_e \approx 2.2 \times 10^{18}$ | Interf. | [22] |
| $MgI$ | 1000 | 2 | $n_{MgI} \approx 1.2 \times 10^{15}$ | AS + LIF | [81] |
| $MgII$ | 1000 | 2 | $n_{MgII} \approx 2 \times 10^{13}$ | AS + LIF | [81] |
| $MgI$ | 2000 | 20 | $n_{MgI} \approx 1.3 \times 10^{12}$ | AS | [9] |
| $MgI$ | 5000 | 50 | $n_{MgI} \approx 1.2 \times 10^{11}$ | AS | [9] |

The speed of the leading edge of the plume can be estimated from the temporal evolution of the density. One can see in figures 5.18 and 5.19 that more spectra would have been required in the temporal region $100 - 300ns$ to determine with more accuracy when the electron density is peaking. However, the expansion velocity can be estimated to be $\sim (1.3 \pm 0.2) \times 10^6\ cm.s^{-1}$, as the electron density can be expected to reach a maximum before $200ns$ at $2mm$, and after $200ns$ at $5mm$ within the $100-300ns$ time interval. The Mg plasma under study has a temperature typically around $1eV$, so the free electron mean thermal speed, expressed as:

$$c_e = \left(\frac{2\kappa_B T_e}{m_e}\right)^{1/2} \tag{5.5}$$

is of the order of $10^7 cm.s^{-1}$. This is an order of magnitude higher than the experimentally measured expansion velocity. Therefore, the electron velocity measured represents the ion flow velocity with the free electrons constrained

to move within the plasma plume. Figure 5.20 shows the temporal evolution of the total density calculated using an isothermal model, as described in section 2.2, for plasma at different distances from the target. The axial velocity was set to $1.3 \times 10^6 cm.s^{-1}$, and the density peaks at expected values compared to the experimental data presented in figures 5.18 and 5.19. However, it can clearly be seen that in the experimental data, the density is falling much more rapidly than considering a simple adiabatic expansion in an isothermal model or in an isentropic model, as shown in figure 5.20 or in figure 2.3.

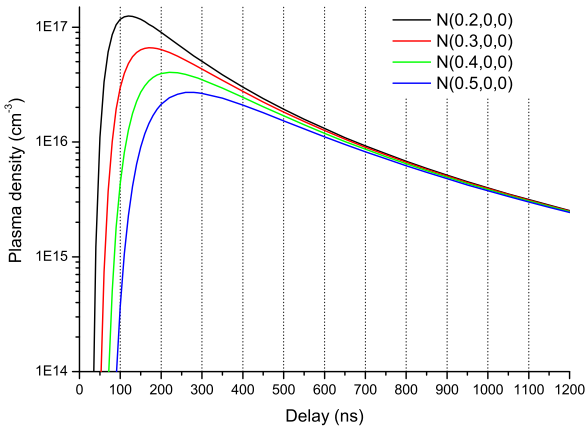


Figure 5.20: Temporal evolution of the total density, $N$, of a Mg plasma calculated using an isothermal model (section 2.2) with an axial velocity of $1.3 \times 10^6 cm.s^{-1}$.

#### 5.5.1.1 Axial evolution of the electron density

As discussed in section 2.2, assuming an adiabatic expansion of the plasma plume after the laser pulse, theoretical calculations show that the electron density varies with time as $n_e \propto t^{-3}$. However, in the time scale considered

in this work, the fits to the experimental data give a power-law dependence for the electron density of $bt^a$, with $a$ varying from $-4.4$ to $-5$, depending on the plasma volume (see figures 5.18 and 5.19). On the other hand, the intensity of the Rayleigh scattering signal, proportional to the density of atoms follows the density scaling power-law, as shown in figure 5.21. Qualitatively, there are two explanations for this dependence, that can be detailed as follows.

A first explanation to these results would be due to the fact there may be strong spatial gradients of ionisation within the initial heated slab of plasma. The measurements are made at a fixed point in space, and the plasma flowing through this point at later time might have started out with a lower ionisation. For a self-similar expansion, we should observe a temporal variation when the density is probed at a fixed point relative to the target surface. Simulations of similar laser ablated plumes [83] indicate that at the end of the heating pulse, we expect to have a plasma slab of uniform temperature but sharply increasing electron density inwards from the target surface. Although the graphs in reference [83] are not showing the fraction of ionisation for these cases, a fall in the ionisation with electron density for a fixed electron temperature can be assumed, countered by a sharp rise in mass density. In the absence of recombination, we should see this translate into a rise in electron density with time rather than a fall. However, this conclusion has to be taken carefully, as there might be later cold material evaporated after the uniform slab shown in the simulations.

Secondly, recombination processes within the plume are expected as the temperature drops due to expansion. Three major recombining mechanisms were considered: three body recombination (3BR), radiative recombination (RR) and dielectronic recombination (DR). The processes and their recom-

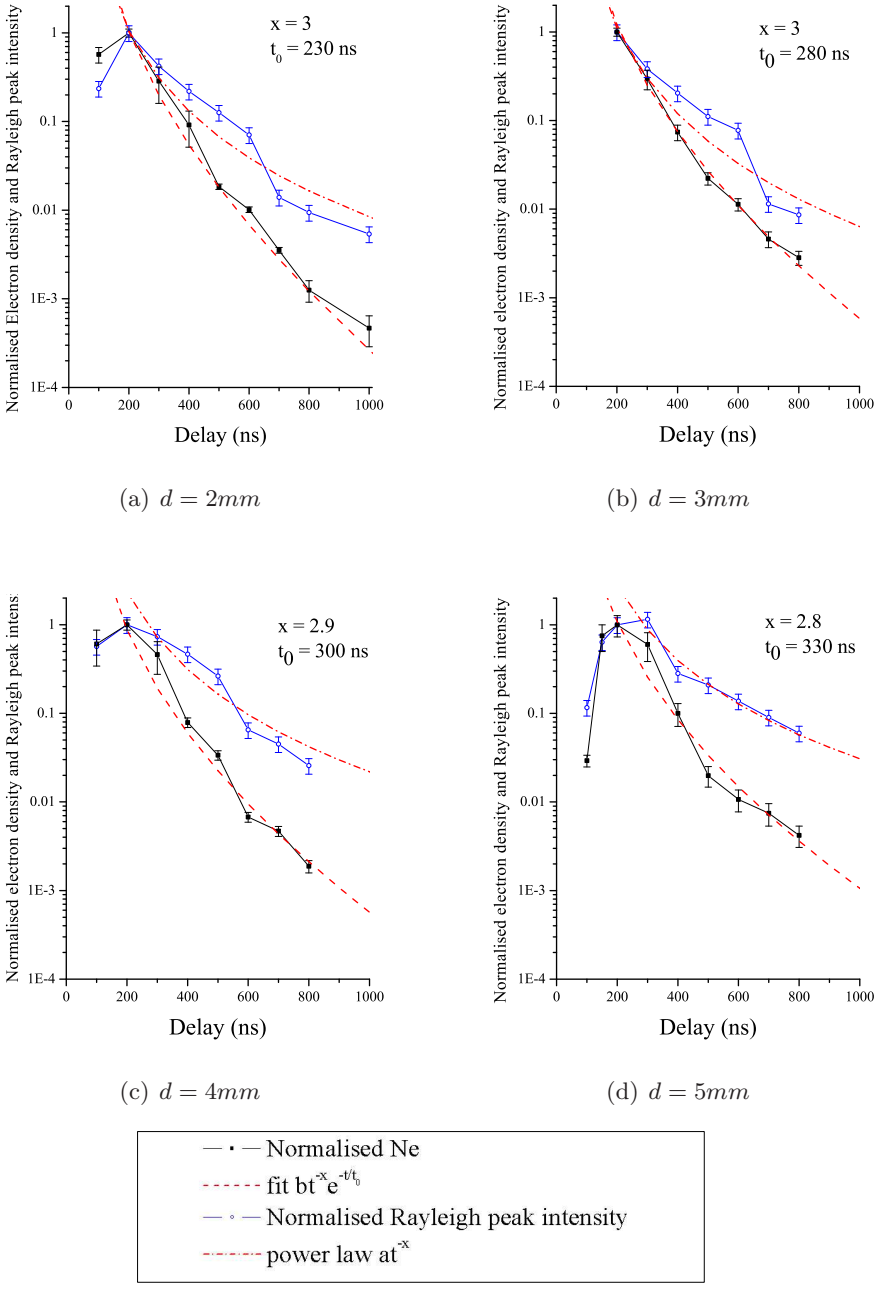


(a) $d = 2mm$ (b) $d = 3mm$

(c) $d = 4mm$ (d) $d = 5mm$

Figure 5.21: Axial evolution with time of the density of electrons, compared to the Rayleigh scattering intensity, proportional to the number of atoms, in the Mg plasma plume $2mm$ (a), $3mm$ (b), $4mm$ (c), and $5mm$ (d) from the target normal. The evolution of the number of atoms is fitted with a power law of the form $at^{-x}$ and the electron density with an exponential power law of the form $bt^{-x}e^{-t/t_0}$, where $x \approx 3$, a and b are fitting constants, and $t_0$ is the average relaxation time.

bination rate coefficients are summarised in section 2.3. The calculation of recombination times for RR and 3BR, using equations 2.21 and 2.19 respectively are suggesting a time for relaxation to ionisation stage equilibrium increasing rapidly from $20\mu s$ to over $40ms$ during the microsecond timescale where the present measurements were made. As described in section 2.3, reliable values of the DR rates coefficient are difficult to obtain, and little work has been done in the regime of low temperature, and low density plasmas. Calculations using equation 2.22 suggest a significant contribution to the total recombination rate for temperatures around 1 eV. However, it still gives a rather large relaxation time of $\sim 1\mu s$ at early times. Assuming that the ionisation state drop is wholly due to recombination, a power law decay can be assumed for plasma expansion and an exponential decay law for recombination. The average relaxation time can then be estimated experimentally by fitting a power law of the form $at^{-x}$ to the density of atoms (given by the Rayleigh peak intensity) and a law of the form $bt^{-x}e^{-t/t_0}$ to the electron density. Here $a$, $b$ and $x$ are constants and $t_0$ is the average relaxation time. The results of the fittings for plasma probed at different distances from the target plane are shown in figure 5.21. $x \approx 3$ in the 4 cases, reflecting an adiabatic expansion of the plasma at late times as discussed in section 2.2. The experimental average relaxation time is estimated to be ranging from $\sim 230ns$ to $\sim 330ns$ as the plasma probed is further away from the target surface. This is shorter than the expected time. On the other hand, calculations of the DR rate are uncertain. For example, previous experimental measurement of the DR cross-section, made by crossing beams of electrons and singly ionised magnesium, $MgII$ [53] suggests a cross-section larger than the calculated values by a factor of 5. This result would bring the calculated DR rate close to what is observed experimentally and would allow us to explain the present data entirely in terms of recombination.

Other loss mechanisms not considered here might be present in this type of plasma. Another loss mechanism that could be considered is molecular recombination of $Mg_2$. However, in such a case, one would expect the Rayleigh peak to decrease more than observed, and there is no evidence of rotational molecular Raman features in the spectra recorded (see for example figure 5.8).

This discussion emphasises again that work is still required in this area, and it is difficult to be conclusive as the physics of the plume is not simple.

#### 5.5.1.2 Axial evolution of the electron temperature

The electron temperature is found to decay with a dependence $T_e \propto t^{-1}$, as shown in figure 5.18 for the plasma volumes probed in this work closer to the target. This is in agreement with previous experiments and analytical calculations [39]. This cooling rate is slower compared with a simple adiabatic expansion where $T_e \propto t^{-2}$ as described in section 2.2. This can be explained by transfer of energy to electrons by three-body recombination which is expected to become important at a time when the free electron thermal energy has fallen to much less than the ionisation energy. According to Rumbsy *et.al.* [39], in this situation a very small 3BR rate can lead to sufficient energy transfer to the electron to make a large change in the electron temperature decay rate without necessarily affecting the density decay rate. Although in the case of the present plasma expansion, we have observed an electron density fall that is likely to result from recombination mechanisms.

### 5.5.2 Lateral expansion of the plasma

Figure 5.22(b) shows the lateral spatial distributions of the electron density and temperature. These distributions were obtained from spectra extracted

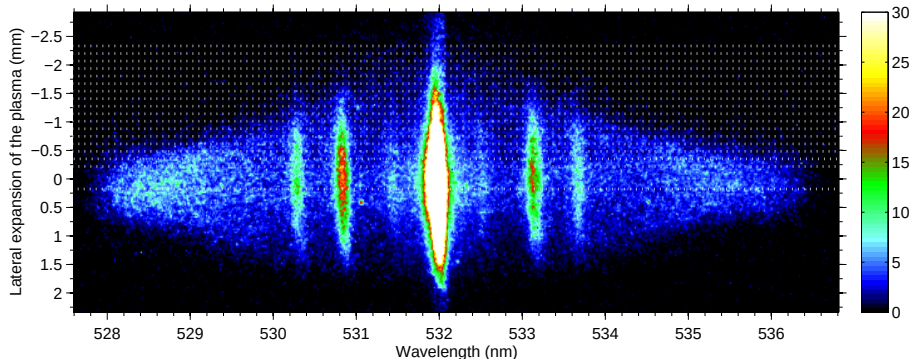


(a) $d = 2mm$ ; $\Delta t = 200ns$ ; Scattering spectrum, full image

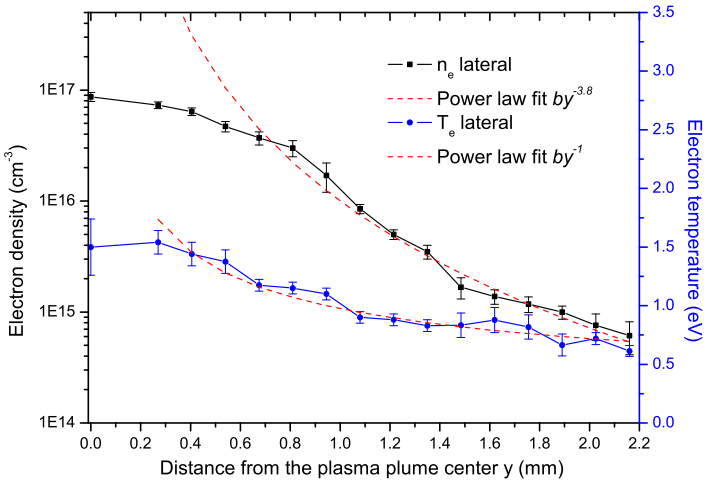


(b) $n_e$ and $T_e$ along the probing laser direction for $d = 2mm$ ; $\Delta t = 200ns$

Figure 5.22: Lateral evolution of the electron density $n_e$ and electron temperature $T_e$ (b) calculated from the scatter spectra (a) taken $2mm$ from the target surface and $200ns$ delay. The dashed lines in image (a) correspond to the steps at which the data was binned for analysis (every $0.13\mu m$). The electron density and temperature profiles are fitted with power laws of the form $by^{-a}$ where y is the distance from the plasma center, in the direction of the probe laser, a and b are constants with $a \approx 3.8$ in the case of the evolution of $n_e$ and $a \approx 1$ in the case of the evolution of $T_e$.

from a single image spectrum, as shown in figure 5.22(a), where the dotted-white lines are representing the area binned to obtained individual scatter spectrum for different plasma volume, along the direction of the probing laser. To generate each line out spectrum, 5 rows of pixels were added, giving steps of $0.135mm$ in the distribution of electron density and electron temperature. The scattering image is the same as the one presented in figure 5.1. The ablating laser fluence was $\sim 10J/cm^2$ and the probing laser fluence $\sim 50J/cm^2$. The expanding Mg plasma was probed $2mm$ from the target surface and with a delay of $200ns$ after the ablation pulse.

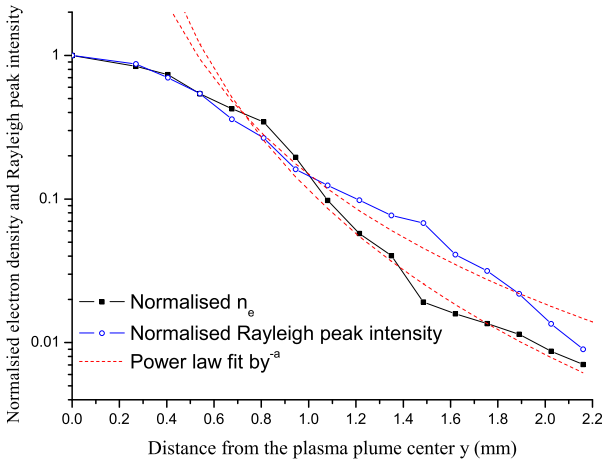


Figure 5.23: Lateral evolution of the density of electron compared to the Rayleigh scattering intensity, proportional to the number of atoms, of the Mg plasma plume, $2mm$ from the target normal, at $200ns$ delay. The plasma expansion is fitted with a power law of the form $by^{-a}$ with $a \approx 3$ for the atom density and $a \approx 3.8$ for the electron density.

The electron density is found to fit a power law of $\sim y^{-3.8}$ in the lateral direction at a fixed time delay of $200ns$. This is close to the decay in atom density given in our data by the intensity of the Rayleigh peak. The power fits in figure 5.23 show approximately a spatial dependence of $n_e \propto y^{-3.8}$ for the electron density and a dependence of $n_a \propto y^{-3}$ for the density of atoms

and ions.

The radial velocity component of the species in the plasma is expected to be significantly smaller compared to the axial velocity component which is enhanced by significant density gradiants at the end of the ablating laser pulse, as discussed in section 2.2. The radial velocity was estimated by comparing the profiles of the Rayleigh peak in the lateral direction as shown in figure 5.24. These profiles were obtained by binning 5 columns in scattering image spectra taken $2mm$ from the target surface, and with different time delays.

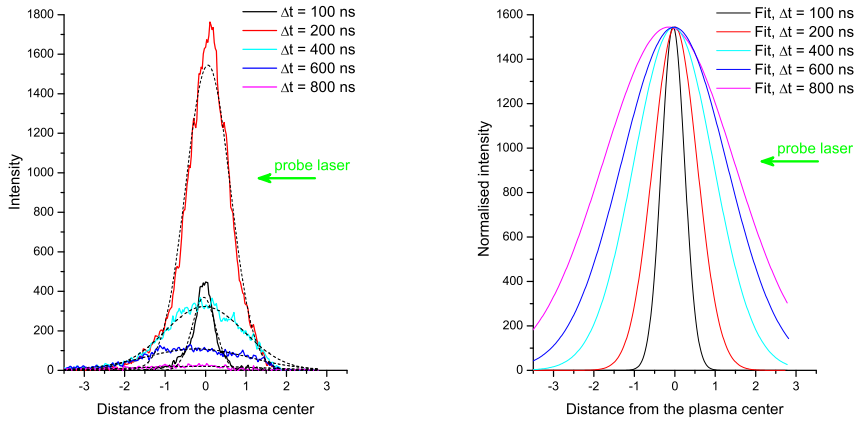


(a) $d = 2mm$ (b) Gaussian fits normalised

Figure 5.24: Lateral profile of the Rayleigh peak evolving with time, $2mm$ from the target surface. The experimental data in figure (a) are corrected for stray light signal and fitted with Gaussian profiles. In figure (b) the fits only are normalised to the data at $\Delta t = 200ns$.

Each peak is then fitted with a Gaussian profile (fig. 5.24(a)) and normalised to the higher intensity peak. Only the fits are shown in figure 5.24(b) for more clarity. As the peak gets broader with time, it is possible to estimate the radial velocity from the difference in the FWHM at different times. An average radial velocity is then estimated to $(4.7 \pm 0.6) \times 10^5 cm/s$. This is 2.8 times smaller than the axial velocity and is broadly consistent with previ-

ous experimental data from interferometry and simulation [83]. Although it depends on the spot size on target and the distance from the target looked at.

## 5.6 Summary

In this chapter we have presented and discussed spatially and temporally resolved scattering images. Results were obtained from plasmas resulting in an irradiance of a Mg target at $\sim 10 J/cm^2$ and probed with a laser fluence of $\sim 50 J/cm^2$. Temporal evolution of electron temperature and density of the plume center were presented and discussed. The electron density evolution, found to fall more rapidly than expected, was compared to the temporal atoms density evolution, decaying as expected.

In the next chapter, results from emission spectroscopy of the Mg plume will be presented and compared to the ones obtained from Thomson scattering measurements.

# Chapter 6

# Emission spectroscopy


For this chapter, the scattering techniques were put aside. The scattering experimental set-up described in chapter 4 was adapted to detect only emission spectra from the Mg plasma under study in this work. Time resolved emission spectroscopy is a widely used diagnostic technique as it presents the non negligible advantages of being non intrusive and easy to implement [14, 19, 90, 91, 92]. The plasma electron temperature and density can then be determined from the ratios of emission lines intensities and Stark

broadening respectively. However, applying this technique usually requires us to assume that the plasma is in local thermodynamic equilibrium and in particular that the lines are optically thin. This chapter will present results obtained from emission spectroscopy for Mg plumes similar to the ones studied so far, and a comparision with the results obtained in the previous chapter from Thomson scattering will be discussed.

## 6.1 Revised experimental set-up

Emission spectra were easily obtained with the scattering experimental apparatus illustrated in figure 4.3. The spectrometer had just to be tuned to a wavelength range containing emission lines of Mg. No changes were made in the timing configuration, so the emission spectra were similarly recorded with an effective gate of $\sim 10ns$ (see section 4.2.6). As previously, the geometry of the experiment enabled us to record a slice of plasma at a time, at a predetermined distance from the target surface. The spatial resolution could obviously not be identical, as no probing laser is present to define the plasma volume probed, as in a Thomson scattering experiment. Although the set-up was left as identical as possible to allow comparison between the two diagnostic techniques, the measurements done in this chapter correspond to averaged values over a significantly larger plasma volume than in the previous chapter. As a result, any result has to be considered carefully as far as comparison between diagnostics is concerned.

The SPEX $1-meter$ spectrometer described in section 4.2.3 was used in single grating configuration to extend the range of emission lines that could be detected at a time. The high resolution of that spectrometer allowed more precise determination of the width of the emission lines in view of calculating the electron density of the plasma. However, even in a single grating configuration, giving a dispersion of $1.15nm/mm$, the spectral window of $\sim 20nm$,

limited by the image intensifier in front of the CCD, did not allow the detection of two emission lines of Mg at the same time. A Multispec $125^{TM}$ $1/8m$ Oriel spectrometer was then used instead. The spectrometer was equipped with a $400l/mm$ grating blazed at $400nm$ (model 77416), and with a $50\mu m$ entrance slit. The same ICCD camera was used (see section 4.2.4), so combined with the spectrometer, a resolution of $0.53nm/pix$ was obtained, and a spectral window of $240nm$ could be recorded at a time. The system was calibrated using a Zn/Cd/Hg lamp.

The system as presented had a cut off below $\sim 370nm$. This was due to the BK7 glass exit window and the collecting lenses (BK7 glass, with anti-reflection coating in the visible) restricting the measurements in the visible range when Mg has a rich UV spectra. However, a change for UV optical components was not possible at that stage of the experiment.

## 6.2 Emission spectra of Magnesium

Emission spectra of a magnesium plume were recorded. The temporal evolution of the plasma was studied from $50ns$ to $1.5\mu s$, about $2mm$ from the target surface. The laser irradiance on target was $\sim 10J/cm^2$, similar to the conditions described in section 4.1.

A first series of high resolution spectra were obtained with the SPEX spectrometer in single grating configuration. The line out of the spectra, corresponding to a vertical binning of 20 rows at the plasma center, is shown in figure 6.1. The spectra show a strong line at 470.3 nm. This is the Mg I $3s3p(^1P) - 3s5d(^1D)$ transition. In figure 6.1(a), the early spectrum, the line is significantly broader, and sitting on continuum radiation still emitting at $100ns$ delay. The spectra also show several weaker lines, probably due to impurities in the target. According to Goodfellow metals supplier, a

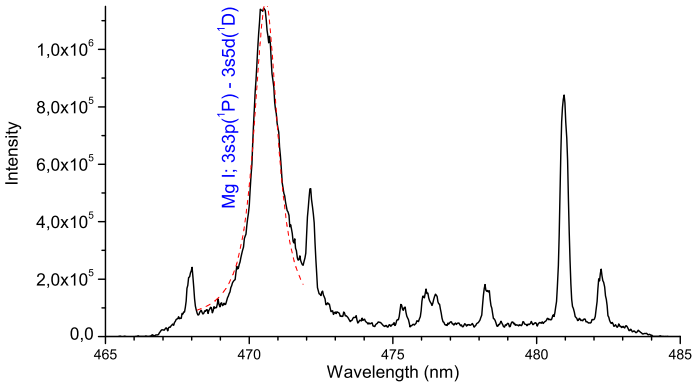


(a) $d = 2mm$ ; $\Delta t = 100ns$

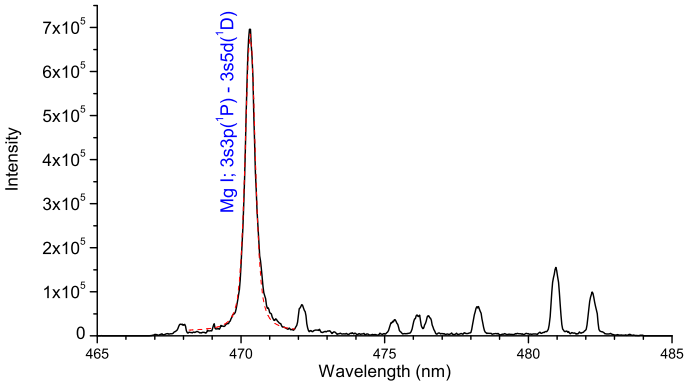


(b) $d = 2mm$ ; $\Delta t = 200ns$

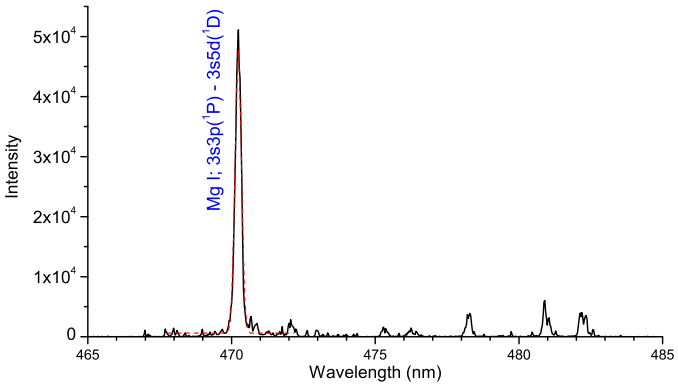


(c) $d = 2mm$ ; $\Delta t = 600ns$

Figure 6.1: High resolution emission spectra from a Mg plume, 100$ns$ delay (a), 200$ns$ delay (b) and 600$ns$ delay (c), 2mm from the target surface. Each spectrum is an accumulation of 25 shots. The peak at 470.3 nm is fitted with a Voigt function.

Mg target of 99% purity contains traces of Fe, Mn, Al, Cu, Si, Ni and Zn. The unidentified lines visible on figure 6.1 could correspond to transitions of Mn and Zn, which have ground state transitions in that spectral region with high emission transition probability ($A_{j\rightarrow i} > 10^7 s^{-1}$) [56].

A second series of spectra was recorded using the lower resolution spectrometer to detect several emission lines simultaneously. The line out of the spectrum taken $2mm$ from the target surface and with $200ns$ delay is shown in figure 6.2. Twenty rows at the center of the plasma were added to produce this line out. The principal Mg lines detected are indicated in figure 6.2 and listed in table 6.1 with the parameters required in section 6.3 and 6.4 to estimate the electron temperature and density. Figure 6.2 shows only ground state transitions. Only early time spectra ($100ns$ delay) show evidence of emission from singly ionised atoms, $MgII$. Some lines in the spectra are not referenced in any Mg atomic database and are likely to be emission from impurities in the target, as mentioned before.

## 6.3 Determination of $T_e$ from emission spectra

The profile of a finite line has a finite width and shape that is determined by the local plasma conditions. These conditions can be determined by accounting for the various mechanisms that can broader spectral lines. The three main mechanisms are: natural, pressure and Doppler broadening. Natural broadening leads to a Lorentzian shape, whereas thermal and Doppler broadening leads to a Gaussian profile for the line. The result of the combination of the Lorentzian and Gaussian broadening is that most spectral lines are best fitted by a Voigt profile. As a result, analyses of the emission spectra was done by fitting Voigt profiles to the lines.

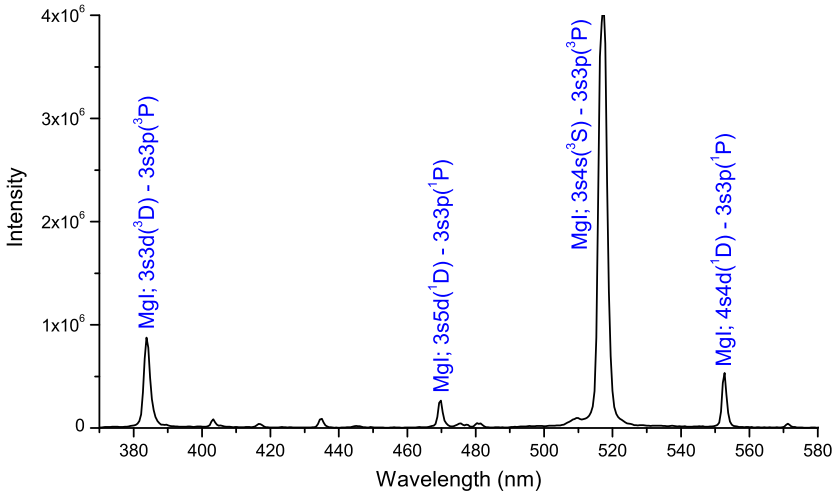


(a) $d = 2mm$ ; $\Delta t = 200ns$

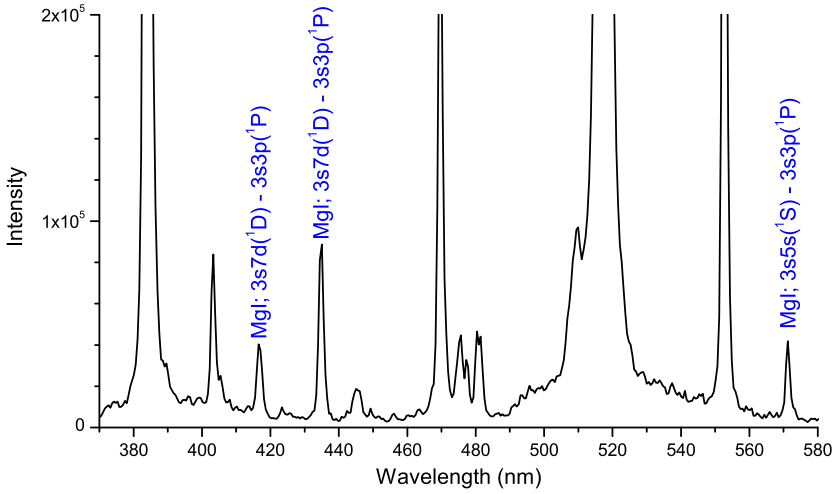


(b) $d = 2mm$ ; $\Delta t = 200ns$; zoom

Figure 6.2: Lower resolution emission spectrum from a Mg plume, 200$ns$ delay, 2mm from the target surface. The spectrum is an accumulation of 100 shots. The Mg transitions are identified.

Table 6.1: Principal lines found in the emission spectra of Mg plumes. $\lambda$ is the wavelength of the emitted radiation, $\omega$ is a Stark broadening parameter corresponding to the electron-impact half width for a temperature of $10,000K$ and an electron density of $10^{16}cm^{-3}$, $U$ and $L$ stand for Upper and Lower levels. Reference of the lines and data are taken from [52, 56].

| Ion | $\lambda$ | Oscillator | Energy | Levels | Statistical | $\omega$ |
|---|---|---|---|---|---|---|
| Mg | (nm) | strength | (eV) | Upper - Lower | weight | (nm) |
| | | $(\times 10^{-1})$ | $E_U$ - $E_L$ | | $g_U$ - $g_L$ | $(\times 10^{-2})$ |
| I | 383.2 | 4.99 | 5.95 - 2.71 | $3s3d(^3D)$ - $3s3p(^3P)$ | 15 - 9 | 1.03 |
| I | 416.7 | 0.60 | 7.32 - 4.35 | $3s7d(^1D)$ - $3s3p(^1P)$ | 5 - 3 | 17.9 |
| I | 435.2 | 0.87 | 7.19 - 4.35 | $3s6d(^1D)$ - $3s3p(^1P)$ | 5 - 3 | 9.51 |
| I | 470.3 | 1.21 | 6.98 - 4.35 | $3s5d(^1D)$ - $3s3p(^1P)$ | 5 - 3 | 4.72 |
| I | 517.8 | 1.35 | 5.11 - 2.71 | $3s4s(^3S)$ - $3s3p(^3P)$ | 3 - 9 | 0.326 |
| I | 552.8 | 1.06 | 6.59 - 4.35 | $3s4d(^1D)$ - $3s3p(^1P)$ | 5 - 3 | 2.61 |
| I | 571.1 | 0.063 | 6.52 - 4.35 | $3s5s(^1S)$ - $3s3p(^1P)$ | 1 - 3 | 2.38 |
| II | 448.1 | 9.81 | 11.63 - 8.86 | $4f(^2F)$ - $3d(^2D)$ | 14 - 10 | 0.783 |

There are several methods to determine the electron temperature of a plasma out of an emission spectra. The most commonly used ones assume a state of local Thermodynamic Equilibrium (LTE) and consider the line-to-line ratios from the same charge state, or the line-to-line ratios from successive charge stages.

### 6.3.1 Line-to-line ratios from the same charge state

This technique is based on the fact that the population distribution of any two states can be related by the Boltzmann factor, assuming a state of Local Thermodynamic Equilibrium [14, 19], as shown in equation 5.3 in section 2.4.1. From this equation follows an expression for the ratio of line intensities ($I_1/I_2$) of two individual spectral lines belonging to the same atomic species:

$$\frac{I_1}{I_2} = \frac{f_1 g_1 \lambda_2^3}{f_2 g_2 \lambda_1^3} exp\left(-\frac{E_1 - E_2}{k_B T}\right) \tag{6.1}$$

where $E_1$ and $E_2$ are the energies of the upper states of the two transitions involved in the measurement, $\lambda$, g, and f are the wavelength, statistical weight and oscillator strength of the line, respectively.

This equation offers the possibility to infer the electron temperature without knowledge of the density. However, we see from the exponential term in equation 6.1 that the accuracy of the temperature determination is the better the larger the energy difference $E_1 - E_2$. In the data collected (see spectra in figure 6.2, and table 6.1) the difference between any two energies of the upper state is small ($\leq 1eV$), so the accuracy of the method is poor. The accuracy of this method may be improved by measuring a number of different lines. The logarithm of the intensity ratios, versus the excitation energies of the upper levels should produce a straight line whose slope renders the temperature [14, 90].

Figure 6.3 shows such Boltzmann plots using the seven $MgI$ lines detected at the same time for a plasma $2mm$ from the target surface and with $200ns$ delay. The intensity of each line is given by the area under a Voigt fit to the experimental data. The intensity is corrected for wavelength dependence attenuation due to the optical components in the detection channel: transmission of BK7 glass (window at the exit of the vacuum chamber and lenses), reflection of Al mirrors, efficiency of the grating, and quantum efficiency of the ICCD, from the different manufacturers specifications.

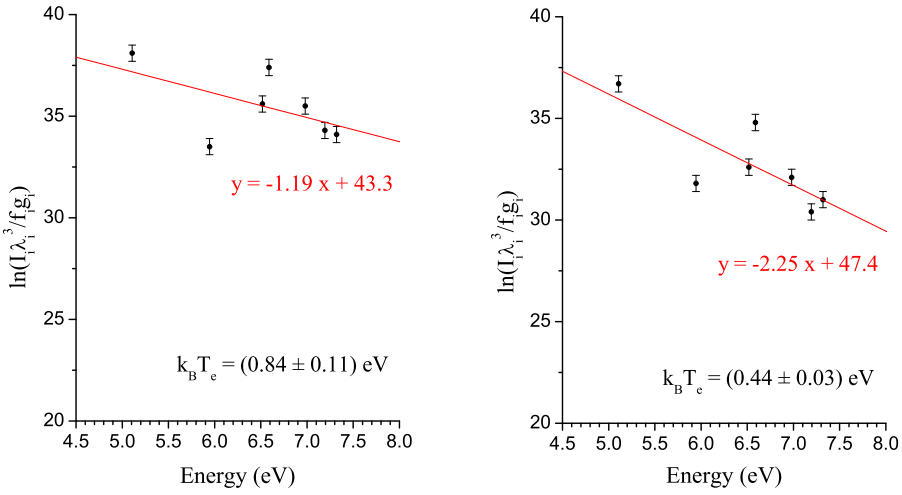


(a) $200ns$ delay (b) $700ns$ delay

Figure 6.3: Bolzman plots of Mg I from emission spectra, $200ns$ delay (a) and $700ns$ delay (b), 2mm from the target surface.

These plots were obtained considering 30% error on the line intensity and 10% error on the oscillator strength [56, 93]. The error on the emission lines was considered significant, not so much from the error on Voigt fit, but as an attempt to take into account a possible reabsorption of the emitted light, or any other phenomena that would modify the intensity of the line.

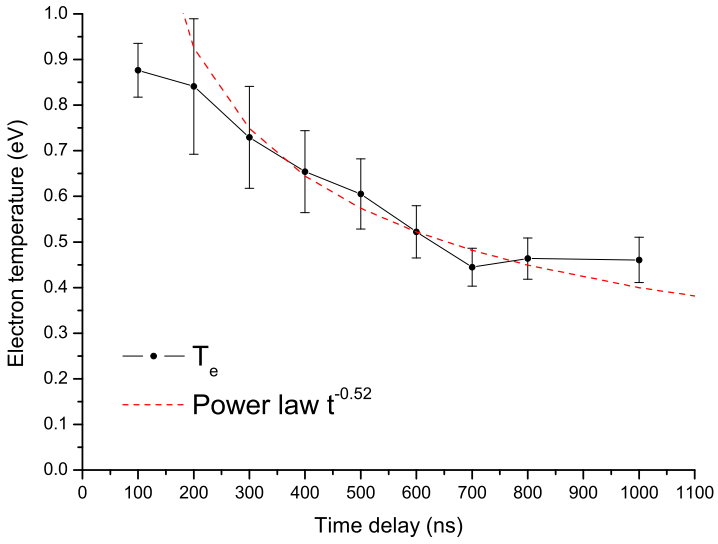


Figure 6.4: Electron temperature evolution with time for plasma $2mm$ from the target surface, infered from emission spectroscopy, using Bolzman plots of Mg I line intensity, such as shown in figure 6.3.

We can see however that there is a significant deviation from a straight line plot. The plasma might not be sufficiently close to LTE to apply this diagnostic method, and the lines might not be optically thin. There might also be errors in the integration of the line profiles caused by underlying continuum emission, although after $200ns$, the continuum is not strong compared to the intensity of the lines (see figure 6.1).

The evolution with time of the electron temperatures calculated using this first line-to-line ratios method is shown in figure 6.4. The temperatures calculated using this method are lower than the temperatures found in the previous chapter using a Thomson scattering diagnostic (see figure 5.18(a)). The experimental condition in the plasma initiation were repeated as accurately as possible, the irradiance on target was $\sim 10J/cm^2$ in both cases.

Moreover the emission and scatter spectra were the results of data integrated over more than 100 shots, so there is no reason for the signals to lead to significant differences. There are two possibilities that would explain this discrepancy. Firstly, the plasma plume might be heated by the probe beam in the Thomson scattering experiment, although this point was discussed in section 5.4.2. Secondly, the results from emission spectroscopy are compromised by an LTE assumption no longer valid. In view of the uncertainty of the results presented above, the second possibility is obviously favored. Furthermore, it can be noted that D. Riley *et al* [52] draw simular conclusions from their simulation work of laser ablated magnesium plasmas, using a collisional radiative equilibrium model. They found that the inferred temperature using line ratios under the assumption of partial LTE was under estimated at low density, below $10^{15} cm^{-3}$, in the $\sim 1eV$ regime.

### 6.3.2 Line-to-line ratios from successive charge stages

The accuracy of the previous method could obviously be improved, and a way to achieve this is by maximising the energy difference between the two excited levels. This requirement of large energy difference leads to the use of lines from different ionisation stages. Instead of relating the integrated intensity ratios using the Boltzmann equation as was done in the previous method, it is now necessary to relate the intensities using the Saha equation (see equation 2.25). The ratio of the integrated line profiles becomes

$$\frac{I_2}{I_1} = \frac{f_2 g_2 \lambda_1^3}{f_1 g_1 \lambda_2^3} \left(4\pi^{3/2} a_0^3 n_e\right)^{-1} \left(\frac{k_B T_e}{E_H}\right)^{3/2} exp\left(-\frac{E_2 + E_\infty - E_1 - \Delta E_\infty}{k_B T_e}\right) \tag{6.2}$$

where $E_\infty$ is the ionisation energy of the lower of the two ion stages, $E_H$ the ionisation energy of hydrogen, $a_0$ the Bohr radius, and the other symbols have been used in equation 6.1. The correction factor $\Delta E_\infty$ lowering the

ionisation energy was neglected as it plays essentially a role in high densities and is several orders of magnitudes lower than the ionisation energy of $MgI$ in the temperature and density conditions of this work (see section 2.4.1).

The only spectra showing evidence of singly ionised ion emission is the early time spectra taken for $100ns$ delay. The $MgII$ $4f(^2F)$ - $3d(^2D)$ transition at $448.1nm$ can then be used along with one of the $MgI$ line to calculate the electron temperature of the plasma, $2mm$ from the target surface, and $100ns$ delay. Figure 6.5 shows the values found for $T_e$ when using the ratio $MgII$ $448.1nm/MgI$ $470.1nm$ to solve equation 6.2 for different values of $n_e$. When using any other $MgI$ line, the value of $T_e$ calculated is within less that 10% error. The two red crosses indicate the values of $T_e$ taken when using the density measured in chapter 5 with the Thomson scatter diagnostic and the density measured in the section 6.4 following with the emission spectroscopy diagnostic.

The value of $T_e$ estimated with this method is more than 3 times lower than the value estimated using Thomson scattering, but it is also 15% lower than the temperature measured with the previous line ratio method. This emphasises again the uncertainty of emission spectroscopy as a diagnostic for low temperature laser plasmas, when LTE is assumed.

## 6.4 Determination of Ne from emission spectra

A widespread method to determine the electron density from emission spectroscopy is following the broadening of a spectral line. There are three main mechanisms contributing to the broadening of a line: natural, Doppler and pressure broadening. Each of these broadening mechanisms reflect a fundamental property of the emitting species, such as transition probability,

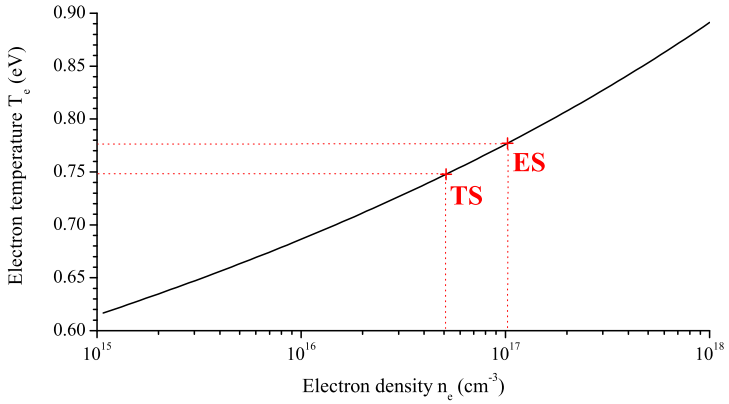


Figure 6.5: Electron temperature obtained by solving equation 6.2 for different densities and for a ratio of line intensities given by the $MgII$ $4f(^2F)$ - $3d(^2D)$ transition at 448.1$nm$ and the $MgI$ $3s5d(^1D)$ - $3s3p(^1P)$ transition at 470.3$nm$. The red crosses indicate the values given for the particular electron densities measured with Thomson scattering (TS) or emission spectroscopy (ES). The data concern a plasma volume 2$mm$ from the target surface, 100$ns$ after the ablating laser pulse (of fluence on target$\sim 10J/cm^2$).

thermal velocity, and collision frequency respectively [94].

### 6.4.1 Line broadening mechanisms

#### Natural broadening

This arises because of the fact that the quantum states of an atom do not have a single energy, but a small spread in energy of the order of $\hbar/\tau$ where $\tau$ is the life time of the state. Therefore there is a finite probability that photons will be emitted with energies in an interval centered about $(E_b - E_a)$ of width $(\hbar/\tau_a + \hbar/\tau_b)$ where a and b refer to two states [94].

Natural broadening is the minimum possible spectral line width that can be observed from a transition. It is not resolvable by most spectrom-

eters, and usually masked by more significant mechanisms. The minimum observable line width in our case is given by the instrument function and was determined from the calibration of the spectrometer (see section 4.2.3).

**Doppler broadening**

The observed wavelength of a line emitted by a moving atom is shifted by the Doppler effect, to shorter wavelengths if the emitter is moving towards the observer, and to longer wavelengths if moving away. The observed wavelength is given in function of the velocity of the emitter $v_x$ and the rest wavelength $\lambda_0$ as [94]

$$\lambda_{observed} = \lambda_0 \left(1 \pm \frac{v_x}{c}\right) \tag{6.3}$$

The addition or subtraction sign indicates whether the emitter is approaching or moving away from the observer. The Doppler effect spreads the wavelength distribution observed and is related to the velocity distribution of the emitting particles. In all of the three models of partial equilibrium considered in section 2.4, a Maxwellian velocity distribution can be assumed. This leads to a Gaussian profile for the spectral line, with a full width half maximum (FWHM) due to Doppler broadening given, in $nm$, by

$$\Delta\lambda_{D_{FWHM}} = 7.16 \times 10^{-6} \lambda_0 \sqrt{\frac{T}{m_a}} \tag{6.4}$$

where $m_a$ is the atomic weight, $\lambda_0$ is the central wavelength in $nm$ and $T$ is the temperature in Kelvin [90]. Doppler effect contributes more to broaden spectral lines at high temperature, and in low-z elements where the velocities of the emitters are usually greater.

In the case of the present experiment, the Doppler broadening takes values from $\sim 0.04nm$ to $\sim 0.13nm$ for the neutral magnesium line, $3s5d(^1D)$ -

$3s3p(^1P)$ at $470.3nm$, in the temperature range measured in chapter 5 using the Thomson scattering diagnostic.

**Stark broadening**

Further broadening can be caused by interactions between the emitting ions and surrounding particles. This pressure broadening may be sub-divided into three categories: (i) resonance, (ii) VanderWaals and (iii) Stark broadening, depending on whether the interaction with the emitter is caused by: (i) the same type of atom, (ii) a different type of atom, or (iii) a charged particle. The majority of particles in a plasma being charged by definition, Stark broadening is of more interest in our case.

Stark broadening is the result of collisions between the emitter and nearby charged particles. There are two components that contribute to the broadening of a spectral line due to Stark effect: the first is caused by electron emitter collisions, the second by ion-emitter collisions. The first type of collisions makes the greatest contribution to the Stark broadening. They occur on a time-scale much shorter than both the natural lifetime of the excited state and the time between ion-emitter collisions. On the other hand, ion-emitter collisions take place over a much longer period, such collisions are known as the quasi-static component of the Stark effect.

Stark broadening leads to a Lorentzian line shape [46] and the FWHM of the Stark broadening of a line, $\Delta\lambda_{S_{FWHM}}$, from neutral atoms can be expressed as [14, 92]

$$\Delta\lambda_{S_{FWHM}} = 2w\left(\frac{n_e}{10^{16}}\right) + 3.5\alpha\left(\frac{n_e}{10^{16}}\right)^{1/4}\left[1 - \frac{3}{4}N_D^{-1/3}\right]w\left(\frac{n_e}{10^{16}}\right) \quad (6.5)$$

where $N_D$ is the number of particles in the Debye sphere given in equa-

tion 1.2 and $n_e$ the electron density in $cm^{-3}$. $w$ and $\alpha$ are electron impact width parameter and ion-broadening parameter respectively, independent of $n_e$, they are slowly varying function of the electron temperature. These Stark width parameters are given by Griem [19] for given ionic species and given temperatures. In equation 6.5 the first term in the right-hand side describes the contribution due to electron-emitter collisions, and the second term is the correction for the ion contribution. For species of low ionisation, Stark broadening of lines is usually dominated by electron collisions, allowing to neglect the ion broadening term [92].

### 6.4.2 Electron densities

When the plasma is dense enough, so that Stark broadening dominates over Doppler broadening, Stark widths can be measured in order to infer the electron density of the plasma under study. Spectroscopic measurements with a resolution high enough is also required so that the broadening of the line due to the instrument function does not dominate other broadening mechanisms.

As mentioned in the previous section, a spectral line broadened by natural or Stark broadening leads to a Lorentzian line shape, whereas Doppler broadening leads to a Gaussian profile for the line. The result of the combination of the Lorentzian and Gaussian broadening profiles is that most spectral lines are best fitted by a Voigt profile. The various broadening mechanisms may then be determined by resolving the Gaussian and Lorentzian components of a measured Voigt profile.

The spectra presented in figure 6.1 were used to analyse the profile of the $MgI$ $3s5d(^1D)$ - $3s3p(^1P)$ transition at $470.3nm$. Voigt functions were fitted to the emission line in order to take into account the various pro-

cesses that contribute to the line broadening. The Stark contribution to the broadening is described by the Lorentzian component and all other contributions such as the Doppler effect and the instrument function of $\sim 0.20nm$ (section 4.2.3) were accounted for in the Gaussian component of the Voigt profile [19]. The Doppler contribution to the broadening was calculated using equation 6.4, and is estimated to $\sim 0.07nm$ for a plasma temperature of $1eV$. The electron density was then calculated using equation 6.5, and $\Delta\lambda_{S_{FWHM}}$ was estimated using only the Lorentzian component of the fitted Voigt profiles.

Using both the electron-impact and the quasi-static ion component of equation 6.5 introduces a temperature dependence incorporated in the Debye length term $N_D$. Using the temperatures calculated in section 5.5 with Thomson scattering or in section 6.3 with emission spectroscopy, the electron density was calculated for the experimentally observed linewidth by minimising equation 6.5 in terms of $n_e$. A difference of up to 15% for the higher temperature cases was observed if it was assumed that contribution in collisions was almost entirely due to electron impact, and only the first term in equation 6.5 was used in the calculation of $n_e$ as suggested by several authors [92, 91]. For this reason, the full equation was used to estimate $n_e$.

Figure 6.6 shows the temporal evolution of electron density after a plasma initiation with a laser of fluence $\sim 10J/cm^2$. The error bars are reflecting the difference found depending on which temperatures were used in the calculations (determined by Thomson scattering or emission spectroscopy), as well as the error in the fitting procedure. The density could not be determined for plasma later than $600ns$ as the Stark broadening was no longer significant enough compared with other broadening mechanisms (mainly instrumental broadening). This figure 6.6 may be compared with figure 5.18(a) showing

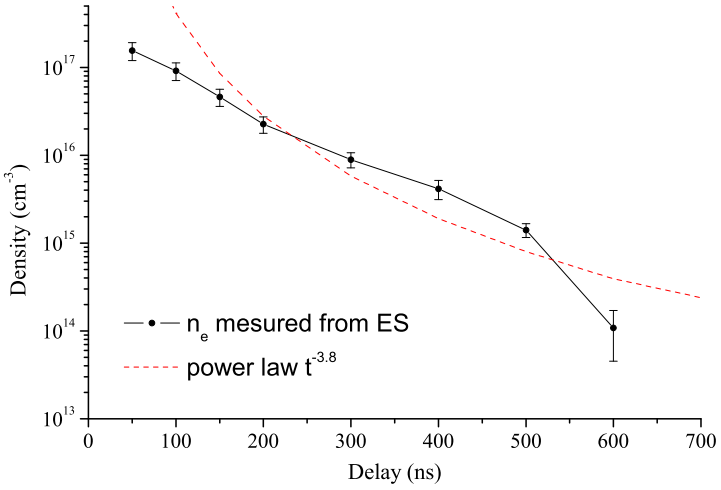


Figure 6.6: Electron density evolution with time for plasma $2mm$ from the target surface, determined by calculating the Stark width of the emission line of $MgI$ at $470.3nm$ in the spectra shown in figure 6.1.

the temporal evolution of the electron density measured for a similar plasma using a Thomson scattering diagnostic. One can see first that the density evolution in figure 6.6 is not peaking at $200ns$ but shows a constant decrease. This is probably due to the fact that the spatial resolution in the case of emission spectroscopy is not as good and emission from a larger region is detected, whereas in the case of the Thomson scattering diagnostic, only the plasma flowing through the probe is detected at any one time. The values of $n_e$ calculated in this section are lower (from 10% to 80%) than the values found using Thomson scattering. Similarly to figure 5.18(a), a power law fit is plotted in figure 5.18(a), showing a $t^{-3.8}$ dependence. This is still a quicker drop than the $t^{-3}$ expected (see section 2.2) but is not as pronounced as in the previous chapter were power laws $\propto t^{-5}$ were found to best fit the electron density evolution with time. We note also that the shape of the power law is not fitting as well.

## 6.5 Summary

In this chapter we have presented and discussed temporally resolved emission spectra of an expanding laser produced Mg plasma. Temporal evolution of electron temperature and density were obtained for a plasma $\sim 2mm$ from the target surface. These results were obtained from a plasma generated in similar conditions than in chapter 5, "Optical scattering from Mg plumes", so that the two diagnostics could be compared. The validity of the local thermodynamic equilibrium in such a plasma was then discussed.

The next and final chapter will conclude this thesis and suggest further work for the future.

# Chapter 7

# Conclusions and future work

*"Même lisse et rond,*
*le galet garde en mémoire*
*les angles du gel"*
*"Le coucou du Haïku", Paul Bergèse*

Pulsed laser deposition is a technique used in thin film preparation in many laboratories because of its flexibility and the possibility to create materials of divers nature. As previously described (section 1.2), the technique consists in focusing a laser into a target, producing a fast expanding plasma plume that condensate on a subtract material. The quality of the film produced is obviously highly dependent on the properties of the expanding plume. This is partly where difficulty arise, as a full characterisation of these plasmas is complicated by its rapidly changing nature. It is in this context that Queen's University has initiated a study combining different diagnostics and ablation techniques [9, 10, 11, 12, 13]. The latest contribution to this study has been presented in this thesis and will be summarised in the present chapter. In view of the results obtained, further work is then

suggested for the next step the project could take in order to contribute in the progress of pulsed laser deposition techniques, as well as in fundamental knowledge of such plasmas.

## 7.1 Thesis in a nutshell

The work presented in this thesis has been concerned with the expansion of laser-produced plasma plumes at modest temperature (around 1 eV). A Thomson scattering diagnostic was implemented to study these plumes, and in particular monitor the evolution of the plasma electron density and temperature. This is a powerful diagnostic widely used for a variety of other plasmas, but a novel technique for this type of plasma. In addition, Rayleigh and Raman scattering proved to be useful diagnostics to provide further information about the relative population of specific excited states within the expanding plasma plume. Spatially and temporally resolved emission spectroscopy has also been used to provide a complementary diagnostic of the plumes.

The Thomson scattering diagnostic was developped to measure the electron temperature and density in a $Mg$ laser-produced plasma at low temperature and modest densities. The temporal evolution of plasma flowing through a fixed point has been presented for several distances from the target surface, as well as the spatial evolution of the lateral expansion of this plasma. In particular, it was found that $2mm$ from the target surface and within $\sim 1\mu s$ of expansion, the electron density drops rapidly, following a power law of $\sim t^{-4.95}$ as opposed to the $t^{-3}$ dependence suggested by a volumetric expansion. In the mean time, the number of atoms decreases as expected with time. The rapid drop in electron density might be explained by dielectronic recombination (DR) being faster than from calculation. This interpretation would be in accordance with crossed beam experiments [53]

suggesting a DR cross-section larger than the calculated value by a factor of 5. The measured electron temperature was found to vary with a $t^{-1}$ time dependence; this result is consistent with an adiabatic expansion of the plasma where energy is injected into electrons by three-body recombination, reducing the rate at which the electrons are cooling.

Simultaneously, signals from atomic type Raman scattering and Rayleigh scattering were detected. The Raman signal was identified as coming from transitions between the different angular momentum levels of the $^3P^0$ metastable term in $MgI$. Comparison with first calculations of cross-sections for both the ground state and metastable state of $MgI$ [69] lead to draw first conclusions on the evolution of the relative population of excited states whithin the plume in expansion. However, these calculations reveled a Rayleigh scattering cross-section from the metastable state 40 times greater than the ground state one, suggesting that in the Rayleigh scattering signal detected, the contribution from the metastable might be dominant, even if their relative population is small. As a result, in order to find the density of neutral atoms from the Rayleigh signal, and subsequently, an absolute measurement of the ionisation fraction in the plume, a good knowledge of the relative population of each excited state is required, as well as accurate calculations of Rayleigh scattering cross-sections for other excited states.

For the last part of this work, the detection system was adapted to undertake a study of the Mg plasma plume by emission spectroscopy, in order that it may be compared with the scattering results. The electron density was obtained by calculating the Stark width of the emission line of the $MgI$ $3s5d(^1D)$ - $3s3p(^1P)$ transition at $470.3nm$. For the plasma $2mm$ from the target surface, the evolution of the density with time could only be obtained up to $600ns$ delay. The Boltzmann plot method was used to mesure the

excitation temperature of $MgI$ species emitting in the visible and to relate them to the electron temperature. Both diagnostics showed some discrepancy that will be discussed in the following section.

## 7.2 Conclusions and suggestions

The advantages and disadvantages of using scattering diagnostics -and in particular Thomson scattering- can be both understood by considering the experiment described in this thesis.

The principal disadvantage is that it is a relatively complicated optical diagnostic technique. The experimental arrangement applied to low temperature laser-plasmas is more complex than other techniques and requires in particular precise alignment and synchronisation. This had to be combined with a multitude of apparatus to reduce and resolve perturbing signals in order to detect the weak Thomson scattering signal. Also, a well thought balance had to be found in the choice of the probing laser to have enough energy to scatter a detectable signal, but not too much to heat the plasma. The technical chalange counted especially, as the small size of the plasma studied and its rapidely changing nature only enhanced the experimental difficulties cited above. This work has shown that with the techniques available today, it is possible to overcome the experimental disadvantage to make Thomson scattering a well suited technique for the analyses of low temperature laser plasmas, allowing the characterisation of its electron density and temperature.

The key advantage of Thomson scattering, that makes it a valuable technique, is that the scattering data can be unambiguously interpreted and the measured density and temperature are therefore absolute measurements.

Thomson scattering could then be used to check the accuracy of other measurement methods, the way it was done for emission spectroscopy in this work, or probes for gas discharges [95]. In fact, the temporal evolution of the electron temperature and density showed a discrepancy between the two diagnostics results, and in particular for the electron temperature, as shown in figure 7.1.

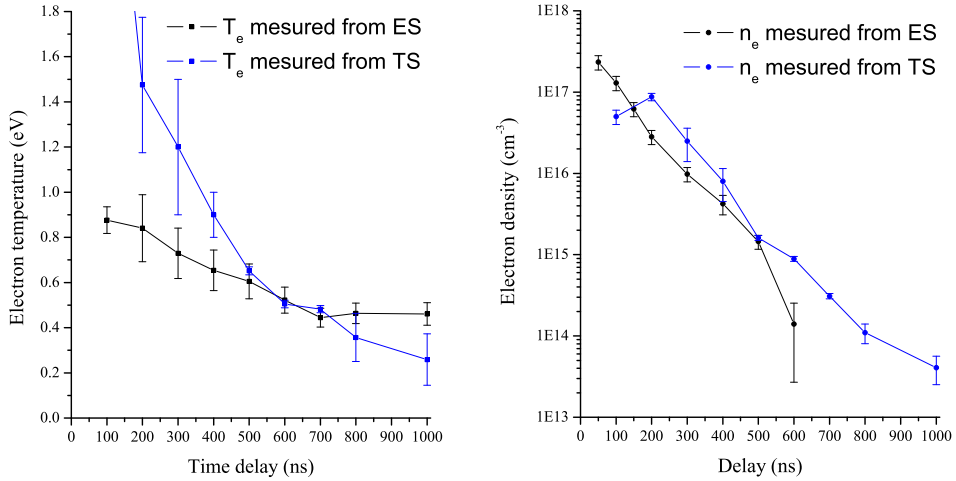


(a) Electron temperature (b) Electron density

Figure 7.1: Axial evolution of the electron temperature and density with time delay, for a Mg laser plasma probed $2mm$ from the target surface, and obtained using a Thomson scattering diagnostic (TS) for the data in blue or emission spectroscopy (ES) for the data in black (as detailed in chapter 5 and 6 respectively). The ablating laser had a pulse energy of $\sim 10J/cm^2$.

This is explained by the assumption of local thermodynamic equilibrium required to interpret the emission spectra. However, the accuracy of this technique to determine the electron temperature could be improved, independently of the assumptions made, by increasing the energy difference between the two excited levels of the emission lines considered in the analyses as decribed in section 6.3.2 and detailed in reference [19]. In the case of Mg, strong emission lines are expected in the UV part of the spectra, and in

particular, the $MgII\ 3p(^2P)$ - $3s(^2S)$ transition at $279.5nm$ is a transition to the ground state with an A-rate of $2.6\times10^8 s^{-1}$. This would obviously require significant changes in the experimental apparatus to use optical components transmitting UV signals, in the detection chanel, when in the present experiment the exit window and the focusing lenses are made of $BK7$ glass, and the turning mirrors are Al coated, giving a lower detection limit of $\sim 380nm$.

The results obtained from Thomson scattering could also be used as a data set for either testing the validity of models and simulations of the plasma expansion dynamics, or as a starting point for further analysis. In particular, further work should now be possible to refine the collisional-radiative model developped by Dr Riley for predicting the optical emission spectrum of low temperature Mg plasmas [52]. The model could then be used to fit the experimental emission spectra obtained during this work.

The laser scattering diagnostic implemented during this research work can be regarded as preliminary work which concerns the simple expansion of plumes resulting from the ablation of single element target only. As the diagnostic is now operational, it may be applied to other laser plasmas in a similar regime. New experiments which combine more elaborate systems can now be considered, to probe plasmas such as: plasma from irradiation of composite target materials of several elements, plasmas expanding in an ambiant gas, modified plasmas by collision of two plumes, or passage through a charged mesh... Some of them have already been developped at Queen's University with other diagnostics such as laser induced fluorescence and laser absorbtion spectroscopy [12, 13].

Before that, it seems that further work would be interesting to explore the atomic Raman scattering features observed. Experimentally, the ratio

of the Raman features could be monitored when varying parameters in the probe, such as the direction of polarisation. Other spectral regions or different target elements could also be investigated. Some target choices amongst others would be calcium which first excited state $3p^6 4s4p(^3P)$ splits in three different angular momentum levels of energy difference $\sim 52.2cm^{-1}$ for $J = 1$ and $\sim 105.9cm^{-1}$ for $J = 2$ from the $J = 0$ level. Similarly for the ground state of $SiI$ the J levels are separated by $\sim 77.1cm^{-1}$ and $\sim 223.2cm^{-1}$ [56]. Moreover, further analytical work is ongoing to calculate the cross-sections of additional levels of $MgI$, and improve the accuracy of the calculated cross-sections. The cross-sections of ground states and excited levels will be calculated for aluminum as well in order to interpret the experimental data (figure 5.12).

## 7.3 Publication

The work presented in this thesis has been published in Applied Physics Letters [28]:

"Optical Thomson scatter from laser ablated plumes"

*A. Delserieys, F. Y. Khattak, J. Pedregosa Gutierrez, C. L. S. Lewis and D. Riley*, Applied Physics Letters, **92** (2008), 011502

# Bibliography


[1] Chen, F. F. *Introduction to plasma physics and controlled fusion.* Plenum Press, New York, (1974).

[2] Sheffield, J. *Plasma Scattering of Electromagnetic Radiation.* Academic Press, London, (1975).

[3] Friichtenicht, J. F. *Review of Scientific Instruments* **45**(1), 51 (1974).

[4] Steen, W. M. *Laser material processing.* Springer, (2003).

[5] Gitomer, S. J. and Jones, R. D. *IEEE Transactions on Plasma Science* **19**, 1209 (1991).

[6] Chrisey, D. B. and Hubler, G. K. *Pulsed Laser Deposition of Thin Films.* Wiley, (2003).

[7] Dyer, P. E., Issa, A., and Key, P. *Applied Physics Letters* **53**, 534 (1988).

[8] Sakeek, H. F., Higgins, M., Graham, W. G., Morrow, T., Turner, R. J., and Walmsley, D. G. *Journal of Applied Physics* **70**, 2455 (1991).

[9] Martin, G. W. PhD thesis, The Queen's University of Belfast, (1999).

[10] Doyle, L. A. PhD thesis, The Queen's University of Belfast, (1999).

[11] Martin, G., Weaver, I., Williamson, T. P., El-Astal, A. H., Riley, D., Lamb, M. J., Morrow, T., and Lewis, C. L. S. *Applied Physics Lettters* **74**, 3465 (1999).

[12] Williamson, T. P. PhD thesis, The Queen's University of Belfast, (2001).

[13] McKenna, C. PhD thesis, The Queen's University of Belfast, (Submitted 2007).

[14] Amoruso, S., Bruzzese, R., Spinelli, N., and Velotta, R. *Journal of Physics B: Atomic, Molecular and Optical Physics* **32**(14), R131 (1999).

[15] Weaver, I. and Lewis, C. L. S. *Journal of Applied Physics* **79**, 7216 (1996).

[16] Shott, L. *Plasma Diagnostics, Chapter 11: Electrical probes.* North-Holland Publishing Company, Amsterdam, (1968).

[17] Hendron, J. M., Al-Wazzan, R. A., Mahony, C., Morrow, T., and Graham, W. G. *Applied Surface Science* **96-98**, 112 (1996).

[18] Weaver, I., Martin, G. W., Graham, W. G., Morrow, T., and Lewis, C. L. S. *Review of Scientific Instruments* **70**, 1801 (1999).

[19] Griem, H. R. *Plasma Spectroscopy.* McGraw-Hill Book Company, (1964).

[20] Walkup, R. E., Jasinski, J. M., and Dreyfus, R. W. *Applied Physics Letters* **48**(24), 1690 (1986).

[21] Offenberger, A. A. and Kerr, R. D. *Journal of Applied Physics* **43**, 354 (1972).

[22] Doyle, L., Martin, G., Al-Khateeb, A., Weaver, I., Riley, D., Lamb, M. J., Morrow, T., and Lewis, C. L. S. *Applied Surface Science* **127-129**, 716 (1998).

[23] Bowden, M. D., Goto, Y., Yanaga, H., Howarth, P., Uchino, K., and Muraoka, K. *Plasma Sources Science and Technology* **8**, 203 (1999).

[24] Thompson, C. E. PhD thesis, The Queen's University of Belfast, (2000).

[25] Craig, G. PhD thesis, The Queen's University of Belfast, (2003).

[26] Moshkaylov, S. A. *Journal Vacuum Science and Technolology* **18**(4), 1395 (2000).

[27] Weaver, I., Doyle, L. A., Martin, G. W., Riley, D., Lamb, M. J., Graham, W. G., Morrow, T., and Lewis, C. L. S. *SPIE* **3404**, 341 (1998).

[28] Delserieys, A., Khattak, F. Y., Gutierrez, J. P., Lewis, C. L. S., and Riley, D. *accepted for publication: Applied Physics letters* (2008).

[29] Bogaerts, A., Chen, Z., Gijbels, R., and Vertes, A. *Spectrochimica Acta Part B: Atomic Spectroscopy* **58**, 1867 (2003).

[30] Allmen, M. V. and Blatter, A. *Laser-beam interaction with materials.* Spinger, (1995).

[31] Hughes, T. P. *Plasma and laser light.* Adam Hilger, (1975).

[32] Friedrich, H. E. and Mordike, B. L. *Magnesium Technology - Metallurgy, Design Data, Applications.* Springer - Verlag., (2006).

[33] Lunney, J. G. and Jordan, R. *Applied Surface Science* **127-129**, 941 (1998).

[34] Spindler, H. L., Gilgenbach, R. M., and Lash, J. S. *Applied Physics Letters* **68**, 3245 (1996).

[35] Ready, J. F. *Journal of Applied Physics* **36**, 462 (1965).

[36] Singh, R. K. and Narayan, J. *Physical Review B* **41**, 8843 (1990).

[37] Rosen, D. I., Mitteldorf, J., Kothandaraman, G., Pirri, A. N., and Pugh, E. R. *Journal of Applied Physics* **53**(4), 3190 (1982).

[38] Caruso, A. and Gratton, R. *Plasma Physics* **10**, 867 (1968).

[39] Rumsby, P. T. and Paul, J. W. M. *Plasma Physics* **16**, 247 (1974).

[40] Zel'dovich, Y. B. and Raizer, Y. P. *Physics of shock waves and high-temperature hydrodynamic phenomena*. Dover Publication, New York, (2002).

[41] Stapleton, M. W., McKiernan, A. P., and Mosnier, J.-P. *Journal of Applied Physics* **97**, 064904 (2005).

[42] Anisimov, S. I., Bauerle, D., and Luk'yanchuk, B. S. *Physical Review B* **48**, 12076 (1993).

[43] Itina, T. E., Hermann, J., Delaporte, P., and Sentis, M. *Physical Review E* **66**, 066406 (2002).

[44] Kelly, R. *Nuclear Instruments Methods Physics Research B* **46**, 441 (1990).

[45] Mattioli, M. *Plasma Physics* **13**, 19 (1971).

[46] Salzmann, D. *Atomic Physics in Hot Plasmas*. Oxford University Press, (1998).

[47] Ribicki, G. B. and Lightman, A. P. *Radiative Processes in Astrophysics*. Wiley-Interscience, (1979).

[48] Dreyfus, R. W. *Journal of Applied Physics* **69**(3), 1721 (1991).

[49] Kolb, A. C. and McWhirter, R. W. P. *The Physics of fluids* **7**, 519 (1964).

[50] Thum-Jaeger, A., Sinha, B. K., and Rohr, K. P. *Physical Review E* **61**(3), 3063 (2000).

[51] Shull, J. M. and Steenberg, M. V. *Astrophysics Journal Supplement Serie* **48**, 95 (1982).

[52] Riley, D., Weaver, I., Morrow, T., Lamb, M. J., Martin, G. W., Doyle, L. A., Al-Khateeb, A., and Lewis, C. L. S. *Plasma Sources Science and Technology* **9**, 270 (2000).

[53] Belic, D. S., Dunn, G. H., Morgan, T. J., Mueller, D. W., and Timmer, C. *Physical Review Letters* **50**, 339 (1983).

[54] Richter, J. *Plasma Diagnostics, Chapter 1: Radiation of hot gases.* North-Holland Publishing Company, Amsterdam, (1968).

[55] Zaghloul, M. R., Bourham, M. A., and Doster, J. M. *Journal of Physics D: Applied Physics* **33**, 977 (2000).

[56] (version 3.1.2). NIST Atomic Spectra Database [Online; accessed June-2007].

[57] Kunze, H. J. *Plasma Diagnostics, Chapter 9: The Laser as a tool for plasma diagnostics.* North-Holland Publishing Company, Amsterdam, (1968).

[58] Hollas, J. M. *Modern Spectroscopy.* Wiley, (1992).

[59] Tyndall, J. *Phil.Trans. Roy. Soc. London* **160**, 333 (1870).

[60] Fiocco, G. and Thompson, E. *Physical Review Letters* **10**, 89 (1963).

[61] Funfer, E., Kronast, B., and Kunze, H. J. *Physical Letters* **5**, 125 (1963).

[62] Behn, R. *Applied Physics Letter* **36**, 363 (1980).

[63] Rohr, H., Steuer, K. H., Schramm, G., Hirsch, K., and Salzmann, H. *Nuclear Fusion* **22**, 1099 (1982).

[64] Glenzer, S. H. *Physics of plasmas* **6**, 2117 (1999).

[65] Gregori, G., Kortshagen, U., Heberlein, J., and Pfender, E. *Physical Review E* **65**(4), 046411 (2002).

[66] Y. Izawa, T. Yamanaka, N. T. M. O. and Yamanaka, C. *Japanese Journal of Applied Physics* **7**, 954 (1968).

[67] George, T. V., Englehar, A. G., and DeMichelis, C. *Applied Physics Letter* **16**(6), 248 (1970).

[68] Sneep, M. and Ubachs, W. *Journal of Quantitative Spectroscopy and Radiative Transfer* **92**, 293 (2005).

[69] Sahoo, S., Riley, D., et al. publication in preparation.

[70] Salpeter, E. E. *Physical Review* **120**, 1528 (1960).

[71] Fried, B. D. and Conte, S. D. *The plasma Dispersion Function*. Academic Press, New York, (1961).

[72] Thorne, A. *Spectrophysics*. Chapman and Hall, London, second edition, (1988).

[73] Lewis, C. L. S., Weaver, I., Doyle, L. A., Martin, G. W., Morrow, T., Pepler, D. A., Danson, C. N., and Ross, I. N. *Review of Scientific Instruments* **70**(4), 2116–2121 (1999).

[74] Muraoka, K., Uchino, K., and Bowden, M. D. *Plasma Physics and Controlled Fusion* **40**, 1221 (1998).

[75] Warner, K. and Hieftje, G. M. *Spectrochimica Acta Part B* **57**, 201 (2002).

[76] Andor Technology, Belfast, UK. *ICCD detector InstaSpec V Instruction Manual*.

[77] Lambda Physik GmbG, Gttingen, Germany. *Excimer laser Instruction Manual*.

[78] Quanta Ray, Gttingen, Germany. *Quanta Ray Instruction Manual*.

[79] Doyle, L., Martin, G. W., Williamson, T., Al-Khateeb, A., Weaver, I., Riley, D., Lamb, M. J., Morrow, T., and Lewis, C. L. S. *IEEE Trans. Plasma Sci: Special Edition on Plasma images* **27**, 128 (1999).

[80] Martin, G. W., Williamson, T., Al-Khateeb, A., Doyle, L., Weaver, I., Riley, D., Lamb, M. J., Morrow, T., and Lewis, C. L. S. *IEEE Trans. Plasma Sci: Special Edition on Plasma images* **27**, 130 (1999).

[81] Martin, G., Doyle, L., Khateeb, A. A., Weaver, I., Riley, D., Lamb, M. J., Morrow, T., and Lewis, C. L. S. *Applied Surface Science* **127-129**, 710 (1998).

[82] Pert, G. J. *Journal Plasma Physics* **41**, 263 (1989).

[83] Qaisar, M. S. and Pert, G. J. *Journal of Applied Physics* **94**, 1468 (2003).

[84] Bowden, M. D., Goto, Y., Hori, T., Uchino, K., Muraoka, K., and Noguchi, M. *Japanese Journal of Applied Physics* **38**, 3723 (1999).

[85] (version 0.8.1). http://www.unipress.waw.pl/fityk/.

[86] Pfeiffer Vacuum, www.pfeiffer-vacuum.de. *Compact FullRange Gauge PKR 261, Short operating instructions.*

[87] Prosnitz, D. and George, E. V. *Physical Review Letters* **32**, 1282 (1974).

[88] Kunze, H. J. and Griem, H. R. *Physical Review Letters* **21**, 1048 (1968).

[89] Baranger, M. and Mozer, B. *Physical Review* **123**, 25 (1961).

[90] Lochte-Holtgreven, W. *Plasma Diagnostics, Chapter 3: Evaluation of plasma parameters.* North-Holland Publishing Company, Amsterdam, (1968).

[91] El-Astal, A. H. and Morrow, T. *Journal of applied physics* **80**, 1156 (1996).

[92] Hafez, M. A., Khedr, M. A., Elaksher, F. F., and Gamal, Y. E. *Plasma sources science and technology* **12**, 185 (2003).

[93] M. Aldenius, J. D. Tanner, S. J. H. L. and Ryan, S. G. *Astronomy and Astrophysics* **461**, 767 (2007).

[94] Hutchinson, I. H. *Principles of plasma diagnostics.* Cambridge University Press, (1987).

[95] Bowden, M. D., Kogano, M., Suetome, Y., Hori, T., Uchino, K., and Muraoka, K. *Journal of Vacuum Science and Technology A: Vacuum, Surfaces, and Films* **17**(2), 493 (1999).